THÈSE

En vue de l'obtention du

DOCTORAT DE L'UNIVERSITÉ DE TOULOUSE

Délivré par **l'Institut Supérieur de l'Aéronautique et de l'Espace**
Spécialité : Mathématiques appliquées et systèmes industriels

---

Présentée et soutenue par **Logan JONES**
le 26 juin 2012

Modélisation des forces de contact entre le pneu d'un avion et la piste

---

JURY

M. Pierre Villon, président, rapporteur
M. Christian Bes, directeur de thèse
M. Jean-Luc Boiffier, co-directeur de thèse
M. Jean-Michel Builles
M. Frédéric Lebon, rapporteur
M. Patrick Heuillet

École doctorale   : **Aéronautique - Astronautique**

Unité de recherche   : **Équipe d'accueil ISAE-ONERA CSDV**

Directeur de thèse   : **M. Christian Bes**
Co-directeur de thèse : **M. Jean-Luc Boiffier**

Acknowledgements

It's with a sense of wonderment that I look back at these three (and a half) years and realize how fast it went by. I've always had a fascination for airplanes and aeronautics and this PhD gave me the chance to, not only enter the world of aeronautics with Airbus, but to work on a subject where I truly felt I was making a difference. Contributing to help resolve the unknowns of braking on contaminated runways, improve the modeling of the tire-runway contact friction and thus further improve our calculations of take-off and landing distances.

There are of course many people to thank and I hope I don't forget anyone. My first thanks must go to my PhD directors: Jean-Luc Boiffier, Jean-Michel Builles and Christian Bes, who were always present, helping to ensure this PhD evolved in the right direction. The subject of this PhD was quite open when it first started, and you all helped to define the way forward and kept pushing me to find solutions. Without you, this PhD would surely not have been achieved. A large thanks to all of my colleagues within the Aircraft Performance Department. You warmly accepted me into the group, you put up with my "Franglais" as I ever so slowly learned the French language, you let me on the football pitch where I was able to show that yes, Canadians do know how to play football (and we won the Airbus tournament) and most importantly you taught me Aircraft Performance: take-off distances, landing distances, accelerate-stop, approach climb, landing climb, anti-skid efficiency, torque limitations, V1, V2, VR and much more. A special thanks to my box-mates, Remi, Stephane and Jean-Michel for the excellent conversations, the answers to many many questions and the great ambiance that our box had. I would also like to thank our heads of department, Laurence and Etienne who accepted my application and supported my work all the way through (although on my first day at work, upon hearing what we wanted to accomplish with the PhD, Etienne said to me "Ambitious....Good Luck")

But my work expanded beyond just the Aircraft Performance department. Robert and the Flight Test department provided me with valuable flight test data and even performed some specific flight tests for me. Lars within the Support team provided me with valuable insight into how Airline Operations work.

My colleagues in the Flight Dynamics and Simulation department at Airbus were critical to the success of this PhD. Olivier and Florian opened the doors so that our two departments could work together. With them

working on lateral friction for aircraft control and myself working on longitudinal friction for stopping distances, together we were able to significantly advance the state of the art at Airbus. The collaboration put in place with Research Institutes and Universities was truly the key: the local friction testing performed by Matthias and the crew at University of Hannover, the material testing done by Patrick at LRCCP and the FEM analysis performed by Frederic and Iulian at LMA. Your work was instrumental and the data you provided gave the inputs for the Brush Model and tire-runway characteristics.

Jerome Journade... who saw something in me. You somehow found my CV (still won't tell me where) and you seemed to believe I was the right person for the job. When you first presented me the PhD, I said no. I didn't want to work on friction... I studied aircraft because they FLY! Yet you kept at it. Every time we'd pass in the hallway you'd say "are you sure?". And eventually I realized you were right. This was for me, this was the direction I wanted my career to go in, and since that day I have never looked back. Thank You!

My love and appreciation goes to my girlfriend Lindsey, who also took a chance with me and a life in France. You've been supportive and you took the time (no matter how boring reading a PhD can be) to read and correct my spelling and grammar mistakes and to make sure the PhD was readable!

Lastly, my family. It's never easy to jet off to a new continent, 8 time zones, 7500km and at least two airport connections away from home. But they were always supportive and encouraged me to follow my dreams. I'm lucky to have such a wonderful family and a set of friends with whom time stands still, no matter how long I've been gone.

Thank you all!

For my family

Contents

Part I

Introduction

Chapter 1

Aircraft Performance on Contaminated Runways

Summary. Le sujet de cette thèse de doctorat a été proposé par Airbus
Operations SAS dans le but de combler une lacune dans les connaissances
opérationnelles actuelles : les performances des avions sur pistes conta-
minées. Au sein d'Airbus engineering, le groupe est divisé en plusieurs
départements et sous-départements. Le département chargé des performances
des avions a pour rôle de fournir les données des performances à haute et
basse vitesse pour les avions de la flotte Airbus. Les performances à basse
vitesse concernent particulièrement les phases de décollage et d'atterris-
sage. Ce département fournit les manuels de vol qui sont utilisés par les
pilotes pour calculer les distances de décollage et d'atterrissage en fonction
des configurations des appareils et des conditions environnementales, telles
que l'altitude-densité, la pente de la piste, les vents etc. Ces informations
sont fournies conformément aux règles de certification publiées par les auto-
rités aériennes compétentes. L'autorité compétente pour la certification des
avions est l'autorité du pays où l'avion a été fabriqué. En Europe, il s'agit
de l'Agence européenne de la sécurité aérienne (AESA), aux États-Unis,
c'est la Federal Aviation Authority (FAA). Afin de fournir des distances de
décollage et d'atterrissage dans toutes les conditions, Airbus s'appuie sur la
modélisation des performances des avions, validée par des essais en vol et
certifiée par les autorités aériennes. Cependant, la modélisation des perfor-
mances au décollage et à l'atterrissage sur pistes contaminées est une tâche
plus compliquée. Les règles de certification varient légèrement d'une auto-
rité aérienne à l'autre, mais les essais en vol sur pistes contaminées ne sont
actuellement demandés ni par l'AESA ni par la FAA. Les modèles utilisés
pour les pistes contaminées sont construits sur des recherches menées lors des
50 dernières années. Ces modèles sont basés de manière empirique sur plu-
sieurs essais en vol sous différentes conditions de pistes. Cependant, comme
ces modèles sont empiriques, il est difficile d'en déterminer des ajustements,

car les conditions sont différentes de celles pour lesquelles le modèle a été dérivé. Ce sujet de thèse a alors été proposé afin d'améliorer la modélisation et la compréhension des pistes contaminées. Comme nous le verrons, les réalités de la modélisation du freinage des avions ont fait évoluer l'objet de ce projet de thèse de doctorat. Le besoin d'un meilleur modèle La recherche sur le frottement des pneus, notamment dans le domaine automobile où d'avantages de recherches ont été menées sur ce sujet, révèle les nombreux facteurs qui sont connus pour modifier ce frottement et qui ne sont pas pris en charge par l'industrie aéronautique. Vu la nature du caoutchouc utilisé pour les pneus, des paramètres tels que la température, le type de caoutchouc et la pression de contact modifient les propriétés frictionnelles. De plus, la texture des pistes jour un rôle non négligeable en créant des forces de frottement. Ces effets ne sont pas encore entièrement compris et ils ne sont donc pas pris en compte dans les modélisations des avions.

Des avions atterrissent dans le mode entier, en toute saison. Quel est l'effet produit par un atterrissage à Dubaï en l'été comparé à un atterrissage au plein cœur de l'hiver au nord du Canada ? Comment une variation de 80°C de la température ambiante modifie-t-elle le frottement ? Si certains pneus sont partiellement dégonflés lors de l'atterrissage, cela dégradera-t-il le frottement ? En ce qui concerne les caractéristiques des pistes : comment le frottement diffère-t-il entre une piste dont le revêtement a été récemment renouvelé et une ancienne piste usée ? Toutes ces caractéristiques ont une influence sur le frottement, mais la manière dont elles modifient les performances d'atterrissage des avions est inconnue. Actuellement, dans l'industrie aéronautique, il existe peu de données en matière de modélisation du frottement et les seules caractéristiques qui existent pour les avions concernent les conditions de fonctionnement. Nous nous sommes inspirés de l'industrie automobile et des types de modèles utilisés. La modélisation de la courbe $\mu-slip$ est largement utilisée chez les acteurs de la filière automobile que sont les fabricants de freins, de pneus et de voitures. Les modèles se différentient par leur complexité et la somme de connaissances requises pour les mettre en œuvre. Comme mentionné, l'objectif final de ce travail est d'obtenir un meilleur modèle pouvant prédire les distances d'atterrissage sur des pistes contaminées. Pour y arriver, nous devons améliorer le modèle du coefficient de frottement qui est la force principale impliquée dans l'arrêt de l'avion. Le modèle devra s'appuyer sur le phénomène physique qui se produit à la zone de contact entre le pneu et la piste. Le modèle de la brosse est une méthodologie couramment acceptée dans l'industrie automobile. Cependant, avant d'utiliser ce modèle pour les pistes contaminées, il doit être adapté aux caractéristiques aéronautiques. Nous allons valider et dériver le modèle de la brosse pour le frottement de freinage sur pistes sèches. La disponibilité des données des essais sur pistes sèches et une physique du contact plus simple sont mieux adaptés à la validation du modèle.

L'utilisation du modèle de la brosse comme modèle de frottement pour les

atterrissages sur pistes sèches a nécessité une somme de travail considérable. Nous avons dérivé le modèle de base et sommes allés plus loin qu'une simple dérivation pour mieux comprendre les interactions physiques complexes dans la zone de contact. Nous avons utilisé la tribologie, la science des matériaux et la résistance des matériaux pour construire un modèle de la brosse capable de prendre en compte les facteurs dynamiques.

Au vu de la somme de travail nécessaire pour développer un modèle de la brosse applicable aux avions, le cas des pistes contaminées n'a pas été entièrement exploré. Cependant, comme ce modèle s'appuie sur la physique du contact pneu-piste, l'essentiel du travail peut être élargi aux pistes contaminées, avec une bonne compréhension de la physique du contact sur pistes contaminées.

1.1 Introduction

This PhD work was proposed by Airbus Operations S.A.S. in order to fill a gap in operational knowledge: aircraft performance on contaminated runways. Within Airbus engineering the group is divided into several departments and sub-departments. The aircraft performance department is responsible for providing the high and low speed performance data for the Airbus fleet of aircraft. Low speed performance principally refers to the aircraft during take-off and landing. The department provides the aircraft flight manuals which allow a pilot to calculate the take-off and landing distances for the aircraft as a function of different aircraft configurations and different environmental conditions such as airport density altitude, runway slope, winds etc... This information is supplied in accordance with the certification rules as written by the applicable aviation authority. The applicable aviation authority for aircraft certification is the authority for the country where the aircraft is manufactured. In Europe, the applicable aviation authority is the European Aviation Safety Agency (EASA) while for the United States it is the Federal Aviation Authority (FAA). In order to provide the take-off and landing distances for all conditions, Airbus relies on aircraft performance modeling that has been validated by flight tests and certified by the aviation authorities. However, aircraft take-off and landing performance on contaminated runways is a more complicated modeling problem. The certification rules vary slightly between different aviation authorities but for the current EASA and FAA regulations, flight tests on contaminated runways are not required. The models used for contaminated runways are based on a combination of research that has been performed during the last 50 years. The models are empirically based on a combination of flight tests under different runway states. However, since the models are empirically based, it is difficult to determine adjustments to the model due to conditions which are different than those for which the model was derived. In order to improve

the modeling and understanding of contaminated runways, this PhD thesis was proposed. As we will come to see, the focus of the PhD project shifted over time with the realities of modeling aircraft braking.

1.2   The Problem of Contaminated Runways

The majority of aircraft accidents and incidents occur during the take-off and landing phases. The pilot workload is at its highest and the margin for error is the lowest. When broken down into categories, runway excursions are the number one type of aircraft accident accounting for approximately 25% of all events. The majority of runway excursions occur during the landing phase as opposed to the take-off phase. During this work we will concentrate on the landing phase, however the braking modeling is equally applicable to take-off (for computation of the rejected take-off) or landing.

As with nearly all aviation accidents, runway excursions are due to a combination of factors. We show in Figure 1.1 how different factors can affect the landing distance. Using Figure 1.1, we demonstrate how several small factors can lead to a dangerous situation.

Example 1. *We take the case of an aircraft crossing the runway threshold with an additional 50ft of height, and 10 extra knots of airspeed. As the aircraft enters the final landing phase, the headwind of 5 knots reverses direction to a tail-wind of 5 knots. This causes the aircraft's ground speed to increase; the sudden change in velocity causes the pilot to extend his flare for 2 seconds. From Figure 1.1 we see that the additional height adds 20% to the landing distance, the extra airspeed 20%, the change in wind 30% and the long flare 30%. The combination of several small factors leads to a doubling of the landing distance which could be longer than the actual length of the runway (See Section 1.3 for Regulations regarding runway landing length). In Figure 1.2 we plot the principal factors that are involved in runway excursions. Contaminated runways leading to ineffective braking contribute to between 25 to 40% of runway excursions (the number vary depending on the source and the accidents in reference).*

Reference Distance (Dry)

1000 feet elevation

10-knot tailwind

Final Approach Speed + 10 knots

100 feet at Threshold

Long Flare

No Ground Spoilers

Wet Runway

Compacted Snow

Water and Slush

Ice

0   1.0   1.2   1.4   1.6   2.0   3.0   3.5

Multiplication Factor with Regards to Dry Reference Landing Distance

Figure 1.1: Factors that can affect the landing distance (Redrawn from [2])

The aviation authority for the USA, the FAA, defines a contaminated runway when 25% or more of the runway surface is covered with one or more of the following contaminants: ice, compacted or loose snow, or standing water. A contaminated runway affects the landing distance by reducing the available friction between the aircraft tire and the runway when braking. When an aircraft lands, there are three principal forces involved in stopping the aircraft: the braking force, the aerodynamic drag forces and the thrust (negative force if reverse thrust is used). We plot in Figure 1.3 the deceleration for a dry and snow runway and the percentage of the total stopping force due to each of the three components. We see that for a dry runway landing the aircraft can decelerate at $3.7 m/s^2$ and 80% of this deceleration is due to the braking force, whereas for a compacted snow runway the aircraft decelerates at approximately $2 m/s^2$ for which the braking is responsible for 65% of the deceleration. This reduction in the deceleration of nearly 50% causes the landing distance to nearly double. Correct knowledge of the runway state and its effect on the braking force is essential for a correct estimation of the distance needed to land.
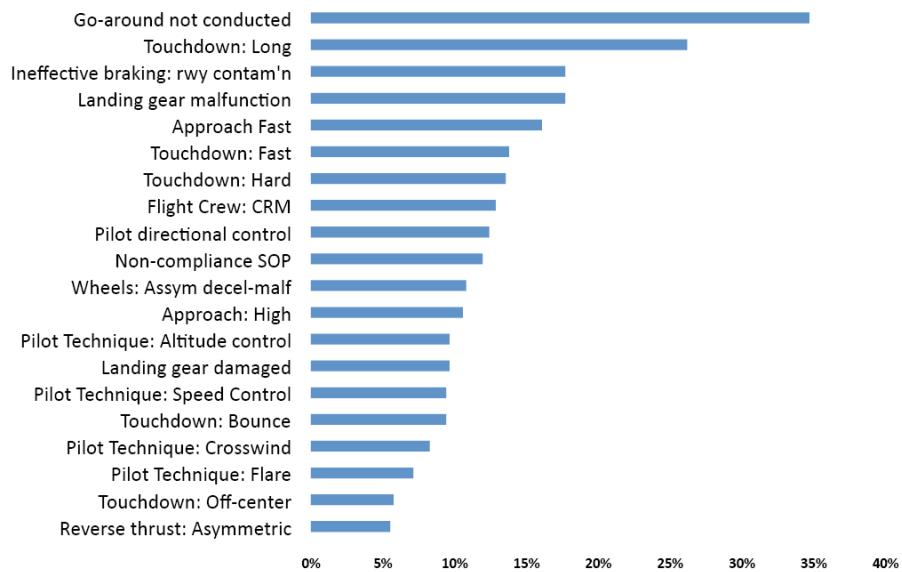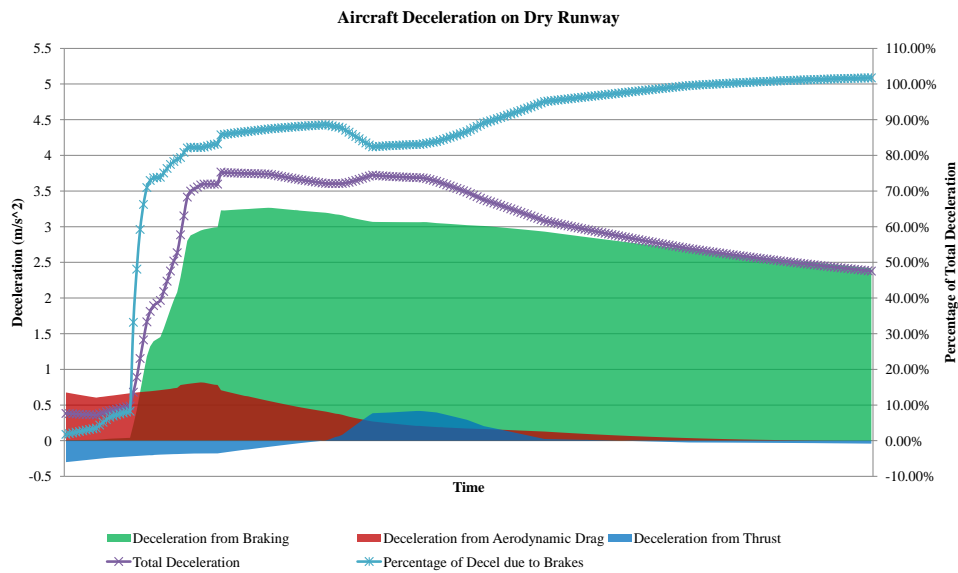

Figure 1.2: Contributing factors to runway excursions [4]

(a) Forces on a Dry Runway
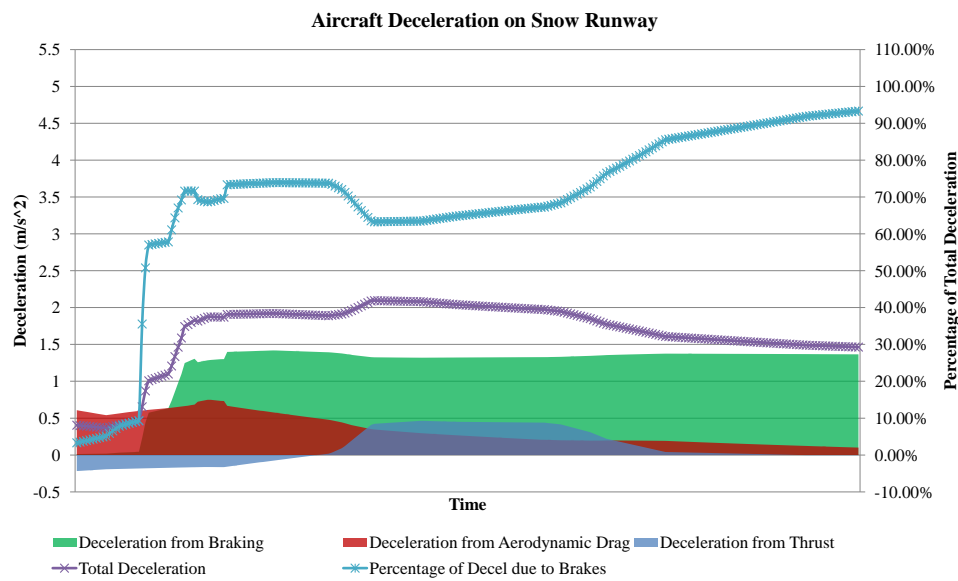
(b) Forces on a Snow Runway

Figure 1.3: The two figures show the contribution of each stopping force to the deceleration of the aircraft for a dry runway 1.3a and a snow covered runway 1.3b

1.3 Regulations

The regulations differ slightly depending on the aviation authority. The two largest aviation authorities that have the most influence are that of the United States, the Federal Aviation Authorities (FAA), and that of Europe, the European Aviation Safety Authorities (EASA). They set the rules for which all commercial aircraft must meet in order to remain airworthy. The regulations are harmonized for a large portion of the rules, however landing distances on contaminated runways remain slightly different, although harmonization is also sought in this area.

1.3.1 Certified Landing Distances

The first distance we describe is called the Actual Landing Distance (ALD). The rules are similar between Europe and the USA. The rules concerning the ALD are described in CS 25.125 and FAR 25.125 for EASA and the FAA respectively. During the certification of the aircraft, the ALD is demonstrated as the distance between a point 50ft above the runway threshold to the point where the aircraft comes to a complete stop. This distance must be determined for standard temperatures at each weight, altitude and wind for which the aircraft is approved for operation. This distance is certified and published in the Aircraft Flight Manual (AFM) for dry runways.

For contaminated runways, the regulations differ between EASA and the FAA. The FAA currently does not contain any regulations to determine the ALD on contaminated runways. Within the EASA regulations, CS 25.1591 demands that the manufacturer provide actual landing distances on contaminated runways if the aircraft is to be permitted to operate on such runways. AMC 25.1591 (Acceptable Means of Compliance) provides a methodology to determine the ALD on contaminated runways without performing specific flight tests. The AMC provides the coefficient of braking friction to be used for different runway states which can be used to calculated the ALD for contaminated runways and thus publish the distances in the AFM.

The next set of regulations must be followed by the airline company that wishes to operate the airplane. Known as the OPS regulations, they define the Required Landing Distance (RLD). Before an aircraft departs on a commercial flight, the company must calculate the aircraft's RLD, taking into account a prediction of the environmental conditions likely to be encountered upon arrival at the destination. The RLD must be less than the landing distance available (LDA) i.e. the length of usable runway. If this condition is not satisfied, the aircraft is prohibited from departing. The RLD regulations for a dry runway can be found in EU OPS 1.5151 and FAR 121.195 and 197 in EASA and the FAA respectively. It must be shown that the aircraft can land within 60% of the available runway. In other words, the

$RLD_{dry} = ALD_{dry}/0.6 \leq LDA$. For a wet runway, the EASA regulation is EU-OPS 1.520 and states that RLD wet must be 115% of the RLD dry. For contaminated runways, also cited in EU-OPS 1.520, the RLD contaminated must be the greater of the $ALD_{contaminated} \times 1.15 RLD_{wet}$.

1.4 Calculating Aircraft Performance

As cited in the regulations, the aircraft manufacturer must provide the ALD for all weights, aircraft configurations, and environmental conditions. The number of possible variations makes it unfeasible to flight test all the cases. Thus the manufacturer relies on a mathematical model of the aircraft performance that is validated with flight tests and certified as providing representative values. This model is based on a balance of forces. The force balance equation (neglecting any lift generaged by the wings) can be written as

$$Ma = T - D - F_b - mgsin(\gamma) \tag{1.1}$$

where M is the mass of the aircraft, a is the acceleration, T is the engine thrust, D is the aircraft drag, F_b is the braking force, g is gravity and γ is the runway slope. Knowing each of the components on the right hand side and the aircraft mass, we can determine the acceleration (or deceleration) of the aircraft at each time step. With the deceleration capability of the aircraft known, the distance needed to stop, d, can be calculated by

$$d = \frac{1}{2}\frac{V_i^2}{\bar{a}} \tag{1.2}$$

where V_i is the initial velocity at touchdown and $\bar{a}$ is the average deceleration during the landing. From this equation we note that the distance needed to stop is inversely proportional to the deceleration. A reduction in the deceleration capability of the aircraft by 50% leads to an increase of 100% of the landing distance.

Each of these components inside Equation 1.1 is modeled by Airbus. The braking force, F_b, can be modeled as

$$F_b = \mu F_z \tag{1.3}$$

where μ is the coefficient of braking friction and F_z is the weight on the braked wheels. The μ is the important component that determines how much friction force the contact between the tire and the runway can create to aid in stopping the aircraft.

1.4.1 Dry Runway Friction

The dry runway friction is determined during flight testing of the aircraft. Under a variety of aircraft and environmental conditions, maximum braking is applied during landing and the flight test results analyzed. By inversing equation 1.1 and using the deceleration measured during landing, the equation can be solved for μ. This is what is commonly called a μ_{global} in that it is the combined effects of all of the tires working together as well as the efficiency of the anti-skid system which regulates the brake pressure to obtain the maximum friction force. Using the combined results of several flight tests, an average μ_{dry} is obtained which is used in the aircraft model for determining the landing distances for all conditions.

1.4.2 Wet Runway Friction

Aircraft manufacturers are not obliged to certify the model for wet runways according to the EASA and FAA regulations (a wet runway is not considered contaminated). Nevertheless, Airbus publishes this information within the Aircraft Flight Manual (AFM) for operators to use. As there is no certification process, flight tests are not needed for aircraft *landing* on wet runways. However, the regulations do require the aircraft manufacturer to provide a model for the accelerate-stop distance (ASD) on wet runways. The accelerate-stop distance is the distance needed when the aircraft is on take-off and decides to abort the take-off and apply full brakes to stop the aircraft. The regulation for the ASD is provided in CS 25.109 and FAR 25.109. As the manufacturer must also provide this calculation for wet runways, the manufacturer has a choice to flight test on wet runways and determine a model, or they can use a predefined set of μ_{wet} runways described within the regulations. These μ_{wet} values are a function of the tire pressure and the velocity. In general, the μ_{wet} value decreases with increasing velocity and increasing tire pressure. We plot the μ_{wet} values as a function of velocity and tire pressure in Figure 1.4

The μ values are described as the maximum possible coefficient of friction. The manufacturer must then determine experimentally the efficiency of the anti-skid system on the airplane. That is to say, how well can the anti-skid system regulate the brake pressure to obtain the maximum possible global friction coefficient. There are several ways to perform this analysis, but they are out of the scope of this work. The final result is that the manufacturer determines the efficiency, η, of the system and multiplies this η value by the μ_{wet} values as defined by the certification regulations (See Table 1.1) to determine the effective friction value, $\mu_{effectivewet}$, to be used in the aircraft model.

$$\mu_{effectivewet} = \eta\mu_{wet} \qquad (1.4)$$
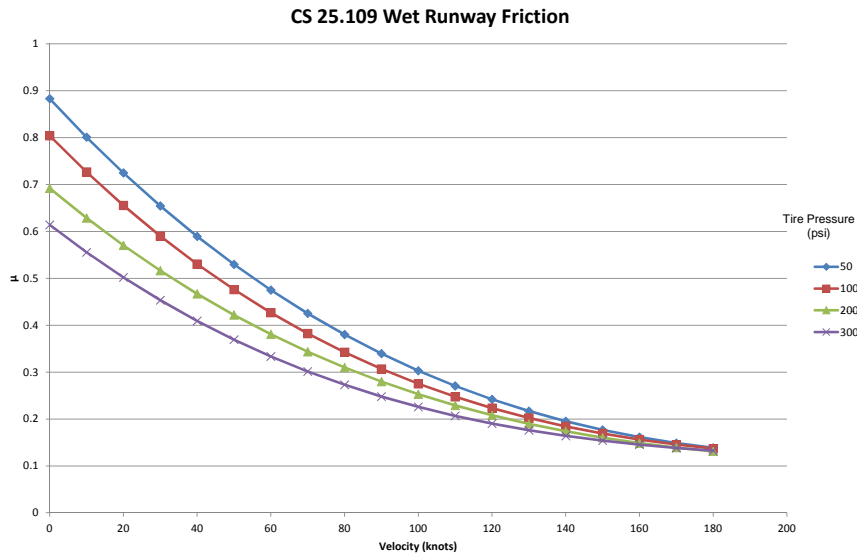
Figure 1.4: μ_{wet} s defined by the EASA Certification Regulations in CS 25.109 and shown in Table 1.1

As these μ_{wet} values are certified for the ASD distance, Airbus uses these values to publish landing distance on wet runways.

Table 1.1: μ_{wet} distance used to calculate the accelerate-stop distance as defined by the EASA Certification Regulations in CS 25.109. The values cited are also plotted in Fig 1.4

Tire Pressure (psi)	μ wet
50	$\mu = -0.0350(V/100)^3 + 0.306(V/100)^2 - 0.851(V/100) + 0.883$
100	$\mu = -0.0437(V/100)^3 + 0.320(V/100)^2 - 0.805(V/100) + 0.804$
200	$\mu = -0.0331(V/100)^3 + 0.252(V/100)^2 - 0.658(V/100) + 0.692$
300	$\mu = -0.0401(V/100)^3 + 0.263(V/100)^2 - 0.611(V/100) + 0.614$

1.4.3 Contaminated Runways

We recall a wet runway is not considered contaminated. When the standing water depth exceeds $3mm$, the runway state ceases to be considered wet and is considered contaminated. As mentioned previously, aircraft landing performance on contaminated runways is currently only covered in the EASA regulations. Under EASA certification, the aircraft manufacturer is not obliged to provide information on contaminated runways in order to certify an aircraft. However, if this information is not provided, the AFM must
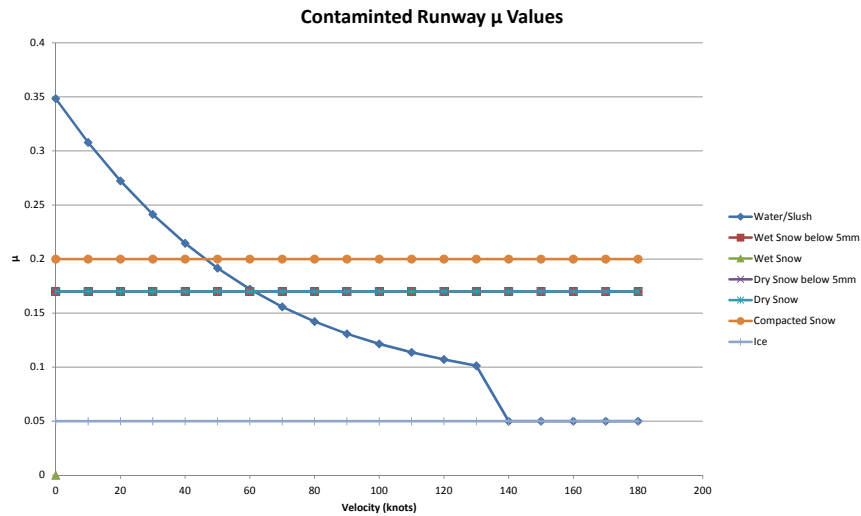
Figure 1.5: μ values for different contaminated runways states as defined in EASA Certification Regulations – AMC 25.1591

contain a statement that prohibits the operation of the aircraft on contaminated runways. This information is provided in CS 25.1591. Similar to the case of wet runways, the manufacturer has the choice to perform flight tests on different contaminated runway surface types and determine their own μ value as done for dry runways or the manufacturer can use the predefined μ values described in AMC 25.1591.

The AMC contains information on the different effects to take into account for the aircraft model. These include different drag effects such as displacement drag (drag associated with pushing the water out from in-front of the wheels), projection drag (drag associated with water spray impacting airframe)and compression drag (energy absorbed as the tire compresses loose snow) as well as several other effects such having multiple wheels in a row and the hydroplaning effect. All of these effects must be taken into account in the aircraft model. Of interest for this PhD work are the cited μ values for different runway states. These μ values are summarized in Figure 1.5. *The values cited in the regulations are considered to contain the anti-skid efficiency directly in the μ values. As such, no determination of the anti-skid efficiency on contaminated runways is necessary.*

1.5 Industry Initiative

As mentioned in Section 1.2, runways excursions are the most common type of aircraft accident. In the last ten years, the issue of runway excursions has been brought to the forefront and several initiatives have been launched to raise awareness and combat this problem. Numerous tools have been

developed such as the Runway Safety Initiative (RSI)[4], the Approach and Landing Accident Reduction (ALAR) toolkit[3], the EASA Runway Friction Characteristics and Aircraft Braking (RuFAB) project [9] as well as numerous safety reports and conferences put on by the aviation authorities in countries such as Canada, Norway, USA and Australia to name a few.

1.5.1 TALPA

One of the largest initiatives was an advisory rule making committee launched by the FAA in 2006 known as TALPA which stands for Take-off and Landing Performance Assessment. As mentioned earlier, the FAA previously did not have specific rules regarding aircraft performance on contaminated runways. In addition, there have been concerns in the industry regarding the representativeness of the actual landing distances (ALDs). The ALD's that are certified and published in the aircraft flight manual are derived from flight tests performed with experienced flight test pilots. These distances represent the maximum capability of the aircraft, but do not reflect the normal day to day operations and the varying skills that commercial pilots have. Problems were also identified regarding the calculation of the required landing distances (RLDs). The RLDs are calculated far in advance of the actual landing and thus contain a prediction of the environmental conditions to be encountered. Winds often change direction and force which can greatly affect an aircrafts performance, although a pilot is expected to recalculate the ALD if the conditions have significantly changed from the first calculation. In addition, the RLD's do not take into account temperature variations nor the runway slope unless it is greater than $\pm 2°$.

The decision was made to provide the pilots with an Operational Landing Distance (OLD). This operational landing distance has several changes with regards to the actual landing distance with the result that the distance is more representative of the performance achievable by a regular pilot under operational conditions. The OLD does not replace the RLD that is calculated before the aircraft takes-off but instead is calculated by the pilot in the air before landing taking into account the latest environmental and aircraft conditions. In addition, the OLD takes into account the effect of runway temperature and runway slope. The recommendation is that a safety margin of 15% be applied to the OLD distance to provide an additional safety buffer. This new landing distance is known as a factored landing distance (FOLD) e.g. $FOLD = 1.15OLD$.

In addition to the aircraft operation being more representative of a line pilot, runway contamination calculation was taken into account in a similar manner to that of the EASA regulations. Some small changes were made to the contaminated runway state μ values based on new research. The new TALPA runway states are defined for different runway codes of which several runway states can fall under the same code. The μ values for the
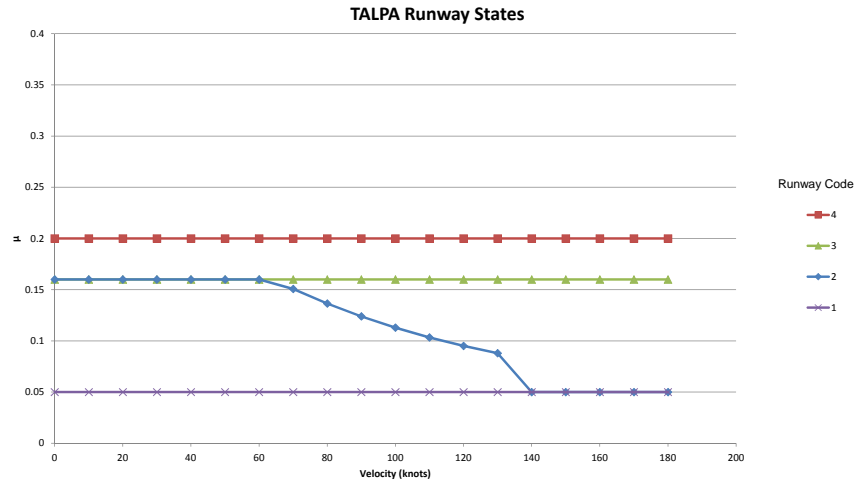
Figure 1.6: μ values for different contaminated runways states as currently defined in TALPA

runway codes are shown below in Figure 1.6. The correspondence between the runway code and the runway states is shown in Figure .

The new TALPA rules have not yet been published as regulations by the FAA and as such are subject to change. In addition, the European authorities have not yet decided the direction they will take with regards to Operational Landing Distances. Consequently, there is still considerable uncertainty regarding the future of operations on contaminated runways.

1.6 Friction Coefficient as a function of Slip Ratio

This section is very important in the understanding of the different terminology used regarding μ in the aircraft world as well as the role of the anti-skid system. Thus far, the μ values presented for determining aircraft performance have been what is often referred to as a μ_{global}. This term is also often called a global friction coefficient, but the term friction coefficient is inaccurate as a coefficient of friction normally refers to two objects in relative sliding motion. We will see in the derivation of the friction model (Chapter 2) that there are additional forces than just the sliding friction that contribute to the tire braking.

A more appropriate term for μ_{global} may be *normalized braking force* in that it is simply the total stopping force produced by the tire divided by the weight on the braked tire. However, the terminology using μ is prevalent in industry, thus this terminology will be kept. In the derivation of the friction model we differentiate the coefficients of friction by using the term *static and dynamic coefficients of friction* represented by the symbol μ_s and μ_k respectively.

The μ_{global}, as it is employed, contains the functioning of the anti-skid system. The curve plotted in Figure 1.7 represents a fundamental curve that will be used throughout this work. It is commonly referred to as the $\mu - slip$ curve and it plots the μ as a function of the slip ratio. The slip ratio is a measurement of the amount of braking. As more force is applied by the brakes, the angular velocity of the wheel, ω, slows down with respect to the absolute velocity of the wheel axle, V_x. It is this difference in speed that creates the frictional forces. The slip ratio can be defined by

$$s_x = \frac{V_x - \omega R_R}{V_x} \qquad (1.5)$$

where R_R is the rolling radius of the wheel. This equation will be developed in more detail in Chapter 2. A slip ratio, s, of zero means that the tire is free-rolling i.e. no braking is being applied. A slip ratio of 1 implies that the wheel is blocked i.e. the angular velocity is zero and the tire is purely sliding with a velocity of V_x. The form of this curve is important, we see that the curve reaches a maximum values and then begins to decrease as the slip ratio increases. This maximum values (0.45 in the example in Figure 1.7) is important in tire braking and anti-skid design. The max is known as the maximum obtainable friction coefficient and the s associated with this value is known as the optimal slip ratio (0.1 in the example in Figure 1.7). This point is the goal of the anti-skid system. The anti-skid system regulates the brake pressure (and inherently the slip ratio) to obtain the maximum braking coefficient. The wheel tends to fall into a skid (blocked wheel) when on the right hand side of the optimal slip ratio. This side is known as the unstable side. Thus the anti-skid systems tries to maintain the slip-ratio on the left (stable) side of the optimal slip ratio while obtaining the maximum friction possible. The efficiency of the anti-skid system is demonstrated by the systems ability to obtain and maintain a friction coefficient close to that of the max. If the wheel begins to fall into a skid (evidenced by a rapidly reducing angular velocity of the wheel), the system reduced the braking pressures to allow the wheel to spin-up and return to the stable side of the curve, after which point it re-applies braking pressure.

As we have seen, the μ values currently used for calculating aircraft performance are either constant values (for snow and ice) functions of velocity (dry, wet and water/slush) and functions of tire pressure (for wet, water and slush). **In all of these cases, we do not define μ as a function of the slip ratio.** For dry runways, the μ value is determined experimentally thus it implicitly contains the functioning of the anti-skid system. For wet runways, we include and efficiency factor η in the μ and for contaminated runways, the predefined μ values are thought to be conservative and contain implicitly the anti-skid functioning. *In order to determine the true impact of contaminated runways, we need to be independent of the anti-skid system. Knowing the shape of the $\mu - slip$ curve for all environmental and*
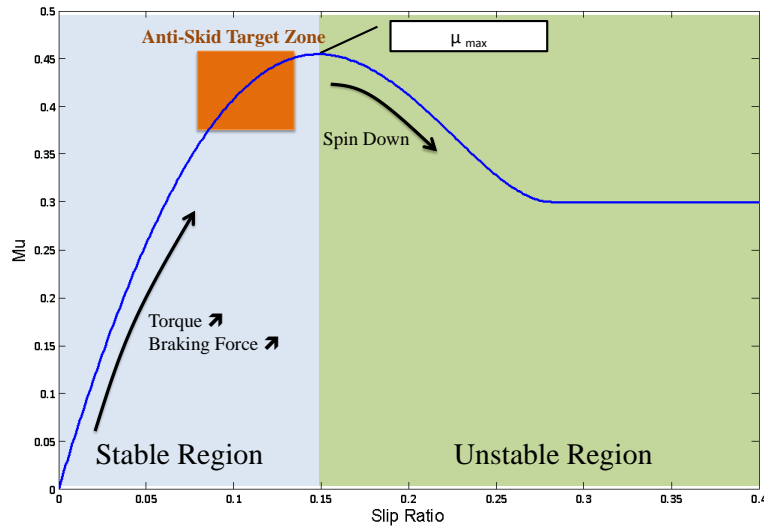
Figure 1.7: General form of the $\mu - slip$ curve showing the stable and unstable sides of the curve as well as the target zone for the anti-skid system.

aircraft conditions provides significantly more information as to the effect that contaminated runways has on the braking.

1.7 The Need for a Better Model

Research into tire friction, most notably into the automobile world where more research has been done regarding tire friction, unveils numerous factors that are known to affect tire friction that are not taken into account in the aeronautical industry. Due to the nature of the rubber used in tires, effects such as temperature, rubber type and contact pressure will change the frictional properties. In addition, the texture of the runway plays an important effect in creating frictional forces. These are effects that are not completely understood and thus not taken into account in aircraft modeling.

Aircraft land throughout the world at all times of the year. What effect does landing in Dubai in the middle of the summer have, as opposed to landing in the north of Canada in the middle of winter. How does a ambient temperature change of 80°C affect friction. If some of the tires are partially deflated during landing, will this degrade the friction? Runway characteristics; how does the friction differ if the runway has recently been resurfaced as opposed to an old worn runway? These are all characteristics that affect friction, but the manner in which they change the aircraft's landing performance is unknown.

Currently in the aeronautical industry, little exists in terms of modeling

friction and the unique characteristics that are present for aircraft operating conditions. For inspiration, we focused on the automobile world and the types of models used in this industry. Modeling of the $\mu - slip$ curve is prevalent among all of actors in the automobile industry: brake, tire and car manufacturers. The models differ in complexity and the amount of knowledge needed to implement the models.

1.7.1 The Brush Model

A model that is common is known as the Brush Model due to its simplicity to implement. As the model is based on the physics of the interactions occurring at the tire-runway contact surface, the model serves as a good base and starting point. The model can be developed with simple assumptions and then built upon to include more complex effects. The Brush Model is also mathematically low-cost to implement as opposed to a finite element model which allows for rapid computation time and possible integration into real-time systems.

1.7.2 Modeling Dry Runway Friction

As mentioned at the beginning of the report, the end goal of this research is to obtain a better model that can predict the aircraft landing distances on contaminated runways. To do this, we must obtain a better model of the coefficient of friction which is the principal force involved in stopping the aircraft. The model should be based on the physical phenomena that occurs in the tire-runway contact zone. The Brush Model is an accepted methodology to model that is commonly used in the automotive industry. However, before we can use this model for contaminated runways, this model must be adapted to the particular characteristics present in the aeronautical environment. We will derive and validate the Brush Model for the case of dry runway braking friction. The availability of flight test data on dry runways and the simpler contact physics are more adept to model validation.

The amount of work involved in using the Brush Model as a friction model for dry runway landings proved to be considerable. We derived the basic brush model, and then went beyond the basic derivation to better understand the complex physical interactions which occur in the contact zone. We used advanced Tribology, Material Science and Strength of Materials to build a more complete Brush Model capable of taking dynamic factors into account.

Due to the amount of work involved in developing the Brush Model for use in the aircraft model, the specific cases of contaminated runways were not fully explored. However, as the model is based on the tire-runway contact physics, the core work can be expanded to cover contaminated runways with a proper understanding of the contact physics involved on contaminated

runways.

1.8   Conclusion

The following Chapters will deal with the derivation of the Brush Model (Chapter 2), the understanding of the complex interactions of the tire and the runway (Chapters 3 through 6) and finally a validation of the Brush Model by comparison with flight test data (Chapters 7 through 9).

Figure 1.8 presents schematically the work that will follow for Part II of this work, the Brush Model. We will derive the Basic Brush Model in Chapter 2. Chapters 3 through 6 will expand the Brush Model and develop the relationships that different scientific branches bring to the Brush Model. We see that the Science of Tribology permits to develop the sliding friction between the tire and the runway. The Strengh of Materials permits to characterize the tire behavior under various loading and conditions. Both the tire behavior and the sliding friction will depend on Material Science. The mechanical properties of rubber vary extensively depending on environmental conditions and thus the Material Science will determine the representativeness of the Brush Model.
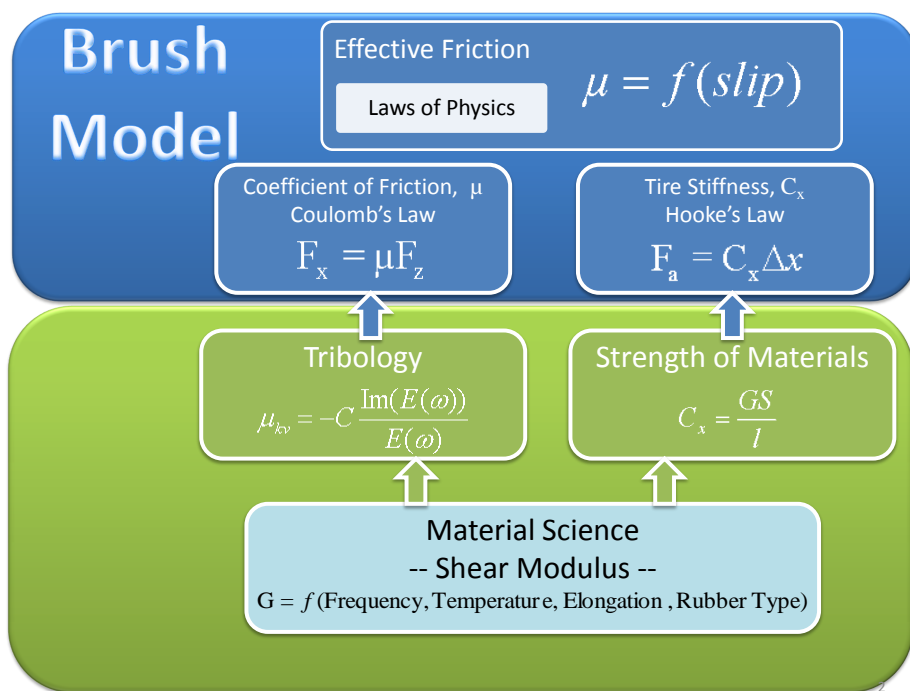
Figure 1.8: Outline of the work done in the derivation of the Brush Model

Part II

Brush Model

Chapter 2

The Brush Model

Summary. Ce chapitre présente le modèle de la brosse qui sera utilisé pour modéliser les forces de frottement produites par le pneu lors du freinage. Le modèle de la brosse est une approche théorique de la modélisation pneu-surface basée sur deux lois physiques : la loi de Coulomb sur le frottement de glissement et la loi de Hooke sur l'élasticité. Le modèle de la brosse repose sur une division de la zone de contact en un nombre infini de poils de brosse. Le mouvement et la force de chaque poil sont calculés au moment où il traverse la zone de contact et la force totale de frottement s'obtient en sommant tous les efforts générés à chaque poil pour un moment donné. Nous pouvons décrire comme suit le mouvement d'un poil quand il se déplace sur la zone de contact :

– Quand le poil entre dans la zone de contact en partie avant de la roue, il adhère à cette de surface contact (Point $-a$ Figure 2.1).
– Quand la carcasse du pneu traverse la zone de contact, le poil commence à s'allonger élastiquement et produit alors des forces résistives dues à la déformation du poil, conformément à la loi de Hookes $F_{ax} = C_x \Delta x$.
– À un certain point le long de la zone de contact, cette force d'adhérence est supérieure au coefficient de frottement statique entre le poil et la surface (Point x_s, Figure 2.1).
– C'est à ce point, dit point de transition, que le poil commence à glisser le long de la zone de contact, produisant des forces résistives dues au glissement, conformément à la loi de Coulomb $F_{sx} = \mu_{sx} F_z$
– La somme de ces deux forces, la force d'adhérence et la force de glissement, forme la force de freinage du pneu $F_x = F_{ax} + F_{sx}$.

Pour les études de freinage des avions, nous nous intéressons tout d'abord au déplacement dans la direction longitudinale. À ce titre, pour simplifier la dérivation du modèle de la brosse, nous supposons l'absence de mouvement dans la direction latérale. La forme finale du modèle de la brosse est illustrée page 50. Le modèle calcule la force de frottement dans la zone de contact

pneu-piste sous la forme d'un polynôme du 3e degré du glissement, σ_x. Les autres paramètres utilisés pour construire le modèle de la brosse sont la longueur de la zone de contact, $2a$, la charge verticale sur l'axe de la roue, F_x, la rigidité longitudinale du pneu, c_{px}, et les coefficients de frottement statique et dynamique, respectivement μ_{sx} et μ_{kx}. Nous effectuons alors une analyse de sensibilité de la forme finale du modèle de la brosse en faisant varier chaque paramètre et en examinant l'effet de cette variation sur la forme du modèle. Nous traçons ensuite le modèle de la brosse sous la forme communément utilisée dans l'industrie, c'est-à-dire la force de frottement F_x en fonction du taux de glissement longitudinal, σ_x. Cette courbe est illustrée page 52. À l'aide de l'équation du modèle de la brosse, nous dérivons plusieurs points clés sur la courbe $\mu - slip$, notamment la force de frottement maximale, la pente initiale de la courbe et le taux de glissement longitudinal optimal. Nous terminons le chapitre par une rapide discussion sur le besoin d'un développement ultérieur du modèle de la brosse. Cette forme du modèle de la brosse comporte trois inconnues qui doivent être définies afin d'utiliser pleinement le modèle. Ces trois inconnues sont la rigidité du pneu, c_{px}, et les coefficients de frottement, μ_{sx} et μ_{kx}. Les chapitres suivants sont consacrés à l'étude de ces paramètres.

2.1 Introduction

The brush model theoretical approach to tire-surface modeling is characterized by using two basic physical laws: Coulomb's law of sliding friction, $F_{sx} = \mu_{sx}F_z$, and Hooke's law of elasticity, $F_{ax} = C_x\Delta x$. The brush model is based on the premise of dividing the contact zone into an infinite number of brush elements (or bristles) much like of a comb. By following the movement of a bristle through the tire-surface contact zone and calculating the resistive forces at each step, the forces generated in the entire contact zone can be determined by summing the effect of the bristles. The concept of the brush model is that the effects of the two physical laws causes the contact zone to be partitioned into two zones, an adhesion zone, governed by Hooke's law, and a sliding zone, governed by Coulomb's law. Figure 2.1 shows the bristle concept and we can describe the movement of a bristle as it moves through the contact zone as follows.

  – When a bristle first enters the contact zone at the front of the wheel, the bristle adheres to the contact surface (Point $-a$ in Figure 2.1).
  – As the tire carcass traverses the contact zone, the bristle begins to stretch elastically thus generating resistive forces due to the deformation of the rubber bristle by Hookes' Law $F_{ax} = C_x\Delta x$.
  – At a certain point along the contact zone, this adhesive force surpasses the static coefficient of friction between the rubber bristle and the surface (Point x_s in Figure 2.1).

– It is at this point, the transition point, where the bristle begins to slide along the contact zone, generating resistive forces due to sliding by Coulomb's Law $F_{sx} = \mu_{sx} F_z$
– The sum of these two forces, the force due to adhesion and the force due to sliding which form the braking force of the tire $F_x = F_{ax} + F_{sx}$.
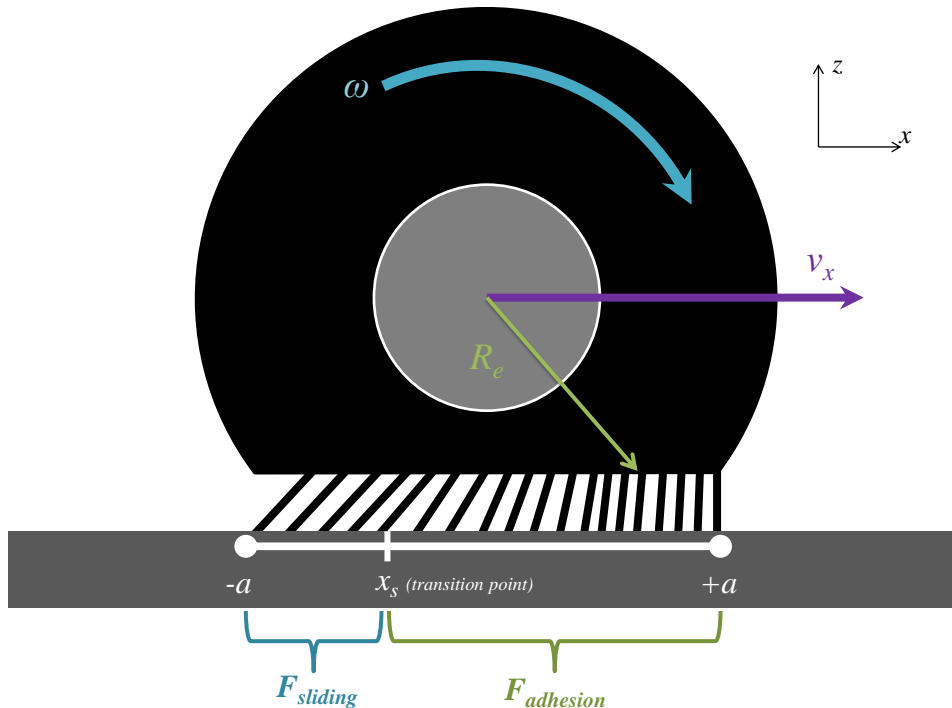
Figure 2.1: Cut-away view of the tire and 'bristles'. The tire-axis is moving forward with a horizontal speed v_x while the tire is rolling with a circumerfential speed $v_c = \omega R_e$

2.2 Fundamentals

Before beginning with the derivation of the brush model, the coordinate system, notations and definitions must be clearly defined. The general formation of the brush model has followed the methodology as outlined by Svendenuis [24]. However some minor changes have been made regarding the coordinate system and notations.

2.2.1 Coordinate System

Tire kinematics are defined using the xyz coordinate system as seen in figure 2.1. The x-axis is defined as the longitudinal direction aligned with

the wheel heading, the lateral y-axis perpendicular to the wheel plane, and the vertical z-axis to be upwards in accordance with the ISO-standard. This coordinate system was chosen so that the signs of each parameter retain a physical sense. The coordinate system is moving with the tire and is fixed at the tire axis, so that the tire axis is always the point $x, y, z = 0$.

Friction is defined as a force which resists the relative motion of two surfaces. When braking, the sliding direction is in the positive x direction resulting in a friction force in the negative x-axis. In the same way, during traction (acceleration), for the case of an automobile, the sliding velocity in the tire-surface contact zone is in the negative x direction resulting in a traction force in the positive x-axis. The coordinate system also gives the normal force F_n acting in the positive z-axis.

2.2.2 Notation

Variables are often defined in vector form denoted by a bar such as $\bar{v}$ where $\bar{v} = (v_x, v_y, v_z)$, x, y and z referring to the longitudinal, lateral and vertical components respectively.

Subscripts are chosen to stay consistent with the physical processes involved in the brush model.

– subscript s - denotes sliding
– subscript a - denotes adhesion
– subscript x, y or z denotes direction the variable is acting in

2.2.3 Definitions

Tire Slip

The tire slip is the basis for the development of braking friction forces between the tire and the runway. The tire slip can be defined in several different forms but its components include the absolute wheel travel velocity, $\bar{v}$, defined at the wheel axis, the circumferential velocity $v_c = \omega R_R$ where ω is the wheel angular velocity and R_R is the effective rolling-radius of the tire, and the sliding velocity defined as the difference between the wheel travel velocity and the circumferential velocity $\bar{v}_s = (v_x - v_c, v_y)$.

The most commonly used form of tire slip in the aeronautical industry is the *slip ratio s* defined as

$$\bar{s} = (s_x, s_y) = \frac{\bar{v}_s}{\bar{v}} \tag{2.1}$$

Using this definition of slip will produce values between 0 and 1 (or 0-100%), where 0 represents a free rolling wheel ($v_c = v_x$) and 1 represents a locked wheel with no circumferential velocity ($v_c = 0$).

In the brush model however, a different form of tire slip will be used that relates the *sliding velocity* to the *circumferential velocity*. This definition will

become clear during the brush model derivation.

$$\bar{\sigma} = (\sigma_x, \sigma_y) = \frac{\bar{v}_s}{v_c} = \frac{\bar{s}}{\sqrt{1 - s_y^2 - s_x}} \tag{2.2}$$

These definitions can also be related to each other

$$\bar{\sigma} = \frac{\bar{s}}{\sqrt{1 - s_y^2 - s_x}} \tag{2.3}$$

$$\bar{s} = \frac{\bar{\sigma}}{\sqrt{(1 + \sigma_x)^2 + \sigma_y^2}} \tag{2.4}$$

Due to the fact the brush model derivation will be applied in the longitudinal sense only, we can simplify these terms

$$s_x = \frac{v_x - v_c}{v_x} = \frac{\sigma_x}{1 + \sigma_x} \tag{2.5}$$

$$\sigma_x = \frac{v_x - v_c}{v_c} = \frac{s_x}{1 - s_x} \tag{2.6}$$

Tire/Rubber Stiffness

As mentioned in section 2.1, the adhesion force generated in the contact zone is due to the deformation of the bristle. This is similar to the deformation of a spring and can be described by Hooke's Law of Elasticity

$$F_x = -C_x \Delta x$$

where Δx is the displacement, F_x is the spring force and C_x is the *spring constant*. In the case of a tire, the spring constant is represented by the tire-stiffness. The *tire stiffness* can be determined by performing a deflection test on the tire. The experimental procedure requires that a vertical weight be placed on a tire with a known internal (gauge) pressure. An increasing horizontal force is placed at the wheel center, and the corresponding deflection of the wheels center is measured. The horizontal force is increased and the measurement repeated until a force vs deflection curve is plotted. The typical form of this curve is shown in Figure 2.2. This process can be repeated for varying vertical forces and tire pressures.

The *tire stiffness* (or *spring constant*) is then determined as the slope derived from the force-displacement curves.

$$C_x = \frac{\Delta F_x}{\Delta x}$$

Note: C nominally has the units N/m.
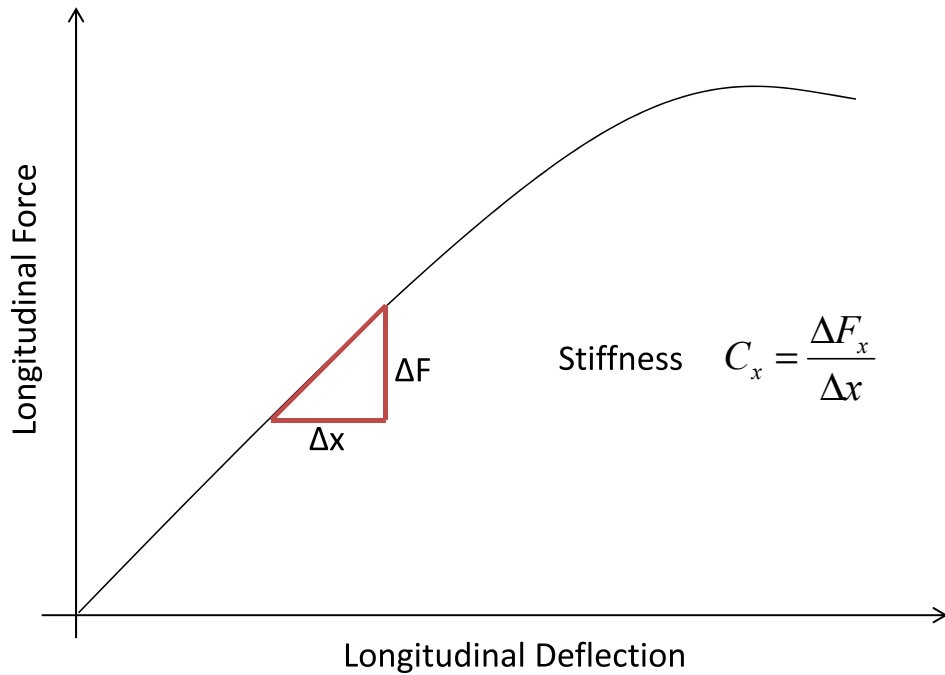
Figure 2.2: Typical form of the curve obtained from longitudinal tire-stiffness tests

The brush model method is based on determining the forces involved for one bristle and then integrating along the contact zone. The coefficient of stiffness obtained above is the stiffness produced by the contact zone it its entirety. To obtain the stiffness provided per unit length of the contact patch, we define the Bristle stiffness, c_{px} as

$$c_{px} = \frac{C_x}{2a}$$

where C_x is the total stiffness determined by longitudinal stiffness tests and a is one half of the length of the contact zone

2.3 Derivation of the Brush Model

The following is a basic derivation of the brush model with several assumptions as outlined in the text. The brush model is applicable for combined slip in both the lateral (y) and longitudinal (x) directions. Nevertheless, due to the fact that aircraft braking is primarily in the longitudinal axis, we ignore the lateral sense and derive the brush model considering only longitudinal motion.

2.3.1 Adhesive Zone Forces

To determine the forces generated in the adhesive zone we follow the movement of one bristle as it moves through the adhesive zone (Figure 2.1). The contact area has a length of 2a and is centered at $x = 0$. The model is simplified in the lateral, y, direction. The bristles are assumed to have the same width as the tire contact area. Variables in the lateral direction are assumed to be constant including: tire pressure, tire-stiffness and tire width.

We must first be able to calculate the position of *a bristle* and its deformation for any point in the contact zone. To do this, we first define an arbitrary time t_c which represents the amount of time since the bristle first entered the contact zone. We recall that the coordinate system is fixed to the tire axis and thus is moving in space at a velocity v_x. We also recall that the moment a bristle enters the contact zone (at $t = 0$) it adheres (or sticks) to the surface. There is no relative movement between the bristle and the surface but the point of contact is moving with reference to the coordinate system which is fixed at the wheel axle and moving at a velocity v_x (See Figure 2.3).

Thus the point x_r representing the point of contact between the surface and the bristle, can be described in our moving coordinate system for any time, t_c as

$$x_r(x) = a - \int_0^{t_c(x)} v_x dt \qquad (2.7)$$

However the bristle has a known height and the top of the bristle is moving at a difference speed, v_c with reference to the coordinate system due to the circumferential speed of the tire, ω. Thus we can determine the position of the top of the bristle, x_c for a given time, t_c by taking into account the circumferential velocity of the tire, v_c (where $v_c = \omega R_R$) by

$$x_c = a - \int_0^{t_c(x)} v_c dt \qquad (2.8)$$

Therefore the deformation that the bristle has undergone is the difference between the x-positions between the top and the bottom of the bristle

$$\Delta_x(x) = x_r(x) - x_c = -\frac{v_x - v_c}{v_c}(a - x) = -\sigma_x(a - x) \qquad (2.9)$$

Using the deformation obtained in equation 2.9 we can calculate the force generated by this bristle using the stiffness, c_{px}, of the bristle. Therefore the force generated by one bristle found at position x along the contact zone is

$$dF_{ax}(x) = c_{px}\Delta_x(x)dx \qquad (2.10)$$
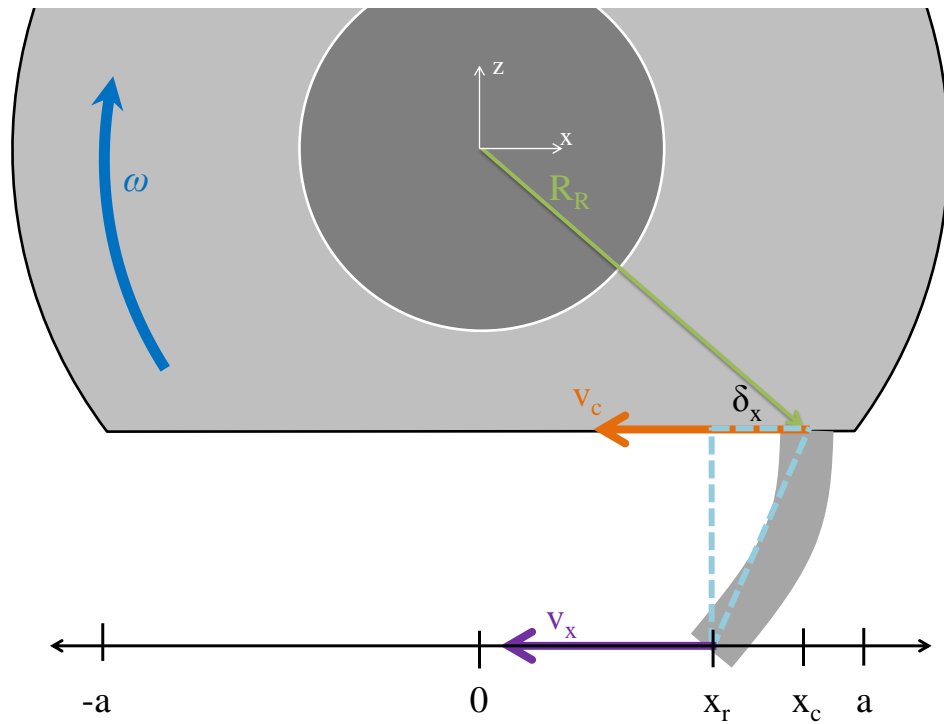
Figure 2.3: Computing the deformation of a bristle as a function of the circumferential and horizontal speeds using a moving coordinate system fixed at the tire-axis

As a result, to find the total force produced in the adhesion zone, we sum the deformation forces of each bristle in the adhesion zone. To do this we must know the size of the adhesion zone, so we designate the point x_s as the transition point between the adhesion zone and the slipping zone. Integrating over the adhesion zone

$$
\begin{aligned}
F_{ax} &= \int_{x_s}^{a} dF_{ax}(x) \\
&= -c_{px}\sigma_x \int_{x_s}^{a} (a - x)\, dx \\
&= -c_{px}\sigma_x \left[ax - \frac{x^2}{2} \right]_{x=x_s}^{x=a} \\
&= -c_{px}\sigma_x \left(a^2 - ax_s - \frac{a^2}{2} + \frac{x_s^2}{2} \right) \\
&= -c_{px}\sigma_x \left(\frac{1}{2}a^2 - ax_s + \frac{1}{2}x_s^2 \right) \\
&= -\frac{1}{2}c_{px}\sigma_x \left(a^2 - 2ax_s + x_s^2 \right) \\
&= -\frac{1}{2}c_{px}\sigma_x \left(a - x_s \right)^2 \qquad\qquad (2.11)
\end{aligned}
$$
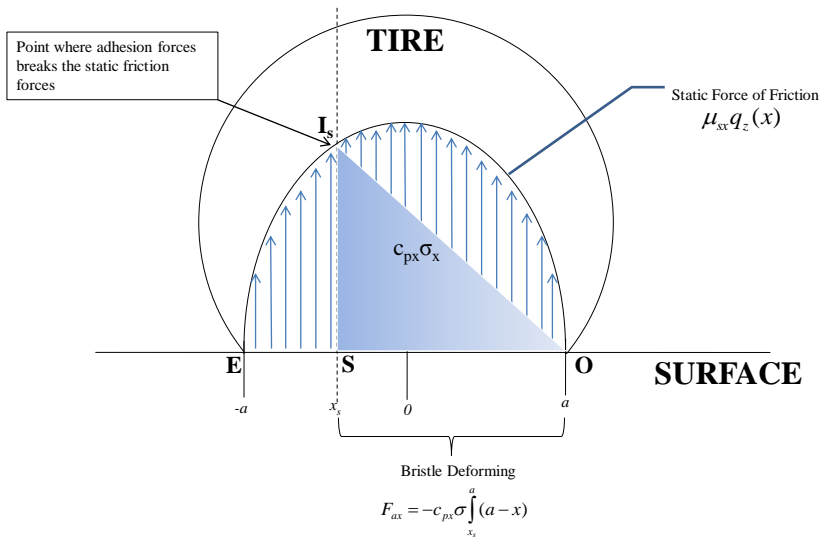
Figure 2.4: Schematic of the adhesion zone. The slope of the line IO is equal to $c_{px}\sigma$. The total adhesive force is equal to the area OSI_s.

2.3.2 Adhesion Zone to Sliding Zone Transition Point

The next step is to determined the transition point x_s. Conventional sliding physics define two types of friction: static and kinetic. Static friction arises from the interlocking of irregularities at the contact point between the tire and the runway. The static friction coefficient is calculated based on the force needed to break these bonds and move an object that was initially at rest. Kinetic friction is calculated based on the frictional force developed during sliding. For these cases of friction we apply Coulomb's law

$$F_x = \mu F_z \tag{2.12}$$

where μ can either be μ_s in the case of static friction or μ_k in the case of kinetic friction.

In order to remain consistent with the signs it should be recalled that the friction force is a resistive force which is always opposite the direction of relative motion of the sliding surface. Thus the form of equation (2.12) can be written as

$$F_x = -\mu \frac{v_{s_x}}{|v_{s_x}|} |F_z| \tag{2.13}$$

and for the calculation of the friction coefficient μ_{global}

$$\mu_{global} = -\frac{F_x}{F_z} \frac{|v_{s_x}|}{v_{s_x}} \tag{2.14}$$

In the case of braking, the sliding speed v_{s_x} is in the positive x-direction, resulting in a friction force F_x in the negative $x-direction$ which is consistent with braking.

To calculate the transition point x_s recall that in the adhesion zone there is no sliding motion between the bristle and the runway. However as the bristle moves through the contact zone, the deformation of the bristle increases and consequently the adhesive force at the contact point increases. The transition point x_s is found at the point where the force due to adhesion is equal to the force necessary to break the static friction.

$$dF_{ax}(x_s) = -\mu_{sx} q_z(x_s) \tag{2.15}$$

Pressure Distribution - $q_z(x)$ In the basic brush model, we will define a distribution of pressure along the contact zone. Assuming that the pressure distribution is constant in the lateral axis, we define a parabolic distribution along the longitudinal contact zone as follows

$$q_z(x) = \frac{3F_z}{4a} (1 - (\frac{x}{a})^2) \tag{2.16}$$

Inserting equations (2.9), (2.10) and (2.16) into the transition point equation (2.15)we find

$$- c_{px}\sigma_x(a - x_s) = \frac{3F_z(-\mu_{sx})}{4a}(1 - (\frac{x_s}{a})^2) \qquad (2.17)$$

and rearranging for x_s

$$x_s = \frac{c_{px}\sigma_x 4a^3}{3F_z\mu_{sx}} - a \qquad (2.18)$$

In order to simplify the equations we will introduce a normalized slip value defined as

$$\bar{\sigma} = \frac{c_{px}\sigma_x 2a^2}{3F_z\mu_{sx}} \qquad (2.19)$$

Thus our equation for x_s becomes

$$x_s = (2\bar{\sigma} - 1)a \qquad (2.20)$$

Inserting the transition point x_s into equation (2.11) we obtain the the frictional force produced in the adhesion zone.

$$
\begin{aligned}
F_{ax} &= -\frac{1}{2}c_{px}\sigma_x \left(a^2 - 2ax_s + x_s^2\right) \\
&= -\frac{1}{2}c_{px}\sigma_x \left(a^2 - 2a(2\bar{\sigma} - 1)a + ((2\bar{\sigma} - 1)a)^2\right) \\
&= -\frac{1}{2}c_{px}\sigma_x a^2 \left(1 - 2(2\bar{\sigma} - 1) + (2\bar{\sigma} - 1)^2\right) \\
&= -\frac{1}{2}c_{px}\sigma_x a^2 \left(1 - 4\bar{\sigma} + 2 + 4\bar{\sigma}^2 - 4\bar{\sigma} + 1\right) \\
&= -\frac{1}{2}c_{px}\sigma_x a^2 \left(4 - 8\bar{\sigma} + 4\bar{\sigma}^2\right) \\
&= -2c_{px}\sigma_x a^2 \left(1 - 2\bar{\sigma} + \bar{\sigma}^2\right) \qquad (2.21)
\end{aligned}
$$

Finally by substituting in $\bar{\sigma}$ (from Eq. 2.19)we obtain

$$
\begin{aligned}
F_{ax} &= -2c_{px}\sigma_x a^2 \left(1 - 2\left(\frac{c_{px}\sigma_x 2a^2}{3F_z\mu_{sx}}\right) + \left(\frac{c_{px}\sigma_x 2a^2}{3F_z\mu_{sx}}\right)^2\right) \\
F_{ax} &= -2c_{px}\sigma_x a^2 \left(1 - \frac{4}{3}\frac{c_{px}\sigma_x a^2}{F_z\mu_{sx}} + \frac{4}{9}\frac{c_{px}^2\sigma_x^2 a^4}{F_z^2\mu_{sx}^2}\right) \\
F_{ax} &= -2c_{px}\sigma_x a^2 + \frac{8}{3}\frac{c_{px}^2\sigma_x^2 a^4}{F_z\mu_{sx}} - \frac{8}{9}\frac{c_{px}^3\sigma_x^3 a^6}{F_z^2\mu_{sx}^2} \qquad (2.22)
\end{aligned}
$$

2.3.3   Sliding Zone Forces

In the sliding zone, after the transition points x_s, the friction force is created due to the sliding of the bristle along the surface. We treat this as classical sliding friction $F_s = \mu_k F_z$ where μ_k is the kinetic (dynamic) friction coefficient. In order to find the vertical force acting in the sliding zone, we must integrate the distribution of vertical force from the rear of the wheel $(-a)$ to the transition point x_s.
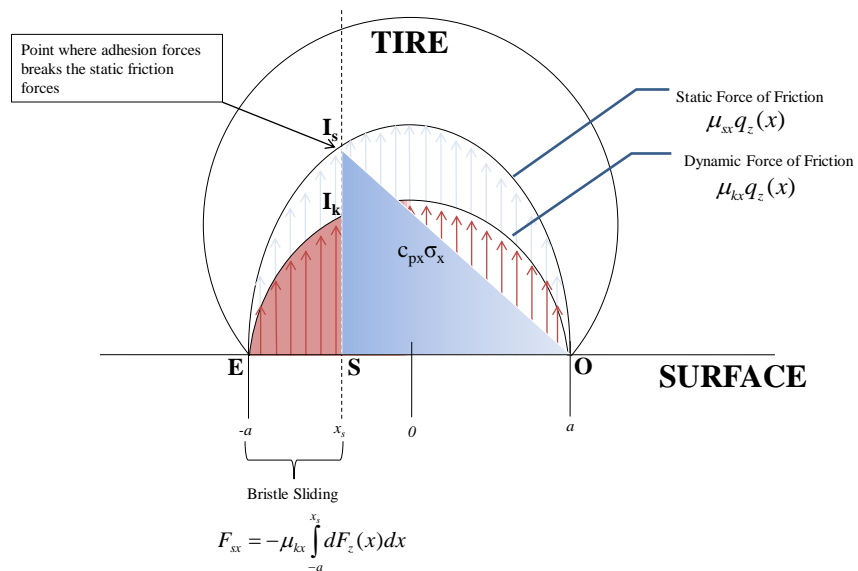
Figure 2.5: Schematic of the sliding zone in the Brush Model. The total sliding force is equal to the area under the curve of ESI_k.

$$
\begin{aligned}
F_{sx} &= -\mu_k \int_{-a}^{x_s} dF_z(x)dx \\
&= -\mu_k \int_{-a}^{x_s} \frac{3Fz}{4a}(1-(\frac{x}{a})^2) \\
&= -\frac{3Fz\mu_k}{4a^3} \int_{-a}^{x_s} a^2 - x^2 \\
&= -\frac{3Fz\mu_k}{4a^3} \left[a^2 x - \frac{x^3}{3} \right]_{x=-a}^{x=x_s} \\
&= -\frac{3Fz\mu_k}{4a^3} \left[a^2 x_s - \frac{x_s^3}{3} + a^3 - \frac{a^3}{3} \right] \\
&= -\frac{Fz\mu_k}{4a^3} \left[2a^3 - x_s^3 + 3a^2 x_s \right]
\end{aligned}
$$

Substituting $x_s = (2\sigma - 1)a$

$$
\begin{aligned}
F_{sx} &= -\frac{Fz\mu_k}{4a^3} \left[2a^3 - ((2\bar{\sigma}-1)a)^3 + 3a^2((2\bar{\sigma}-1)a) \right] \\
&= -\frac{Fz\mu_k}{4} \left[2 - (2\bar{\sigma}-1)^3 + 3(2\bar{\sigma}-1) \right] \\
&= -\frac{Fz\mu_k}{4} \left[2 - (8\bar{\sigma}^3 - 12\bar{\sigma}^2 + 6\bar{\sigma} - 1) + 6\bar{\sigma} - 3 \right] \\
&= -Fz\mu_k \left[-2\bar{\sigma}^3 + 3\bar{\sigma}^2 \right]
\end{aligned}
$$

And finally, re-substituting the value for $\bar{\sigma}$

$$
\begin{aligned}
F_{sx} &= -Fz\mu_k \left[-2\left(\frac{c_{px}\sigma_x 2a^2}{3F_z\mu_{sx}} \right)^3 + 3\left(\frac{c_{px}\sigma_x 2a^2}{3F_z\mu_{sx}} \right)^2 \right] \\
F_{sx} &= -Fz\mu_k \left[-\frac{16}{27} \frac{c_{px}^3\sigma_x^3 a^6}{F_z^3\mu_{sx}^3} + \frac{4}{3} \frac{c_{px}^2\sigma_x^2 a^4}{F_z^2\mu_{sx}^2} \right] \\
F_{sx} &= +\frac{16}{27} \frac{c_{px}^3\sigma_x^3 a^6 \mu_k}{F_z^2\mu_{sx}^3} - \frac{4}{3} \frac{c_{px}^2\sigma_x^2 a^4 \mu_k}{F_z\mu_{sx}^2} \qquad\qquad (2.23)
\end{aligned}
$$

2.3.4 Total Friction Force

Finally, the total friction developed between the tire and the surface is the addition of the friction due to adhesion F_{ax} and the friction due to sliding F_{sx}.

$$F_x = F_{ax} + F_{sx}$$

$$F_x = \left[-2c_{px}\sigma_x a^2 + \frac{8}{3}\frac{c_{px}^2 \sigma_x^2 a^4}{F_z \mu_{sx}} - \frac{8}{9}\frac{c_{px}^3 \sigma_x^3 a^6}{F_z^2 \mu_{sx}^2} \right] + \left[\frac{16}{27}\frac{c_{px}^3 \sigma_x^3 a^6 \mu_k}{F_z^2 \mu_{sx}^3} - \frac{4}{3}\frac{c_{px}^2 \sigma_x^2 a^4 \mu_k}{F_z \mu_{sx}^2} \right]$$

$$(2.24)$$

Alternate Forms of the Basic Brush Model

The form of the brush model equation in 2.24 can be re-arranged in several forms:

If we rearrange this in the form of a polynomial with σ as the independent variable we get

$$F_x = -2c_{px}a^2\sigma_x + \frac{c_{px}^2 a^4 \sigma_x^2}{F_z}\left(\frac{8}{3\mu_{sx}} - \frac{4\mu_{kx}}{3\mu_{sx}^2} \right) + \frac{c_{px}^3 a^6 \sigma_x^3}{F_z^2}\left(-\frac{8}{9\mu_{sx}^2} + \frac{16\mu_{kx}}{27\mu_{sx}^3} \right)$$

$$(2.25)$$

Simplifying further

$$F_x = -2c_{px}a^2\sigma_x + \frac{4}{3}\frac{c_{px}^2 a^4 \sigma_x^2}{F_z \mu_{sx}^2}(2\mu_{sx} - \mu_{kx}) + \frac{8}{27}\frac{c_{px}^3 a^6 \sigma_x^3}{F_z^2 \mu_{sx}^3}(-3\mu_{sx} + 2\mu_{kx})$$

$$(2.26)$$

Other works on the brush model have simplified the model further by $\mu_{sx} = \mu_{kx}$. However the science of Tribology (Chapter 6) has shown that the static and dynamic coefficients of friction are only *near* equal for very low sliding speeds. As the sliding speeds in tire-braking operations are normally greater than $1m/2$, we will not use the simplification $\mu_{sx} = \mu_{kx}$.

The next section will demonstrate the strong effect that a difference between μ_{sx} and μ_{kx} has on the form of the μ-slip curve. However we can rearrange equation (2.26) to obtain a ratio of μ_{kx}/μ_{sx}.

$$F_x = -2c_{px}a^2\sigma_x + \frac{4}{3}\frac{c_{px}^2 a^4 \sigma_x^2}{F_z \mu_{sx}}\left(2 - \frac{\mu_{kx}}{\mu_{sx}} \right) + \frac{8}{27}\frac{c_{px}^3 a^6 \sigma_x^3}{F_z^2 \mu_{sx}^2}\left(-3 + 2\frac{\mu_{kx}}{\mu_{sx}} \right) \quad (2.27)$$

The majority of curves in the aeronautical industry are presented as μ-slip curves. This mu, is in fact a normalized braking coefficient $\bar{F}_x = -Fx/Fz$ or alternatively presented as μ or μ_{global}. To obtain this conventional $\mu - slip$ curve from the basic brush model, we divide through by F_z.

$$\mu_{global} = -\frac{F_x}{F_z}\frac{|v_{s_x}|}{v_{s_x}}$$
$$= \frac{2c_{px}a^2\sigma_x}{F_z} - \frac{4}{3}\frac{c_{px}^2 a^4 \sigma_x^2}{F_z^2 \mu_{sx}}\left(2 - \frac{\mu_{kx}}{\mu_{sx}}\right) - \frac{8}{27}\frac{c_{px}^3 a^6 \sigma_x^3}{F_z^3 \mu_{sx}^2}\left(-3 + 2\frac{\mu_{kx}}{\mu_{sx}}\right)$$

$$(2.28)$$

Pure Slip

Recall that the brush model theory results in a repartition of the contact area into two zones, an adhesion zone and a sliding zone. The derivation of the brush model demonstrates that braking is not-possible without sliding. This can be visually seen in the schematic of the bristle movement (Figure 2.4). From the moment that the tire begins to brake (slip ratio $\sigma_x > 0$) the bristles at the rear of the tire will be sliding. As the slip ratio increases, the sliding zone will grow at the expense of the adhesion zone. The point where the entire contact zone is sliding we will call *pure-slip*. From section 2.3.2, the contact zone will be in pure slip when the transition zone x_s is equal to the start of the contact zone a (In figure 2.5 this can be visualized as when the transition point x_s is at the point O. Thus the triangle representing the adhesion force disappears and the entire contact zone has sliding friction). Substituting $x_s = a$ into (2.18) we find the *limit-slip* at which the contact zone is 100% sliding.

$$\sigma_x^o = \frac{3F_z\mu_{sx}}{2a^2 c_{px}} \tag{2.29}$$

If the tire-surface is in *pure-slip*, the μ_{global} should equal the dynamic/sliding friction coefficient, μ_k. Substituting equation (2.29) into the μ_{global} form of the brush model, equation (2.28) we find

$$\mu_{global} = -\mu_k$$

The point σ_x^o is important in the plotting of the μ-slip curve as it defines the *point of discontinuity* where the adhesion force becomes nil and the tire is in pure sliding. After this point the general form of the brush model is not applicable. Therefore to plot the brush model we define two curves.

If $\sigma_x \leq \sigma_x^o$ then

$$F_x = -2c_{px}a^2\sigma_x + \frac{4}{3}\frac{c_{px}^2 a^4 \sigma_x^2}{F_z \mu_{sx}}\left(2 - \frac{\mu_{kx}}{\mu_{sx}}\right) + \frac{8}{27}\frac{c_{px}^3 a^6 \sigma_x^3}{F_z^2 \mu_{sx}^2}\left(-3 + 2\frac{\mu_{kx}}{\mu_{sx}}\right)$$

Else if $\sigma_x > \sigma_x^o$ then

$$F_x = -\mu_{kx}\frac{v_g}{|v_g|}|F_z|$$

Where

$$\sigma_x^o = \frac{3F_z \mu_{sx}}{2a^2 c_{px}}$$

What is interesting to note is the physical significance of pure slip in the brush model. As mentioned before, the industrial notion of slip is measured in terms of s, where 0 is a free rolling wheel and 1 is a blocked wheel. We normally associated a wheel in 100% sliding as that of a blocked wheel ($\omega = 0$ and $s = 1$), that is to say with 0 circumferential velocity, v_c. However, the brush model demonstrates that 100% (pure-slip) sliding can occur before $s = 1$, that is, while the tire is still rolling. Intuitively this seems contradictory. Thus we re-visit the definitions of slip.

$$s_x = \frac{v_x - v_c}{v_x} = \frac{\sigma_x}{1 + \sigma_x}$$

$$\sigma_x = \frac{v_x - v_c}{v_c} = \frac{s_x}{1 - s_x}$$

Recall that the definition σ_x is used because in the brush model we are directly measuring the longitudinal deformation of the bristle (Figure 2.3).

$$\Delta_x(x) = x_r(x) - x = -\frac{v_x - v_c}{v_c}(a - x) = -\sigma_x(a - x)$$

What does it mean in the brush model for a surface to be in pure-slip? Essentially it means that the difference in speed between the tangential speed at the top of the bristle,v_c, and the tire forward movement speed, v_x, is large enough that at the moment a bristle enters the contact zone, the difference in position between the top of the bristle and the bottom is large enough that the bristle begins to slide. So although the tire is still rolling and thus the bristle is still traversing the contact zone, the bristle is sliding. This as opposed to the case of a blocked wheel, $s = 0$, where the bristles are 100% sliding, but the bristles are not traversing the sliding zone because $\omega = 0$,$v_c = 0$.

2.4 Conclusion Basic Brush Model Derivation

This concludes the derivation of what we will call the *Basic Brush Model*. That is to say, the Brush Model derived under simplified conditions such as:

parabolic distribution of pressure, constant μ_{sx} and μ_{kx} and linear tire-stiffness. Chapters 3, 4, 5 and 6 will further develop the Brush Model to consider the viscoelastic rubber material and its effect on the coefficient of friction and the tire behavior. The following section (2.5) will perform a sensibility analysis on the parameters in the Brush Model and identify the key points on the $\mu - slip$ cuve.

Brush Model

If $\sigma_x \leq \sigma_x^o$ then

$$F_x = -2c_{px}a^2\sigma_x + \frac{4}{3}\frac{c_{px}^2 a^4 \sigma_x^2}{F_z \mu_{sx}}\left(2 - \frac{\mu_{kx}}{\mu_{sx}}\right) + \frac{8}{27}\frac{c_{px}^3 a^6 \sigma_x^3}{F_z^2 \mu_{sx}^2}\left(-3 + 2\frac{\mu_{kx}}{\mu_{sx}}\right)$$
$$(2.30)$$

Else if $\sigma_x > \sigma_x^o$ then
$$F_x = -\mu_{kx}\frac{v_g}{|v_g|}|F_z|$$

Where
$$\sigma_x^o = \frac{3F_z \mu_{sx}}{2a^2 c_{px}}$$

Variables and Units :

$2a$	: Length of tire-surface contact zone		$[m]$
c_{px}	: Tire stiffness per unit length of contact zone length		$[N/m^2]$
σ_x	: Longitudinal slip ratio		$[-]$
F_z	: Total vertical force applied on the wheel		$[N]$
F_x	: Horizontal Force due to braking		$[N]$
μ_{kx}	: Dynamic coefficient of friction		$[-]$
μ_{sx}	: Dynamic coefficient of friction		$[-]$

2.5   Sensibility Analysis

2.5.1   Brush Model Form

The first step after deriving the brush model is to confirm that the mathematical derivation produces a model that is consistent with basic tire-runway theory based on the combination of experimental results in the automobile world. To facilitate the comparison, we examine the shape of the μ-slip i.e. $\mu_{global} = f(\sigma_x)$ which is the conventional curve used in tire-runway contact.

We can summarize that the brush model calculates the force of friction from 6 variables for pure longitudinal slip

$$F_x = f(c_{px}, a, \mu_{kx}, \mu_{sx}, F_z, \sigma)$$

We recall that F_x is the combined friction force opposing the movement of the tire, c_{px} is the tire stiffness coefficient per unit length in the longitudinal axis, a is one half the length of the tire-surface contact zone, μ_{kx} is the dynamic coefficient of friction at the tire-surface in longitudinal slip, μ_{sx} is the static coefficient of friction at the tire-surface in longitudinal slip and F_z is the vertical load on the tire.

First, a mathematical derivation of the brush model will reveal some key points and characteristics of the μ-slip curve which will be of benefit when trying to understand the physical effects of parameters.

Remark 1. *The form of slip s is more commonly used in industry and has a more physical sense in that it varies between* 0 *(free-rolling wheel) and* 1 *(blocked wheel). As such, the majority of the μ-slip figure below are plotted using the form of slip, s.*

Remark 2. *Recall that the brush model can be in terms of the horizontal friction force, F_x, or a μ_{global} where $\mu_{global} = -F_x/F_z$. Because the vertical load, F_z is constant as a function of slip, the shape of the μ-slip (or $F_x$slip) curve remains the same in both cases, simply the scaling of the ordinate changes. As such, the following plots may be in terms of F_x or μ_{global} depending on which gives a more simplistic derivation.*

Key Points on the μ-Slip Curve

Remark 3. *Although our coordinate system specifies that braking produces a negative F_x, the curves henceforth plot F_x in the positive y-axis for simplicity.*

Slope at Zero Slip

Taking the first derivative of (2.27) with respect to σ_x and setting $\sigma_x = 0$ will provide the initial slope of the μ-slip curve.
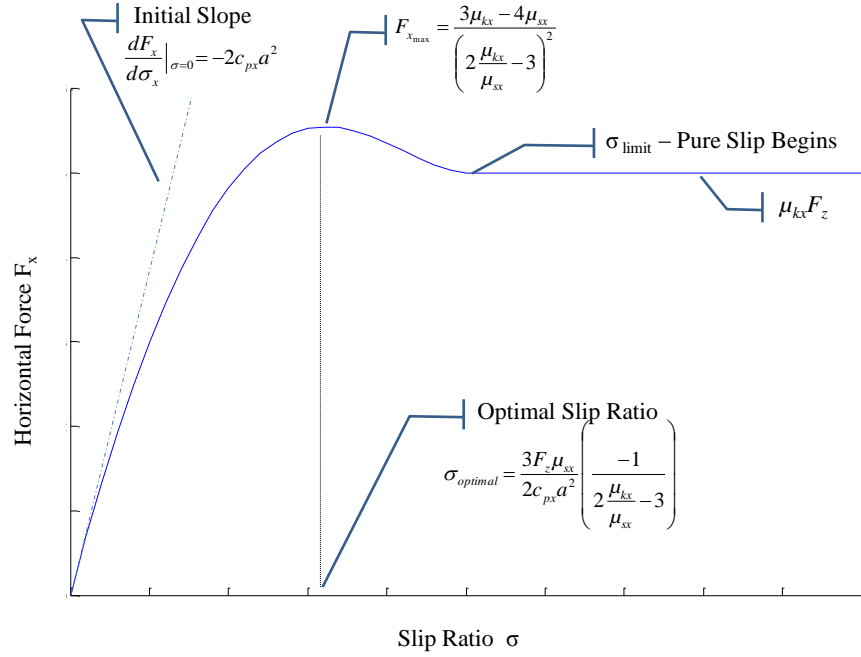
Figure 2.6: Basic form of the friction-slip curve with key points

$$\left.\frac{dF_x}{d\sigma_x}\right|_{\sigma_x=0} = -2c_{px}a^2 \qquad (2.31)$$

The above result establishes that the initial slope of the μ-slip curve is proportional to the tire-stiffness, c_{px}. This result is consistent in that at very small slips, we know that the majority of the contact zone is under adhesion forces which are governed by the stiffness of the tire.

Optimal Slip Ratio

This is the slip value which provides the maximum friction available for a given tire-surface. This value is important in anti-skid system control as the goal of the anti-skid system is to regulate the brake pressure (which in turn regulates the slip ratio) in order to achieve the maximum braking possible. Maximum braking depends directly on achieving the maximum μ possible. Using the *first-derivative rule*, we can mathematically determine the local maximum of the brush model equation. Differentiating the brush model equation (2.27) with respect to σ_x

$$\frac{dF_x}{d\sigma_x} = -2c_{px}a^2 + \frac{8}{3}\frac{c_{px}^2 a^4 \sigma_x}{F_z \mu_{sx}^2}\left(2\mu_{sx} - \mu_{kx}\right) + \frac{24}{27}\frac{c_{px}^3 a^6 \sigma_x^2}{F_z^2 \mu_{sx}^3}\left(-3\mu_{sx} + 2\mu_{kx}\right)$$

(2.32)

Since this is a polynomial of *2-degrees* in the form $A\sigma_x^2 + B\sigma_x + C$, we can use the quadratic formula to find the roots

$$\sigma_x = \frac{-B \pm \sqrt{B^2 - 4AC}}{2A}$$

(2.33)

where

$$A = \frac{24}{27}\frac{c_{px}^3 a^6 \sigma_x^2}{F_z^2 \mu_{sx}^3}\left(-3\mu_{sx} + 2\mu_{kx}\right)$$

$$B = \frac{8}{3}\frac{c_{px}^2 a^4 \sigma_x}{F_z \mu_{sx}^2}\left(2\mu_{sx} - \mu_{kx}\right)$$

$$C = -2c_{px}a^2$$

Combining variables and simplifying

$$\sigma_x = \frac{3F_z\mu_{sx}}{2c_{px}a^2}\left[\frac{-\left(2 - \frac{\mu_{kx}}{\mu_{sx}}\right) \pm \sqrt{\left(2 - \frac{\mu_{kx}}{\mu_{sx}}\right)^2 + \left(-3 + \frac{2\mu_{kx}}{\mu_{sx}}\right)}}{\left(-3 + \frac{2\mu_{kx}}{\mu_{sx}}\right)}\right]$$

(2.34)

And further simplifying

$$\sigma_x = \frac{3F_z\mu_{sx}}{2c_{px}a^2}\left[\frac{\left(-2 + \frac{\mu_{kx}}{\mu_{sx}}\right) \pm \frac{mu_{kx}}{\mu_{sx}} - 1}{\left(-3 + \frac{2\mu_{kx}}{\mu_{sx}}\right)}\right]$$

(2.35)

Finally this gives two roots of σ_x

$$\sigma_{x_1} = \frac{3F_z\mu_{sx}}{2c_{px}a^2}\left[\frac{-1}{2\frac{\mu_{kx}}{\mu_{sx}} - 3}\right]$$

$$\sigma_{x_2} = \frac{3F_z\mu_{sx}}{2c_{px}a^2}$$

Since F_x is a third order function with respect to σ_x we expect two points of zero slope, a maximum and a minimum. The maximum will correspond to the maximum friction and the optimal slip ratio. While the minimum refers to the point where the adhesive forces become nil and the tire-surface contact zone is in pure sliding. In this case, σ_{x_1} refers to the local maximum while σ_{x_2} refers local minimum. Thus it is not surprising to find that σ_{x_2} is

equal to the σ_x^o that we calculated in equation (2.29) since both refer to the point where the tire-surface is in pure sliding. The *optimal slip ratio*, $\sigma_{x_{opt}}$ is then

$$OSR = \sigma_{x_1} = \frac{3F_z\mu_{sx}}{2c_{px}a^2}\left[\frac{-1}{2\frac{\mu_{kx}}{\mu_{sx}} - 3}\right] \tag{2.36}$$

Maximum Friction

Subbing the $\sigma_{x_{opt}}$ into the general equation for μ_{global} (2.28) we obtain the μ_{max}

$$\mu_{max} = -\frac{3\mu_{sx}}{2\frac{\mu_{kx}}{\mu_{sx}} - 3} - \frac{3\mu_{sx}\left(2 - \frac{\mu_{kx}}{\mu_{sx}}\right)}{(2\frac{\mu_{kx}}{\mu_{sx}} - 3)^2} + \frac{\mu_{sx}}{(2\frac{\mu_{kx}}{\mu_{sx}} - 3)^2} \tag{2.37}$$

Simplifying

$$\boxed{\mu_{max} = -\frac{3\mu_{kx} - 4\mu_{sx}}{(2\frac{\mu_{kx}}{\mu_{sx}} - 3)^2}} \tag{2.38}$$

From this derivation we can determine some important characteristics about the form of the μ-slip curve. The first is that if $\mu_{kx} = \mu_{sx}$ then $\sigma_{x_1} = \sigma_{x_2} = \sigma_x^o$. That is to say that the optimal slip ratio and consequently the maximum friction force occurs when the tire contact zone is in pure sliding. $\mu_{kx} = \mu_{sx}$ results in a μ-slip curve without a true peak, simply an asymptotic curve at μ_{max}.

The second and most interesting development is that the brush model equations determine that the maximum available friction does not depend on the tire characteristics. The vertical force, the contact length, the slip ratio and tire-stiffness variables all disappear. **As such the maximum available friction is a function only of the static and dynamic coefficients of friction.**

2.5.2 Physical Effect of Variables

The reason to using the brush model is to introduce a friction model that takes into account the characteristics of the environment to produce a physical model. This produces a more robust, flexible friction model in that if a parameter is changed such as tire size, tire pressure, tire type, runway texture etc... the new braking performance could be modeled and thus predicted.

In this section we examine the principal variables involved in the brush model. We vary each parameter and note its effect on the μ-slip curve. We then try to explain mathematically and physically the effect of each variable.
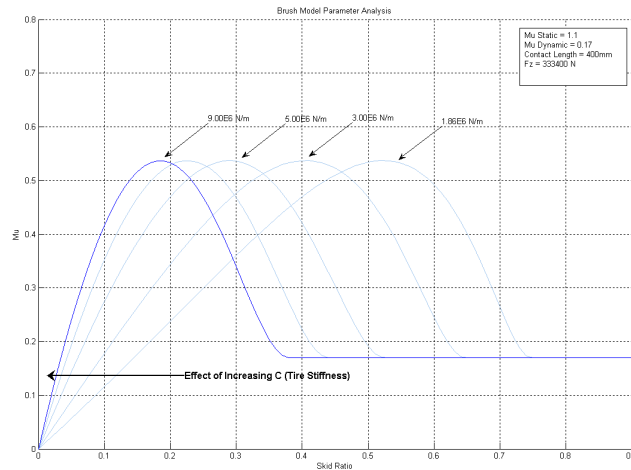
Tire-Stiffness Effect

Figure 2.7: Brush Model Effect of Tire Stiffness

Observation	Figure 2.7 shows that as the tire-stiffness increases, the initial slope of the mu-slip curve increases. Although the μ_{max} remains constant, the optimal slip ratio s_{opt} decreases.
Mathematical Proof	From section 2.5.1, we note that the initial slope of the mu-slip curve is proportional to $2c_{px}a^2$. Also equation (2.38) states that the μ_{max} does not depend on the tire-stiffness.
Physical Sense	A stiffer tire (larger c_{px}) implies that a greater force per unit deflection will be required to deform the rubber. As such, the transition point between adhesion and sliding will happen at a lower slip ratio due to the fact that a smaller deformation of the the rubber will be needed to overcome the static coefficient of friction. Thus we expect that as the stiffness of the tire increases, the optimal slip ratio will decrease.

Static Friction Coefficient Effect
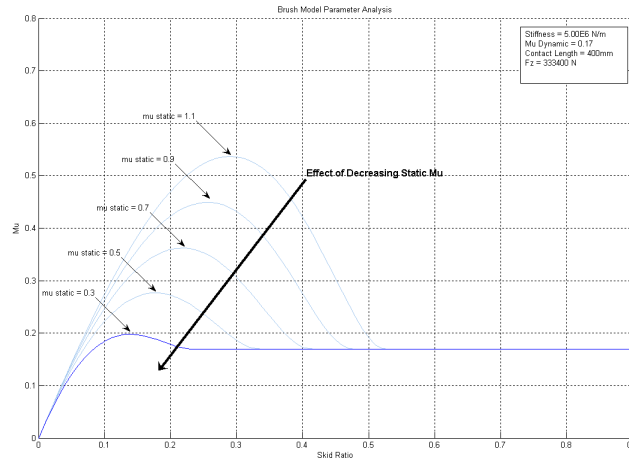
Figure 2.8: Brush Model Effect of Tire Static Mu

Observation	As the μ_{sx} decreases, the optimal slip ratio decreases and the maximum μ_{global} decreases as well.
Mathematical Proof	Referring to equations (2.36) and (2.38) we can see that the OSR and the μ_{max} are proportional to the μ_{sx}.
Physical Sense	Referring to figure 2.9, we note that increasing the μ_{sx} serves two purposes. For a given tire-stiffness, we are increasing the amount of deflection needed to break the static coefficient of friction. That is to say, a greater slip ratio is needed. In addition, we can see by figure 2.8 that increasing the μ_{sx} and thus the σ means a larger area under the curve. This implies that each bristle is allowed to deform more before slipping, thus contributing to a higher force of adhesion.

Figure 2.9: Tire Contact zone view of the effect of lowering the static coefficient of friction

Dynamic Friction Coefficient Effect
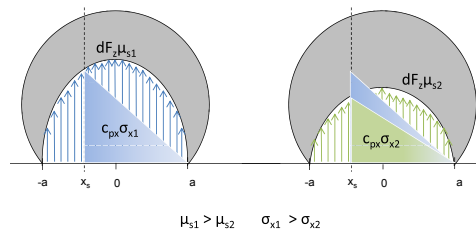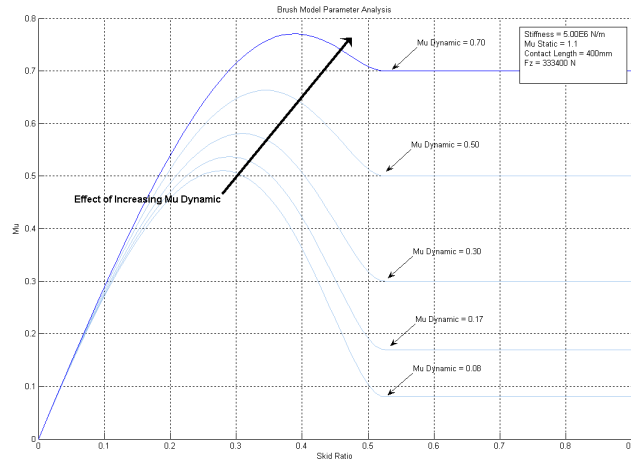

Figure 2.10: Brush Model Effect of Tire Dynamic Mu

Observation	We note that as the dynamic coefficient of friction decreases, the optimal slip ratio and the μ_{max} decrease.
Mathematical Proof	Referring to equations (2.36) and (2.38) we can see that the OSR and the μ_{max} are proportional to the μ_{kx}. It can also be noted in the diagram that the position of the limit-slip, σ_x^o is unchanged. This corresponds with equation (2.29) which has no μ_{kx} variable involved.
Physical Sense	The dynamic coefficient of friction is the variable which governs sliding in the contact zone. If the μ_{kx} is small in comparison with the μ_{sx}, it means that the forces due to sliding friction are insignificant compared to the forces due to adhesion. Thus in order to achieve the μ_{max} the majority of the contact zone should be under adhesive forces. To achieve this, the slip-ratio will be smaller in order to have a transition point x_s closer to the rear of the tire.
	In the reverse sense, if μ_{kx} is approaching the same value as μ_{sx} then the sliding zone is producing more friction than the adhesion zone. Thus as noted by equation (2.36), when $\mu_{kx} = \mu_{sx}$ the optimal slip ratio is found at the $limit - slip$ when the entire contact zone is in pure slip.

2.6 Introduction to Advanced Brush Model

The basic form of the brush model forms the foundation of the tire-surface modeling. The brush model is presented as computing the total force of friction as a function of 6 variables.

$$F_x = f(c_{px}, a, \mu_{kx}, \mu_{sx}, F_z, \sigma_x)$$

where F_x is the combined friction force opposing the movement of the tire, c_{px} is the tire stiffness coefficient per unit length in the longitudinal axis, a is one half the length if the tire-surface contact zone, μ_{kx} is the dynamic coefficient of friction at the tire-surface in longitudinal slip, μ_{sx} is the static coefficient of friction at the tire-surface in longitudinal slip and F_z is the vertical load on the tire.

In order to have a complete equation we need the values for each of these 6 variables. The variables F_z and σ_x are given parameters. The contact length, a, is modeled as a function of the vertical load with experimental data providing the formula. This leaves three variables that need to be defined to complete the Brush Model: c_{px}, μ_{sx} and μ_{kx}. These three variables we call *unknown* and must either be **estimated** or **identified** from experimental data.

In order to **estimate** the *unknown* variables, we must be able to model the parameters. This can be done using scientific pricipals and experimental data to develop analytical models. Chapters 3, 4, 5 and 6 will determine qualitatively and quantitatively the factors that affect the tire-stiffness, c_{px}, and the static and dynamic coefficients of friction, μ_{sx} and μ_{kx}. To **identify** the *unknown* variables we will use experimental data and curve fitting techniques to fit the Brush Model to the experimental data.

For the parameter **estimation**, we use three branches of science to model these variables. The tire-stiffness, C_x is a mechanical characteristic of the tire. It depends on the *Strength of Materials*, which determine the deformation of the tire, as well as *Material Science*, which determines the variation of the tire materials shear modulus.

The *Science of Tribology* will form the base for the development of the static and dynamic coefficients of friction. Tribology will be used to determine the complex interactions that are present between rubber and rough surface sliding friction.

The Chapter on Material Science will characterize the behavior of the rubber used in tires. It will be shown that the rubber characteristics vary as a function of temperature and solicitation frequency. The rubber's mechanical strength will affect both the friction characteristics of the rubber as well as the stiffness of the tire.

Figure 2.11 represents schematically the scientific approach we have used to further develop the Brush Model.
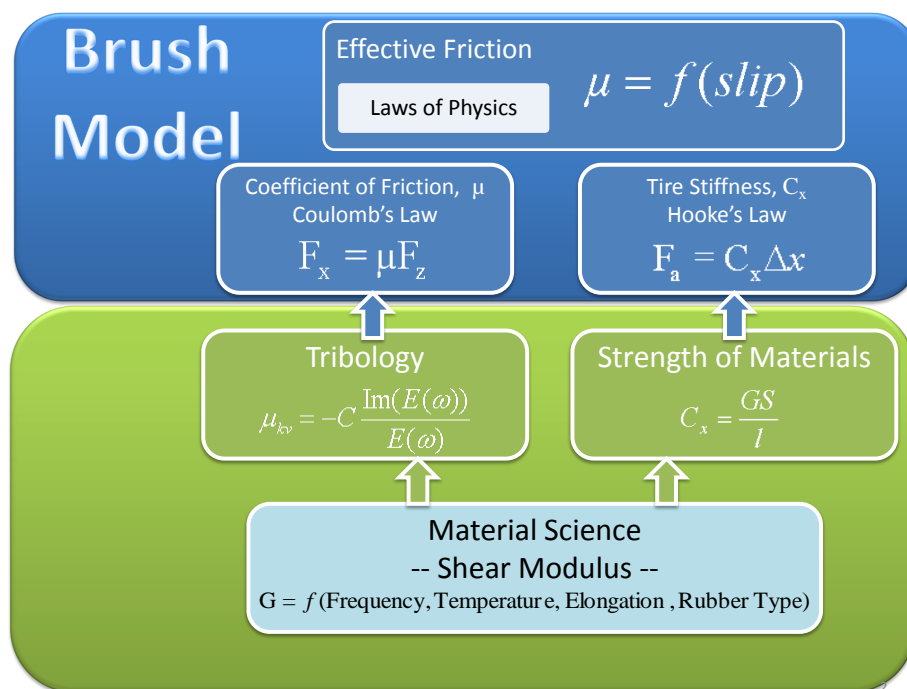
Figure 2.11

Chapter 3

Material Science

Summary. Ce chapitre est consacré à la compréhension des caractéristiques mécaniques du caoutchouc utilisé pour les pneus des avions. Le caoutchouc est un matériau viscoélastique, ce qui a d'importantes conséquences sur ses propriétés mécaniques. Un matériau viscoélastique est un matériau pour lequel la relation entre la contrainte et la déformation est fonction du temps. Nous pouvons définir plusieurs propriétés de base d'un matériau viscoélastique :

- Si la contrainte est maintenue constante, la déformation augmente avec le temps (fluage)
- Si la déformation est maintenue constante, la contrainte diminue avec le temps (relaxation)
- La rigidité effective dépend du taux d'application de la charge
- L'application d'une charge cyclique conduit à une hystérésis (décalage de phase) qui entraîne une dissipation de l'énergie mécanique
- Les ondes acoustiques subissent une atténuation
- Le rebond d'un objet suite à un impact est inférieur à 100%
- Lors du roulage, il se produit une résistance de frottement

Les propriétés viscoélastiques du caoutchouc sont importantes pour le freinage des avions, en raison de la charge cyclique qui s'exerce sur le pneu pendant que le caoutchouc glisse le long de la surface rugueuse de la piste. En raison des propriétés viscoélastiques du caoutchouc, le décalage de phase entre la contrainte et la déformation crée une dissipation d'énergie appelée hystérésis. Le chapitre 6 démontre que cet effet d'hystérésis est la première source du frottement pneu-piste. Nous pouvons définir, pour un matériau viscoélastique, la contrainte (σ) et la déformation (ϵ) d'une sollicitation harmonique sous la forme : [10]

$$\epsilon = \epsilon_0 \sin(t\omega)$$

$$\sigma = \sigma_0 \sin(t\omega + \phi)$$

où ω est la fréquence de la sollicitation, t le temps et ϕ le décalage de phase entre la contrainte et la déformation. Sachant que le module de Young est le

rapport de la contrainte sur la déformation, nous pouvons définir un module de conservation (E') et un module de perte (E'')

$$E' = \Re(E) = \frac{\sigma_0}{\varepsilon_0} \cos \phi$$

$$E'' = \Im(E) = \frac{\sigma_0}{\varepsilon_0} \sin \phi$$

Un module de conservation et un module de perte en cisaillement (G' et G'') peuvent être définis de la même manière, sachant que le module de cisaillement est le rapport de la contrainte de cisaillement sur la déformation de cisaillement. Le module de conservation et le module de perte peuvent également être représentés comme des variables complexes :

$$E = E' + iE''$$

$$G = G' + iG''$$

Afin de mieux comprendre la composition du pneu, nous avons travaillé avec le Laboratoire de Recherches et de Contrôle du Caoutchouc et des Plastiques (LRCCP) situé en France, près de Paris, et qui est spécialisé dans l'analyse des caoutchoucs et des polymères. Nous avons envoyé deux types de pneus au LRCCP qui en a analysé la structure et les caractéristiques mécaniques. Nous avons utilisé les données du LRCCP et l'équation de Williams-Landel-Ferry (WLF) pour extrapoler les caractéristiques mécaniques dans la plage de fréquence et de température. C'est-à-dire que nous avons utilisé la loi WLF pour déterminer les caractéristiques mécaniques pour toutes les combinaisons de fréquences de sollicitation et de températures du caoutchouc. Grâce à ce travail, nous avons pu calculer les caractéristiques mécaniques de l'ensemble pneu-caoutchouc pour les conditions rencontrées lors du freinage de l'avion.

Goal   *The goal of this chapter is to determine the mechanical characteristics (the Young's modulus, E, and the Shear Modulus, G) of the tire rubber. These characteristics will have an influence on the Tribology which will be developed in Chapter 6 and the Strength of Materials developed in Chapter 5. As a consequence, this Chapter will have an direct impact on the evaluation of c_{px}, μ_{sx} and μ_{kx} which are used in the derived form of the Brush Model (Pg 50) as developed in Chapter 2.*

3.1   Introduction

In order to understand the mechanical characteristics that will affect the tire stiffness and the friction, we must first understand the material. The
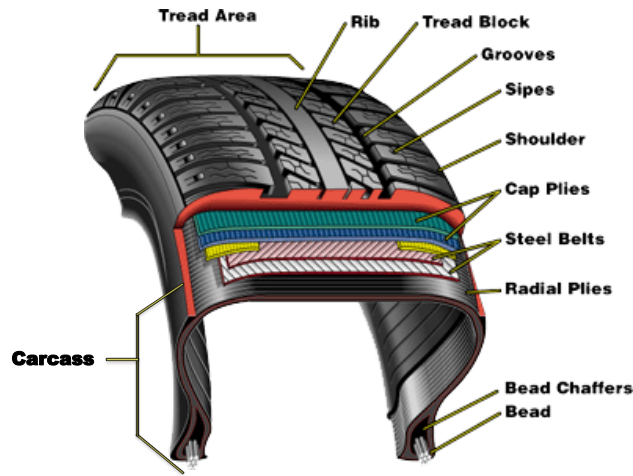
Figure 3.1: Typical composition of typical radial type tire used in the automobile sector

tire is a complex structure made up of several elements as shown in Figure (5.6). For simplicity, we will model the tire as a two structure element made up of the tire carcass and the tire tread. This simplification will become more evident in Chapter 5 as we characterize the tire stiffness.

The tire tread, the part of the tire in direct contact with the ground, is made of rubber. The formulation of tire rubber is a complicated chemical process known as vulcanization. The exact additives used in this process are usually closely guarded trade secrets. However, our experience has shown that although various tires from separate manufacturers may exhibit different overall mechanical characteristics, the mechanical characteristics of the rubber itself is often very similar. Thus the following discussion on the viscoelastic properties of rubber pertains to aircraft tires in general and not simply one manufacturer.

3.2 Material Properties of Rubber

3.2.1 Viscoelastic Properties of Rubber

Rubber is known as a viscoelastic material. In order to better understand the mechanical characteristics of rubber, one must first understand the nature of a viscoelastic material. In short, a viscoelastic material is a material for which the relationship between stress and strain depends on time. From [8] we can define seven basic properties of a viscoelastic material:

   – if the stress is held constant, the strain increases with time (creep)

   – if the strain is held constant, the stress decreases with time (relaxation)

   – the effective stiffness depends on the rate of application of the load

– if cyclic loading is applied, hysteresis (a phase lag) occurs, leading to a dissipation of mechanical energy

– acoustic waves experience attenuation

– rebound of an object following an impact is less than 100%

– during rolling, frictional resistance occurs

Another way to visualize a viscoelastic material is to think of the two extremes: a (near) purely elastic material and a (near) purely viscous material. If we take a near-purely elastic material such as a rubber band and apply a tensile force (stress), the rubber band stretches (strain) instantaneously, and when the force is released the rubber band will return to its original position instantaneously. That is to say that there is little-to-no phase lag between the stress and the strain. To the other extreme, we think of an extremely viscous material like a jar of honey. If we apply a shearing force to the top layer of the honey and then we suddenly remove this shearing force, the honey will continue to displace (strain) for a period of time. Thus there is a phase lag between the the stress and the strain. These two examples are of course simplistic in nature, but they give a very simple understanding of the lag that can occur between stress and strain.
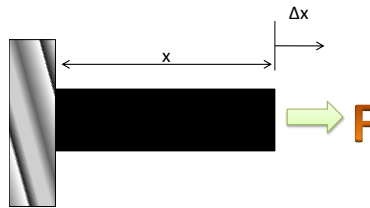

Figure 3.2: Applying a force to a rubber block and measuring the displacement Δ_x

In rubber, the viscoelastic effect can be clearly seen by a phase lag between the stress and the strain. Figure 3.3 shows how the phase lag between stress and strain can be calculated by cyclically loading the test specimen. This phase lag creates a dissipation of energy known as hysteresis and, as Chapter 6 will demonstrate, for aircraft tires this hysteresis effect is the primary source of tire-runway friction.

Hysteresis

In rubber, the hysteresis effect can be observed as the dissipation of mechanical energy when a specimen is loaded and unloaded. In a simple tensile loading and unloading, the hysteresis effect can be observed as a difference between the loading and unloading curves as shown in Figure 3.4. That is to say, that the energy taken to load the specimen is greater than the energy recovered when unloading the material. This dissipation of energy is due to the molecular structure of rubber or other polymers. Polymers
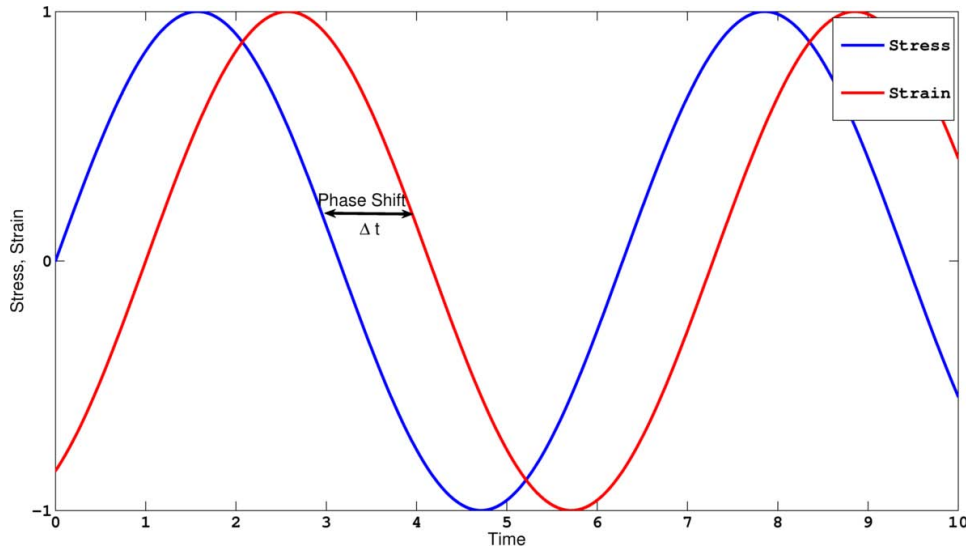
Figure 3.3: Cyclic loading of a viscoelastic material demonstrates the lag between stress and strain

are composed of polymer chains. These polymer chains intertwine together to form the structure of the polymer – this polymer chain intertwining is often visualized as a tangled bowl of spaghetti. When a polymer is put into uni-axial tension these polymers begin to *untangle* and orient themselves in the direction of the applied force. This *untangling* process requires energy to alter the intermolecular bonds. As a result of this interaction of polymer chains, we note that in general, the longer the chain length of the polymer the higher strength a polymer has [22]. This is due to the fact that a longer polymer chain will have more intertwining with adjacent polymer chains, thus necessitating greater stress in order to alter the intermolecular bonds.

3.2.2 Viscoelastic Effects

Viscoelastic properties exhibit different characteristics under dynamic (vibratory) conditions. The ratio of stress-strain under dynamic conditions is known as the dynamic modulus, $E(\omega)$. For a perfectly elastic material, when a stress is applied and removed the strain occurs instantaneously. That is to say, the stress and strain are in phase. For a viscous material there is a $90°$ phase lag between the stress and the strain. For a viscoelastic material, the phase lag is somewhere between 0 and $90°$.

For a viscoelastic material we can define the stress (σ) and strain (ϵ) in harmonic solicitation as [10]

$$\epsilon = \epsilon_0 \sin(t\omega)$$

$$\sigma = \sigma_0 \sin(t\omega + \phi)$$

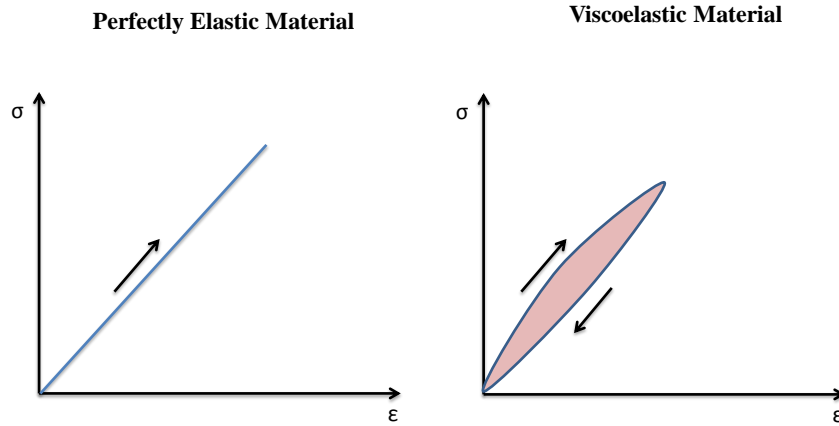**Perfectly Elastic Material**   **Viscoelastic Material**

Figure 3.4: The difference in the stress-strain relationship between elastic and viscoelastic materials. The area inside the loop of the viscoelastic stress-strain curves is the energy lost (hysteresis)

where ω is the solicitation frequency, t is time and ϕ is the phase lag between stress and strain. Knowing that Young's Modulus is the ratio of stress over strain we can define a storage modulus (E') and a loss modulus (E'')

$$E' = \Re(E) = \frac{\sigma_0}{\varepsilon_0} \cos \phi$$

$$E'' = \Im(E) = \frac{\sigma_0}{\varepsilon_0} \sin \phi$$

The storage and loss moduli in shear $(G'$ and $G'')$ can be defined in the same way knowing that the shear modulus is the ratio of shear stress over shear strain. The storage and loss moduli can also be represented as complex variables

$$E = E' + iE''$$

$$G = G' + iG''$$

For materials that experience small phase angles (such as the rubber used in an aircraft tire), we simplify and state that the storage modulus, E' (real part of E), is approximately the static Young's Modulus i.e $E' \approx E$, while the loss modulus, E'' (imaginary part of E), represents the dissipation of energy due to the viscoelastic characteristics of the material i.e. $E'' \approx E\phi$. *The viscoelastic effect and its effect on the friction will be explore in Chapter 6, but in general we can show that $\mu = -CE''/E = -C\phi$ i.e. we can demonstrate that the friction due to the viscoelastic nature of the rubber is proportional to the phase lag of the rubber.*

3.2.3 Effects of Horizontal Displacement - Non Linear Effect

Another well noted characteristic of polymers is that the strength modulus diminishes with increasing stress. This reduction is due to the polymer chains that are cross-linked. As a force is applied to a polymer, these long chains will begin to align themselves in the direction of the force i.e. the chains will begin to untangle. The energy is spent in untangling these chains i.e. altering the intermolecular bonds, but as the chains begin to align, the force needed to additionally stretch the chains diminishes. Although in Chapter 5 we see this emerge in the diminishing of tire-stiffness with horizontal displacement, the effect only becomes predominant for large horizontal deflections that do not occur in normal operations. As a result we will not take into account the effect of horizontal displacement on the rubber mechanical properties. *Note: Large deflections are not frequent in longitudinal displacement of the tire, however in the lateral sense significant deflections can occur.*

3.2.4 Effects of Temperature

Polymers such as rubber have a characteristic temperature known as the glass-transition temperature, T_g. At or around this temperature, the mechanical characteristics of the material, notably the Young's Modulus, E, and shear modulus, G, change considerably. In general, below T_g the material has glass like properties in that its stiffness E increases by several orders of magnitude and the material becomes very brittle. For example, striking a rubber block below its glass transition temperature will cause it to shatter as though it were glass. For rubber the glass transition temperature is approximately $-70°C$ although it can vary based on the use of additives in the rubber.

We will come to see in the next section that the mechanical characteristics are also a function of the solicitation frequency $E(\omega, T)$ where ω is the solicitation frequency and T is the temperature. The relationship between frequency and temperature is such that increasing the solicitation frequency is akin to increasing the glass transition temperature of the rubber. For example, rubber solicited at a frequency of $10^8 - 10^9$Hz will be in the glass state at room temperature (300K).

The *Williams-Landel-Ferry* law provides a mathematical relation with which to relate frequency and temperature

$$log(a_T) = \frac{-C_1(T - T_s)}{[C_2 + (T - T_s)]} \tag{3.1}$$

C_1 and C_2 are constants, T is the actual temperature and T_s is a reference temperature. For rubber T_s is normally taken as $T_s = T_g + 50$ and C_1 and C_2 determined experimentally ([5])

$$log(a_T) = \frac{-8.86(T - T_g - 50)}{101.5 + T - T_g - 50} \qquad (3.2)$$

We can equate the Young's modulus, E as a function of frequency and temperature using the Williams-Landel-Ferry equation

$$E(\omega, T) \approx E(\omega a_T) \qquad (3.3)$$

So whereas the rubber was in the glassy state at $T = 300$K and $\omega \approx 10^8 - 10^9$Hz, if the temperature is raised to $T = 400$K, then the frequency at which the rubber becomes glassy increases by an order of magnitude $\omega \approx 10^9 - 10^{10}$Hz.

3.2.5 Effects of Solicitation Frequency

When rubber is sliding on a rough surface, the rubber continually slides across and comes in contact with the peaks of the asperities as shown simply in Figure 3.5. These peaks generate a solicitation frequency in the rubber ω where

$$\omega = v_s/\lambda \qquad (3.4)$$

v_s is the sliding velocity and λ is the wavelength of the asperity. Section 3.2.4 referred to the strong effect of the glass transition temperature. As the temperature decreases towards the glass-transition temperature, the rubber becomes stiffer (Young's Modulus, E, increases). Below the glass transition temperature, the rubber stiffness increases by several orders of magnitude.
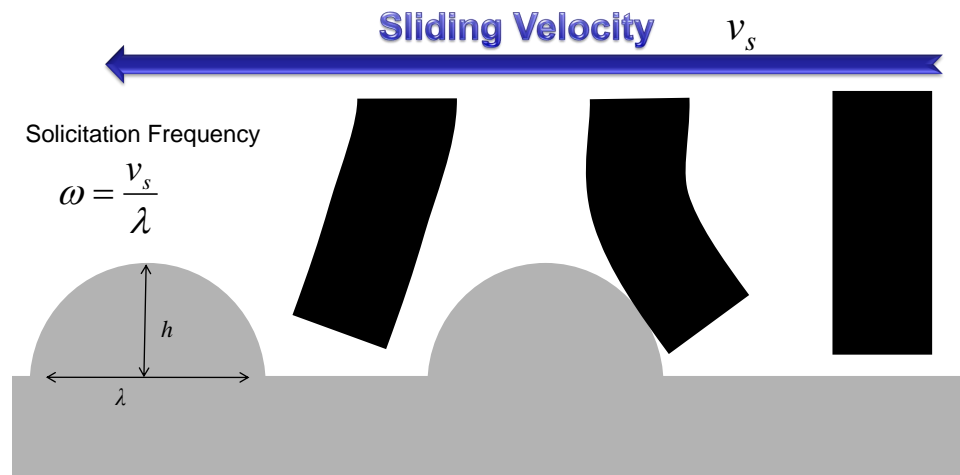

Figure 3.5: Mechanical characteristics are a function of the solicitation frequency defined by the sliding speed and the asperity length.

As the solicitation frequency increases, the hysteresis effect increases (as shown in Figure 3.14 which plots the phase lag, ϕ as a function of the solicitation frequency). This has the analogous effect as increasing the glass transition temperature of the rubber. Thus for a constant temperature (neglecting any frictional heating), as the sliding velocity increases the rubber will become stiffer (E increases). Section 3.2.4 demonstrated that rubber will transition to the glassy state at room temperature if the solicitation frequency is $\omega \approx 10^8 - 10^9 Hz$. This effect is significant in tire braking applications where the rubber can be solicited at frequencies of 10^6. Although this frequency is not in the glass transition region, the dynamic modulus is significantly larger at these frequencies than at low frequencies. As a tire brakes, the brush model demonstrates that the rear part of the tire is in pure sliding. We know that a runway surface is not flat. In fact at the microscopic level, a runway (or roadway) presents a structure similar to mountainous terrain i.e. a collection of peaks and valleys. From [14] we can define a runway (or roadway) surface as a fractal surface, or "self-affine" surface. A self-affine surface has the property that if we change the scale, the surface morphology does not change. Thus we can represent a runway as a set of asperities with a known width to height ratio and within these asperities will be a smaller set of asperities with approximately the same width to height ratio (Figure 3.6). This concept of runway surface texture is expanded further in Section 6. What is important to note is that this runway texture will generate a range of solicitation frequencies in the rubber which can be predicted based on knowledge of the runway texture.

EXAMPLE An aircraft comes in for landing at approximately $139 knots$ or $71.5 m/s$. The regulation of the anti-skid system may generate slip ratios up to 14% resulting in a sliding speed at the tire-runway interface of approximately $10 m/s$. The runway is modeled as a fractal surface which can be shown under different magnifications in Figure 3.6. For the largest aspertiy sizes of $1 mm$, the local rubber is being solicted at $10,000 Hz$. At a magnification of 10 the rubber in that region is being solicited at $100,000 Hz$ and at a magnification of 100, the local rubber is being solicted at $1,000,000 Hz$. For a constant temperature, if the soliciation frequency changes from 10^4 to 10^6 this causes approximately a 6 times increase in the loss modulus, G''. Consequently, there is a significant effect on the disspiation of energy (hysteresis) due to the viscoelastic characterteristics of the rubber.
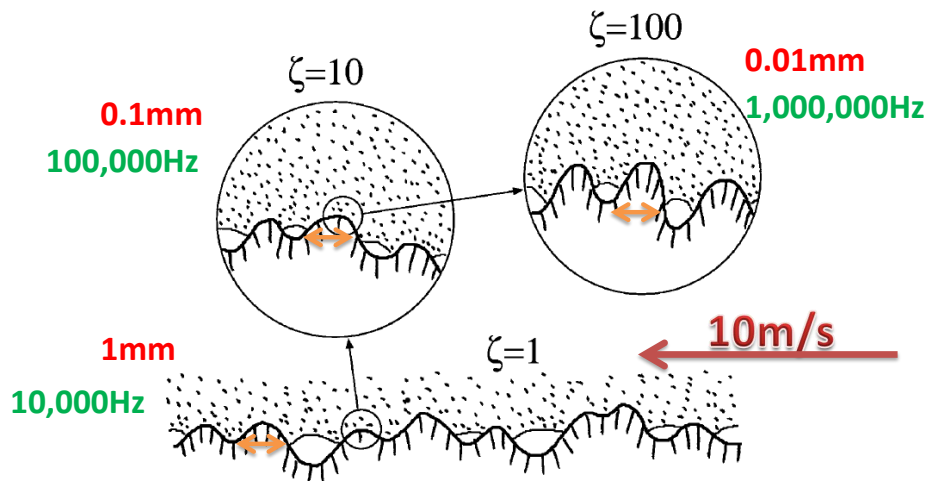
Figure 3.6: Example of rubber sliding on a runway represented by a fractal surface. At each magnification level, the solicitation frequency is higher.

3.3 Aircraft Tire Composition

One type of aircraft may have several different tire types available to be installed on the aircraft. For the purpose of this study we will look at two tires coming from two different manufacturers – Tire A and Tire B . These two tires have nearly the same external dimensions in order to properly fit on the aircraft, however due to their different manufacturers the tire characteristics may be different. Tire A will be used as the reference tire in which the majority of the tests will be performed. Tire B will be used to make comparisons to Tire A in order to determine the effect different construction techniques may have on tire properties.

We have enlisted the help of the *Laboratoire de Recherches et de Controle du Caoutchouc et des Plastiques* (LRCCP) which is a research laboratory specializing in the analysis of rubber and plastics near Paris, France. LRCCP was given both Tire A and Tire B and the structure of the tire and the mechanical characteristics were analyzed. The following is a small summary of the work done by LRCCP and the subsequent analysis of the results as it relates to the viscoelastic properties of rubber.

3.3.1 Tire Tread Rubber Analysis

The rubber from the tire-tread of both Tire A and Tire B were analyzed. The results showed that the rubber used within the tire tread from each manufacturer performs similarly, that is to say they have roughly the same mechanical properties. Consequently, the following analysis is applicable independent of the tire manufacturer.
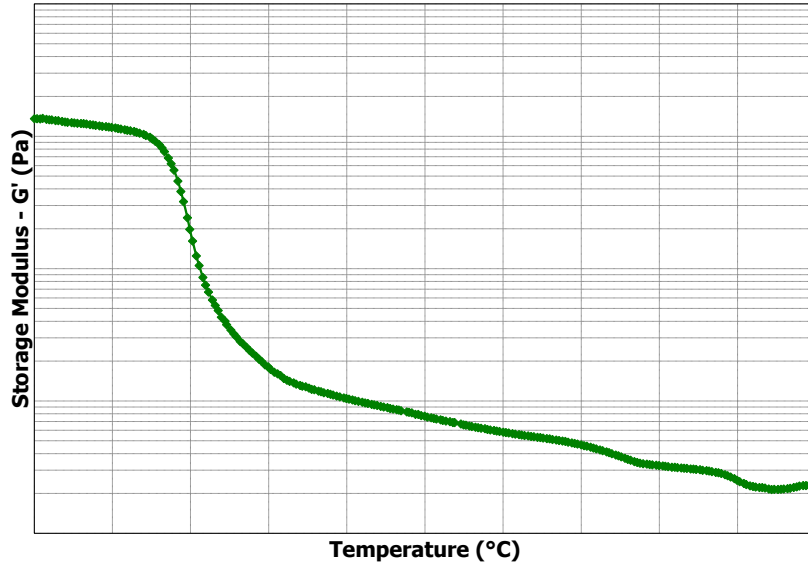
Figure 3.7: Storage Shear Modulus -G'(Pa)- as a function of temperature for a rubber specimen solicited at a given frequency

As reviewed in Section 3.2 the primary effect that will affect the rubber properties is the temperature frequency effect. To investigate this effect a mechanical analysis is performed using *Dynamic Mechanical Test* (DMA). This test consists of applying a shear load to the test specimen at a given frequency and a given dynamic strain while varying the temperature of the specimen. This test can be repeated for several frequencies to obtain an array of points as a function of frequency and temperature. From this test the following data is determined

 – δ - Phase Lag between stress and strain
 – G' - Storage shear modulus
 – G'' - Loss shear modulus

Figures 3.7, 3.8 and 3.9 show the initial results from the DMA tester for a rubber specimen at a given sampling frequency.

A subset of this data, the $tan(\delta)$, can be plotted in the frequency domain as shown in Figure 3.10. We note that the testing was performed for temperatures from $-60°C$ to $80°C$ and for a frequencies from $2Hz$ up to $200Hz$. We wish to use this data to determine the mechanical characteristics of the rubber when it is solicited at high frequencies. As we have shown in Figure 3.6, within the tire-runway contact area the rubber can be solicited in the megahertz range due to the micro asperities.

To extrapolate the measured data we use the *Williams-Landel-Ferry*

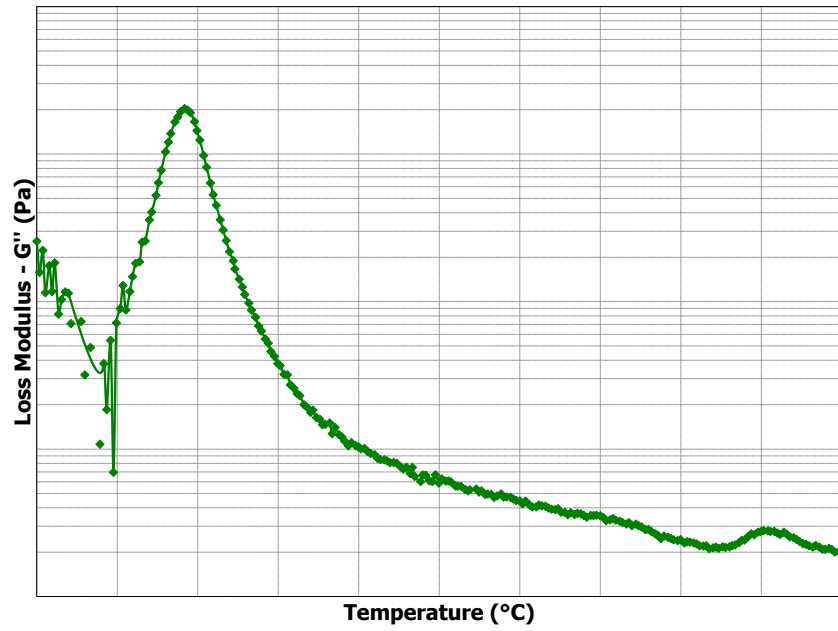Figure 3.8: Loss Shear Modulus - $G''(\text{Pa})$- as a function of temperature for a rubber specimen solicited at a given frequency
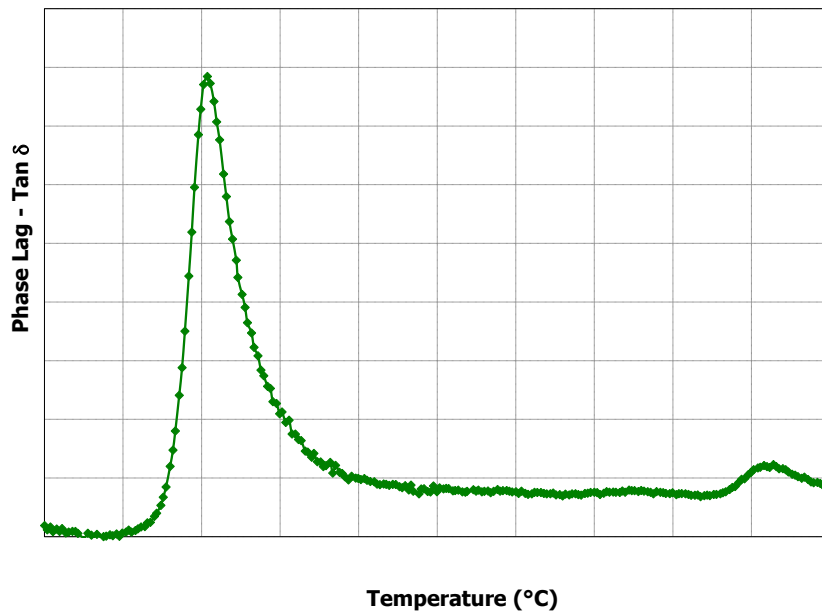

Figure 3.9: Phase Lag -δ - as a function of temperature for a rubber specimen solicited at a given frequency
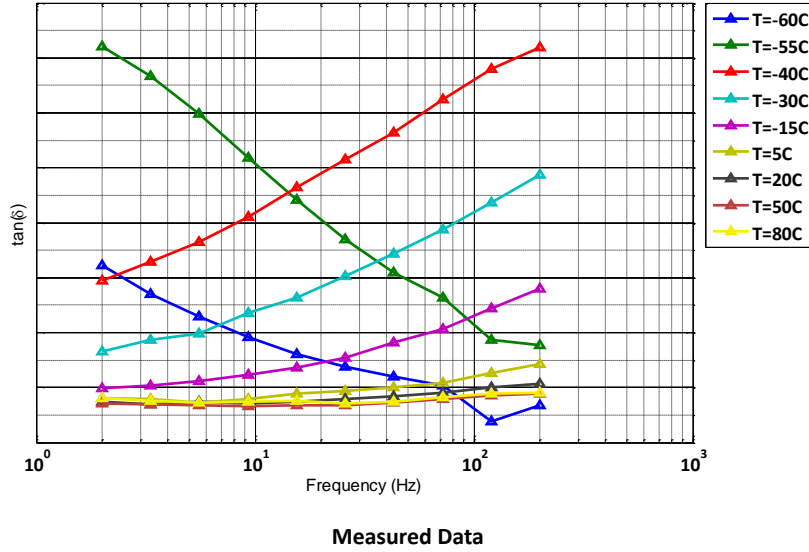
Measured Data

Figure 3.10: The $tan(\delta)$ data that was measured at different frequencies and temperatures is plotted as a function of the solicitation frequency.

(WLF) law. The WLF law is an empirical law using time-temperature superposition to calculate the relationship between temperature and frequency. The law takes the form:

$$log(a_T) = \frac{-C_1(T - T_{ref})}{[C_2 + (T - T_{ref})]}$$

From the mechanical testing we can determine the coeffiicents C_1 and C_2 which vary depending on the rubber properties. To create a Master Curve at a temperature of $23°C$, we use this value as the T_{ref}. Then for the each of the iso-thermal lines shown in Figure 3.10, we can compute the frequency shift a_T that is necessary to represent that data point at a temperature of $23°C$.

This process is shown in Figure 3.11. We see that each iso-therm is shifted so that it forms the master curve at a reference temperature of $23°C$. With the master curve create, a curve fitting can be passed through the data to eliminate the noise.

This process can be repated for the loss modulus and the storage modulus to obtain the master curves for both of these mechanical properties. To determine the time-temperature relationship for temperature other than that of the reference, the frequency shift from the reference temperature must be computed using again the WLF law.

$$log(a_T) = \frac{-C_1(T - T_{ref})}{[C_2 + (T - T_{ref})]}$$
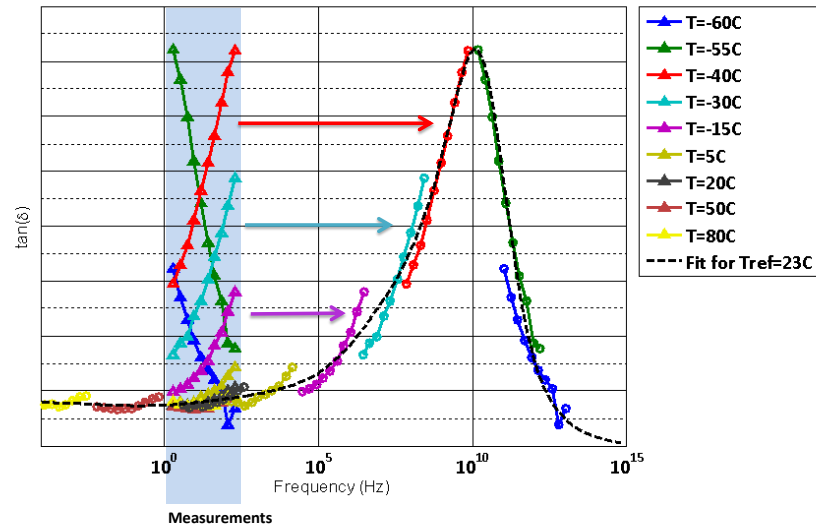
Figure 3.11: The $tan(\delta)$ data that was measured is shifted to a reference temperature of $23°C$ using the Williams-Landel-Ferry law.

Below, we plot the time-temperature curves for the reference temperature $T = 23°C$ as well as at $T = -50°C$ and $T = 75°C$. These experimental curves validate the Material Science theory regarding the effects of temperature and solicitaiton frequency. Figure 3.13 shows that at a temperature of $-50°C$, the rubber approaches a brittle state (characterized by the large modulus) without the rubber being soliciated. This demonstrates the glass transition temperature for unsolicited rubber. Taking a look at the $T = 23°C$ curve, we see that if the rubber were to be solicited in the 10^10Hz range, the rubber would approach a brittle state while at room temperature.

An example of these curves is shown in Figures 3.12, 3.13 and 3.14.
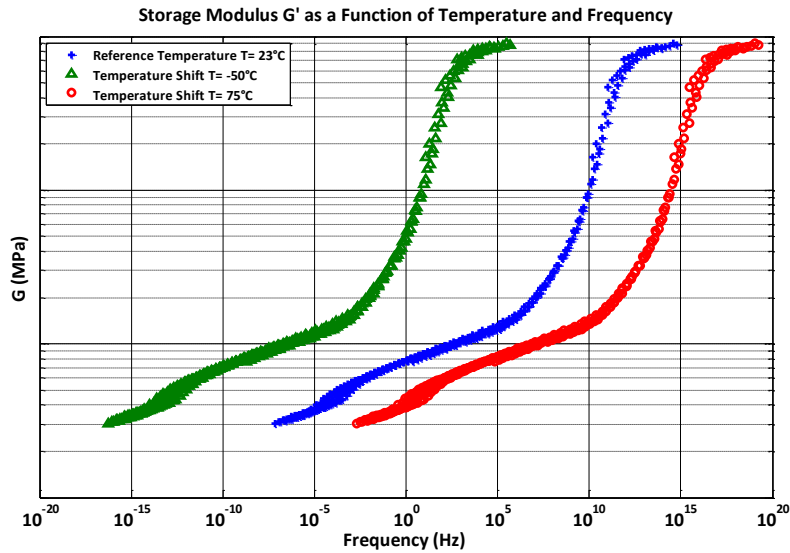
Figure 3.12: Using the WLF law, we extrapolate storage modulus data to the frequency domain for various rubber temperatures
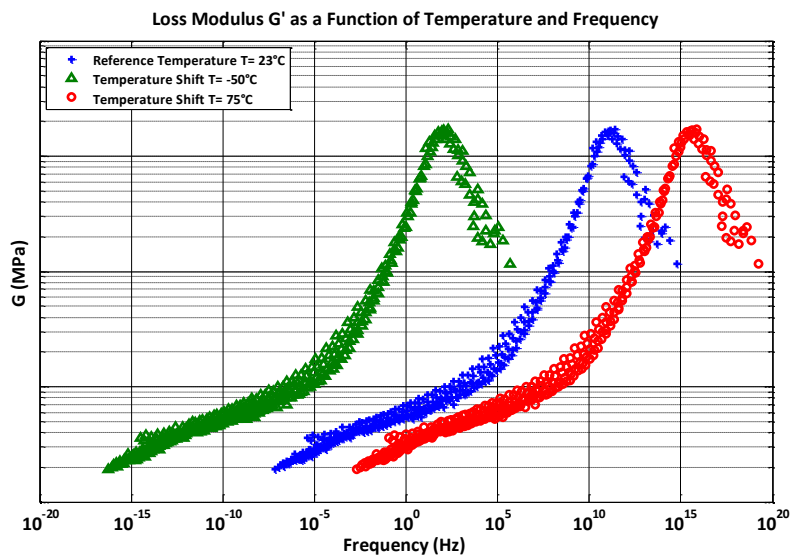
Figure 3.13: Using the WLF law, we extrapolate loss modulus data to the frequency domain for rubber reference temperatures
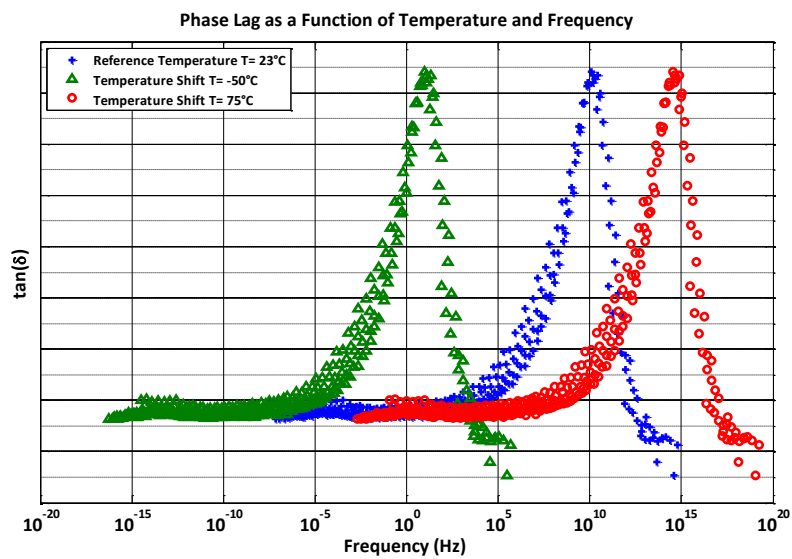
Figure 3.14: Using the WLF law, we extrapolate phase lag data to the frequency domain for various rubber temperatures

3.4 Conclusion

By analyzing the components of the tire, we were able to determine the mechanical characteristics (E or G) of the tire components, most notably the tire tread. These characteristics depend on several factors such as the strain,ϵ, the temperature, T, and the solicitation frequency, ω. The *Williams-Landel-Ferry* equation allows us to extrapolate the data for temperature and frequency to obtain data for the domains that are not possible to test for e.g. high frequency. When all the data is combined, we are able to predict the mechanical characteristics of the rubber as a function of temperature and frequency which will then be used as an input in the modeling. These characteristics will most notably apply in Chapters 5 and 6 as the tire tread mechanical properties will influence the tire-runway friction and the tire stiffness.

Chapter 4

Tire Runway Contact Zone

Summary. Pour modéliser les forces de frottement dans la zone de contact avec le pneu, nous devons connaître les charges verticales dans cette zone. Le modèle de la brosse décrit au chapitre 2 a été dérivé en utilisant une distribution parabolique des pressions dans la zone de contact. Dans ce chapitre, nous utilisons des données issues des essais conduits sur des pneus d'avion qui montrent une distribution des pressions plus plate le long de la longueur de contact. Nous avons donc modélisé la distribution de pressions sous forme de distribution quadratique. Nous avons inséré la distribution quadratique dans la forme du modèle de la brosse et avons tracé la modification de l'aspect de la courbe $\mu - slip$ due à la distribution quadratique des pressions. Ensuite, nous avons introduit le concept d'" aire de contact réelle ". L'aire de contact réelle, A_R est la zone qui est en contact direct atome-atome quand deux surfaces sont en contact. A_R est significativement différente de l'aire de contact apparente, A_A, qui est l'aire totale entre les deux surfaces. Pour étudier l'aire de contact réelle, nous avons d'abord utilisé la théorie du contact de Hertz qui permet d'estimer la taille de la zone de contact entre deux corps élastiques. Hertz a mené des expériences au cours desquelles il a pressé l'une contre l'autre deux sphères de rayon R_1 et R_2 (voir Figure 4.8) et déterminé la taille de la zone de contact, ΔA. La théorie de Hertz nous a permis de déterminer des tendances concernant l'aire de contact réelle : 1. il existe une relation $F^{2/3}$ entre l'aire de contact, ΔA et la force de contact ; 2. si l'aspérité de contact est plus pointue, c'est-à-dire si le rayon de l'aspérité décroît, l'aire de contact réelle diminue. Cependant, la théorie de Hertz a un inconvénient majeur quand elle est appliquée pour le contact entre du caoutchouc et une surface dure : elle suppose que toutes les aspérités ont la même hauteur et se situent dans le même plan. Ainsi, quand le caoutchouc est pressé sur la surface, il entre immédiatement en contact avec toutes les aspérités en même temps. Cette condition idéale est éloignée de la réalité pour une surface dont la rugosité est aléatoire, avec des aspérités dont la hauteur est distribuée de manière aléatoire. Pour remédier à ce problème,

nous avons utilisé la théorie de Greenwood. La théorie de Greenwood donne des résultats intéressants. Généralement, nous pouvons dire que l'aire de contact réelle est proportionnelle à la charge et que la taille moyenne des zones de contact $\Delta A/\Delta N$ est indépendante de la charge. Physiquement, ceci démontre que lorsque la charge augmente et que le caoutchouc s'enfonce sur les aspérités, de nouvelles zones de contact se forment en continu. En conséquence, l'aire de contact réelle s'accroît à deux niveaux : aux jonctions déjà formées et aux nouvelles jonctions formées par le caoutchouc qui s'enfonce et rencontre d'autres aspérités. C'est ce phénomène qui forme la base de la 1st loi du frottement (loi de Coulomb $F_x = \mu F_z$), décrite au chapitre 6. Cependant, les hypothèses simplificatrices ci-dessus considèrent un caoutchouc sur lequel s'exerce une charge nominale. Si la charge verticale sur le caoutchouc devient très élevée, il y aura moins d'aspérités avec lesquelles enter en contact. En conséquence, à un certain point, l'aire de contact réelle ne sera plus proportionnelle à la charge, car le taux de formation de nouvelles zones de contacts ira en diminuant. Cette situation peut se retrouver pour les pneus d'avion qui subissent des pressions de contact supérieures à $25 bars$. Ce phénomène est décrit au chapitre sur la tribologie (6). La fin de ce chapitre modélise la texture de la piste et la distribution des aspérités. Le point important pour les frottements est que la surface typique d'une piste ou d'une autoroute peut être approximée comme une surface fractale auto-affine. Une surface fractale peut être considérée comme présentant des aspérités à l'intérieur d'aspérités. Autrement dit, si nous agrandissons une aspérité de grande taille, nous constatons qu'elle est couverte de plus petites aspérités. Un autre agrandissement de ces petites aspérités révèlera un autre ensemble d'aspérités de taille inférieure. Techniquement, une surface fractale auto-affine ne change pas sous un agrandissement anisotrope.

Goal   *The goal of this chapter is to develop the models to determine the contact length, a, for use in the derived form of the Brush Model (Pg 50) as developed in Chapter 2. The tire contact area and real area of contact will also influence the tribology as derived in Chapter 6*

4.1   Apparent Area of Contact

The contact zone is where the friction forces are generated. As seen in Section 2.3, the size and the pressure distribution of the contact zone influence the shape of the $\mu - slip$ curve and thus the braking force. There are three main properties associated with the contact zone: the length of the contact area, $2a$, the shape of the contact area (rectangular, circular, oval ...) and the contact pressure distribution (parabolic, quartic ...).

The apparent area of contact is the total area *under* the tire that seems to be in contact with the surface. In general, we assume that this area is

that which is enclosed by the perimeter of tire-surface contact zone. Automobile tires have an elliptical shaped contact zone and thus the apparent area of contact can be calculated by $A_{A_{car}} = \pi ab$ where a and b are one half of the ellipses major and minor axis respectively. Aircraft tires, due to their strong internal structure have an apparent area of contact that is nearly rectangular. Thus the apparent area of contact can be calculated by $A_{A_{aircraft}} = 4ab$ where a and b are the one half the length and the width of the tire contact zone respectively.

From the derivation of the Brush Model in Chapter 2, we assume that all parameters remain constant in the lateral direction and derive in the longitudinal direction using the length, $2a$. We use a experimental data to obtain the length of the contact zone, $2a$, through a relation between the vertical load, F_z and the tire pressure, P. For a semi-rigid structure such as a tire, as the vertical load increases, the contact length increases. We interpolate between points.

4.2 Contact Pressure

The relation between the contact pressure and the contact area is complex in tires due to their semi-rigid structure. We can illustrate the complexity by examining the two extremes between a rigid body and an elastic (inflatable) body. We examine a rigid wheel (for example a wooden wheel) and an elastic wheel (for example an inflatable rubber tube). In the case of the rigid wheel, the contact area is fixed. As the wheel is loaded, the contact pressure increases proportionally with the load. Conversely, with an elastic wheel as the load increases the contact area increases. As a result the contact pressure distribution remains constant at $P = F_z/A$. Where P is the contact pressure, F_z is the vertical load on the wheel and A is the contact area. If the elastic wheel is an inflatable body (such as an inflatable rubber tube) then the contact pressure is equivalent to the gauge pressure, P_g inside the tube.

An aircraft tire falls between a rigid and elastic body. Although the tire is inflated with air, the tire housing, including the tire carcass and sidewalls, give the tire additional load bearing capabilities. This results in part of the vertical load being assumed by the internal air pressure and the other part of the load being taken by the internal tire structure. As such, the tire contact length and contact pressure cannot simply be calculated using $F_z = P_g/A$ with either A or P_g constant as in a rigid or elastic body respectively.

4.2.1 Pressure Distribution

Figure 4.2 provides an indication of the pressure distribution for an aircraft tire under static vertical loading conditions. The tire internal gauge pressure is $17 bar$. If the tire was an elastic body, the pressure distribution
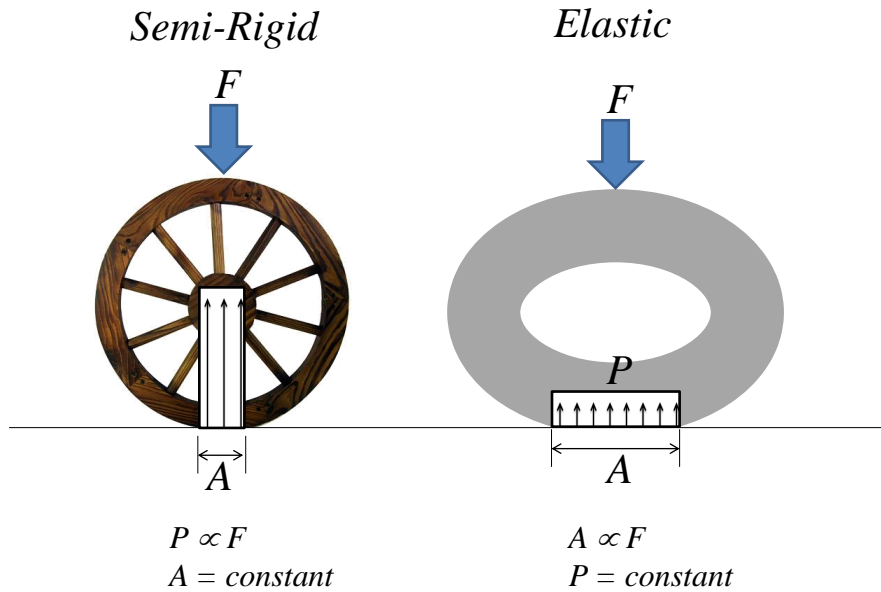
Figure 4.1: Difference between a rigid body and a elastic body

would be constant at $17bar$ across the entire contact zone. However we see in Figure 4.2 that we have contact pressures up to $25bar$ and in Figure 4.3 that the pressure distribution is not quadratic as was derived in the Basic Brush Model (Chapter 2.3).

To provide a *flatter* pressure distribution, we use a quartic polynomial to represent the pressure distribution. In order to determine the effect that a quartic pressure distribution has on the Brush Model, we compare the shape of the $\mu - slip$ curve calculated with two different pressure distributions: the quadratic pressure distribution used in the derivation of Chapter 2.3 and a quartic pressure distribution from [23].

Quadratic Pressure Distribution

$$q_z(x) = \frac{3F_z}{4a}(1 - (\frac{x}{a})^2) \qquad (4.1)$$

Quartic Pressure Distribution

$$q_z(x) = \frac{5F_z}{8a}(1 - (\frac{x}{a})^4) \qquad (4.2)$$

At this time, we will not re-derive the Brush Model with the quadratic pressure distribution. Instead we provide several figures which demonstrate
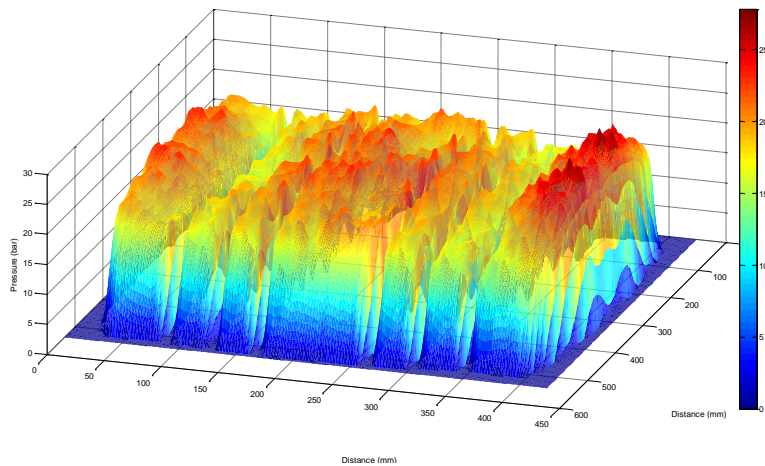
(a) 3D View
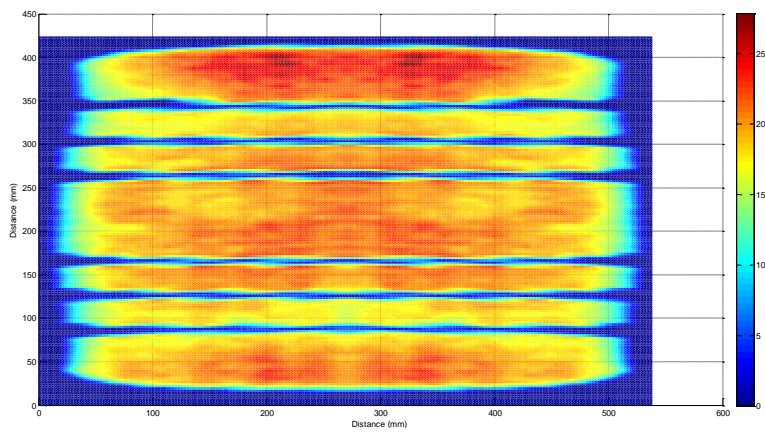
(b) X-Y View

Figure 4.2: Pressure map of the contact zone between an aircraft tire and the runway. The color red represents contact pressures of $25bar$, while the color blue represents contact pressures of less than $5bar$.
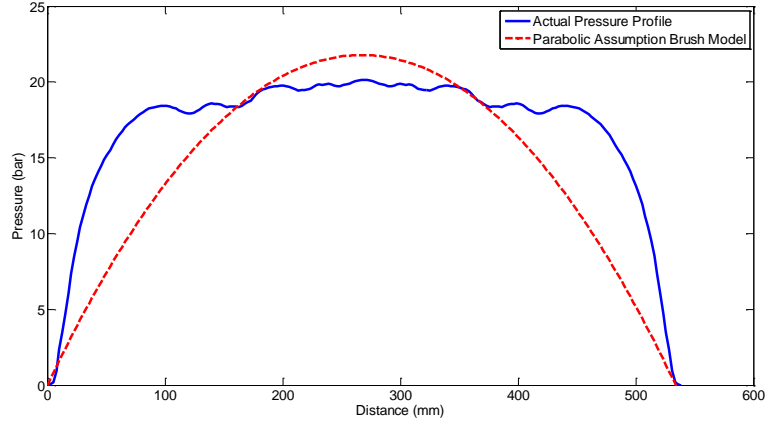
Figure 4.3: Averaged Pressure distribution from the middle tire tread versus the quadratic pressure distribution as used in the derivation of the Brush Model (see Chapter 2.3)

the different form that the Brush Model takes on when a quartic pressure distribution is used.

Figure 4.5 presents the $\mu - slip$ curve for a quadratic and a quartic pressure distribution for specified conditions of μ_{kx}, μ_{sx}, F_z and c_{px} which fall within the normal range. We note that the quartic curve does not have the conspicuous hump that we have come to recognize for the $\mu - slip$ curve. The optimal slip ratio for these two cases are very similar: $s_{opt} = 0.096$ and $s_{opt} = 0.104$ for the quadratic and quartic curves respectively. However, there is a large difference of the point at which *pure-slip* begins i.e. the slip ratio at which the entire tire contact zone is sliding. For the quadratic curve, the s_x^o occurs around 0.175 whereas for the quartic curve the s_x^o is around 0.260. Figure 4.4 plots the difference in the shape along the contact zone. We recall that to the total braking force is the addition of the adhesion forces and the sliding forces.

We perform the same sensibility analysis as in Section 2.5 to observe the effect that changing the input variables C_x, μ_{sx} and μ_{kx} have on the form of the $\mu - slip$ curve. The variables effect is shown in Figure 4.6
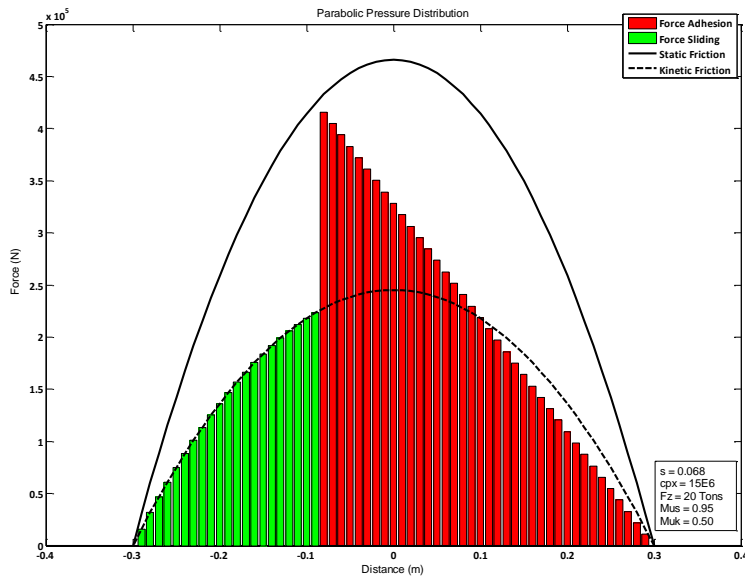
(a) Parabolic Distribution
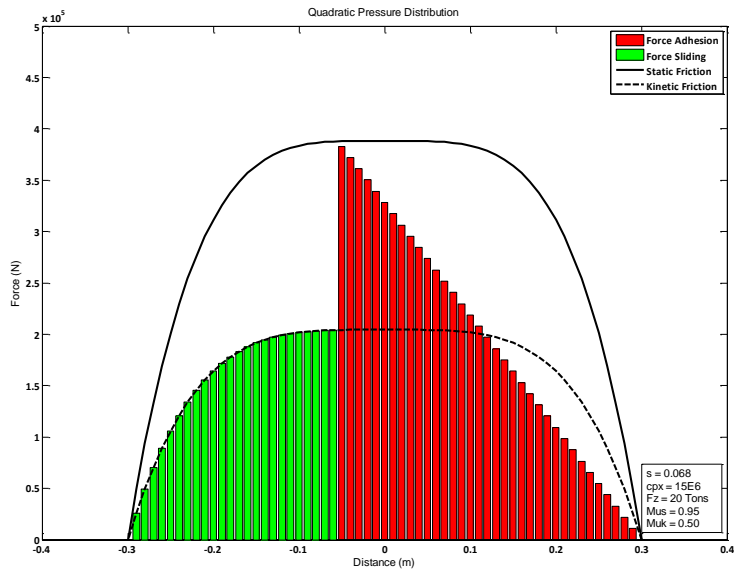
(b) Quadratic Distribution

Figure 4.4: For a fixed slip ratio of 6.8%, we note the difference in form of a parabolic pressure distribution versus a quadratic pressure distribution
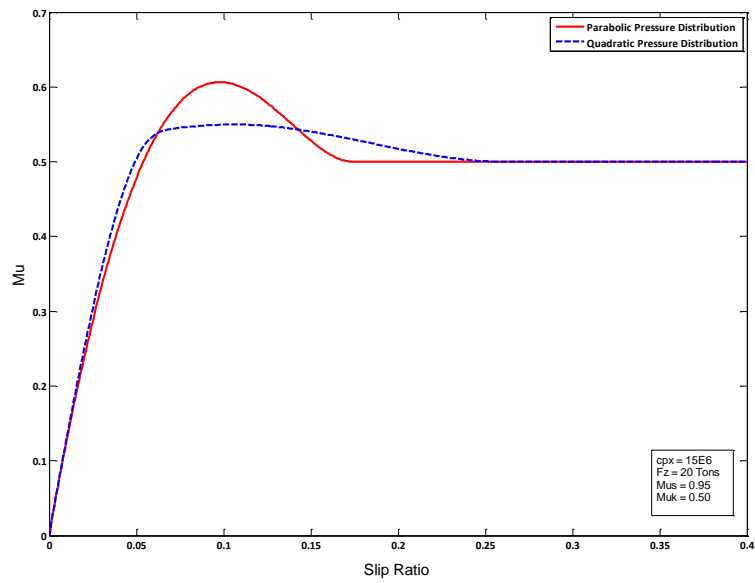
Figure 4.5: The $\mu - slip$ curve for a polynomial pressure distribution (solid line) and a quadratic pressure distribution (dashed line).
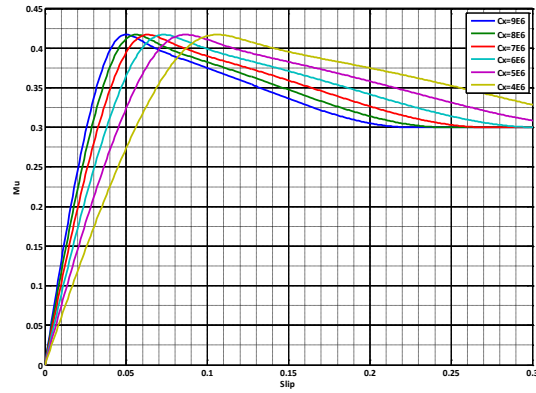
(a) Variation of C_x for Quartic Pressure Distribution
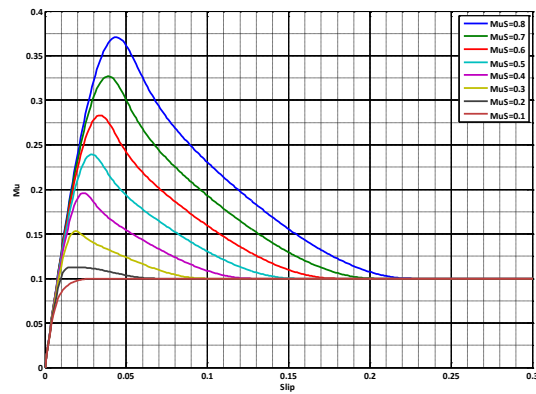
(b) Variation of μ_{sx} for Quartic Pressure Distribution
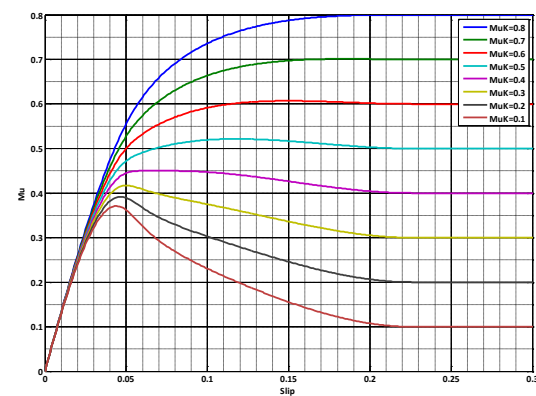
(c) Variation of μ_{kx} for Quartic Pressure Distribution

Figure 4.6: These figures display the form of the μ-slip curve using a quartic pressure distribution. We plot the effects on the $\mu - slip$ curve by varying C_x, μ_{sx} and μ_{kx} in Figures 4.6a, 4.6b and 4.6c respectively

Conclusion   The quartic pressure distribution provides an interesting development step in the Brush Model derivation. At first glance, the pressure distribution seems to be better correlated with the actual pressure distribution measured on aircraft tires. However, the pressure measurements taken for aircraft tires were under static conditions i.e. no rolling or braking. As such, the pressure distribution may not be representative of the pressure distribution when braking. The shape of the $\mu - slip$ curve is significantly different when using a quartic pressure distribution. It remains to be seen (when comparing with flight test data) whether the shape is more or less representative of actual $\mu - slip$ data points.

4.3   Tire Treads

Tire treads on aircraft tires are relatively simple when compared with the complex patterns found on automobile tires. Aircraft tires are most often outfitted with simple circumferential grooves that number between 2 and 5. The primary purpose of these treads is for operations on wet/contaminated runways. These treads allow a channel for the eviction of liquid contaminants (primarily water or slush). This aides in preventing a build up of dynamic pressure in the liquid contaminant, which, if sufficiently large, can lift the tire from the contact surface, resulting in hydroplaning.

Aircraft tires are defined by a *gross contact area* and a *net contact area*. The *gross contact area* is the full area enclosed within the border of the tire-surface contact area. The *net contact area* is the amount of rubber underneath the tire-surface contact area minus the effect of the treads. To give a rough order of magnitude for an aircraft tire (limited treads compared to a automobile), the net contact area is on the order of 10% less than the gross contact area. The net result of having less rubber in contact with the surface (due to the tire treads) is that the contact pressure is higher than if there was not treads.

Aircraft Tire   Automobile Tire

Figure 4.7: Comparison between the tire tread design of aircraft and automobiles

4.4   Real Area of Contact

4.4.1   Introduction

The real area of contact is a concept that will have significant importance for the sliding friction. This effect of the real area of contact on friction will be presented in Chapter 6. Here we will introduce the concept of the real area of contact and give some basic laws used for calculating it.

The real area of contact, A_R refers to the surface area which is in direct atom to atom contact when two surfaces are in contact. As we will see, the A_R is significantly different than the apparent area of contact, A_A, which as we saw in Section 4.1, is the total enclosed area between the two surfaces. Before beginning the derivation, an example using metal contact will provide a quick impression of the real area of contact.

Example 2. *Metal-Metal Contact* *(from [12])*
We assume that as a metal block with mass, M, is lowered onto the hard metal surface that a single contact is formed giving rise to compressive stress. As the block is lowered, more junctions begin to form until the entire load of the metal block is balanced by the contact pressure integrated over the total area, ΔA, of the junctions. We assume that each junction is in a state of incipient plastic flow governed by σ_c, where σ_c is the penetration hardness i.e. the largest compressive stress that the material can support without yielding plastically. Thus from this scenario we can derive

$$Mg = \sigma_c \Delta A$$

For the case of a metal cube of size $10cm \times 10cm \times 10cm$, the load due to gravity is on the order of $\approx 100N$ and the penetration hardness for steel is on the order of $\approx 10^9 N/m^2$. This gives a real area of contact, ΔA of $\approx 0.1mm^2$ compared to the apparent area of contact of $10000mm^2$.

From experiments, we can expect for metal-metal contact approximately 1000 junctions each with a diameter on the order of $\approx 10\mu m$.

4.4.2   Real Area of Contact for Rubber

We have shown that for contact between two surfaces, the real-area of contact is significantly less than the apparent area of contact. Calculating the real area of contact for rubber will have several difficulties related to the viscoelastic nature of rubber as discussed in Chapter 3.

Hertz Contact Theory

We start by describing the Strength of Materials theory as derived by H. Hertz which derives the size of the contact area between two elastic bodies. Hertz performed experiments where two spheres with a radius R_1 and R_2

(see Figure 4.8) are pressed together and the size of the area of contact, ΔA is determined. Hertz found that the contact area $\Delta A_A = \pi r_0^2$ where

$$r_0 = \left(\frac{R_1 R_2}{R_1 + R_2} \right)^{1/3} (E^* F)^{1/3} \tag{4.3}$$

where

$$E^* = \frac{3}{4} \left(\frac{1 - \nu_1^2}{E_1} + \frac{1 - \nu_2'^2}{E_2} \right) \tag{4.4}$$

where E_1, ν_1, E_2, and ν_2 are the elastic modulus and Poisson ratio for material 1 and 2 respectively. From Hertz, we can also determine the distance u that the two surfaces approach each other by

$$u = \left(\frac{R_1 + R_2}{R_1 R_2} \right)^{1/3} (E^* F)^{2/3} \tag{4.5}$$

To apply Hertz theory to our system of rubber sliding on a hard surface we will define rubber as *Material 1* and the rough surface as *Material 2* (See Figure 4.8). The Elastic modulus of rubber is several orders of magnitude smaller than that of a hard surface, $E_2 >> E_1$, thus we simplify 4.4 to

$$E^* = \frac{3}{4} \left(\frac{1 - \nu_1^2}{E_1} \right) \tag{4.6}$$

For the hard surface, we assume for the moment that contact is taking place at one single asperity for which has a radius R_2 that is much smaller than the radius of the rubber i.e. $R_2 << R_1$. As such the ratio $(R_1 R_2)/(R_1 + R_2) \approx R_2$ and thus 4.3 combined with 4.6 evalutes to

$$r_0 = \left(\frac{3}{4} \left(\frac{1 - \nu_1^2}{E_1} \right) F R_2 \right)^{1/3} \tag{4.7}$$

and 4.5 becomes

$$u = \left(\frac{1}{R_2} \right)^{1/3} \left(\frac{3}{4} \left(\frac{1 - \nu_1^2}{E_1} \right) F \right)^{2/3} \tag{4.8}$$

From the Hertz theory, we can determine some tendencies regarding the real area of contact. The first is that the area of contact, ΔA is related to the contact force by $F^{2/3}$. The second is that if the contact asperity is more pointed i.e. the radius of the asperity decreases, the real area of contact decreases.

However the Hertz theory has one major drawback when used for rubber-hard surface contact; it assumes that all of the asperities are of equal height and found in the same plane. Thus when the rubber is lowered onto the surface, it immediately makes contact with all asperities at the same time.

(a) Hertz Spherical Contact

(b) Rubber-Hard Asperity Contact
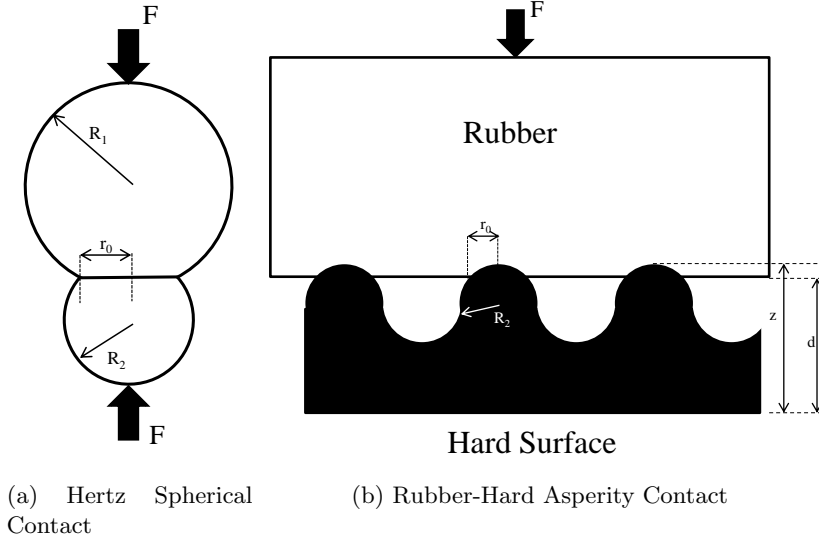
Figure 4.8: Hertz Idealized contact is applied to the case of rubber being pushed against a (or several) hard asperities

This idealized condition is not very realistic for a randomized rough surface which will have a randomized distribution of asperity heights. To treat this problem we use the Greenwood theory as described by Persson in [20](pg 49-51).

Greenwood Contact Theory

We approximate a surface as consisting of N spherical asperities, each with the same radius, R, but with different heights. The rubber is idealized as a flat plane. $N\Phi(z)dz$ is the number of spheres between heights z and $z + dz$ i.e. $\Phi(z)$ is the height probability distribution. If the rubber surface is at a vertical distance d, then all asperities with a height greater than d will be make contact and they will compress the rubber a distance $u = z - d$. If we assume Hertz contact theory and thus equations 4.5 and 4.3 then the asperity contact area equals $\pi r_0^2 = \pi R h = \pi R(z - d)$ and the asperity load, L, equals $R^{1/2}h^{3/2}/E^*$, The total number of contacts is then

$$\Delta N = \int_d^\infty dz N\Phi(z) \tag{4.9}$$

and the area of real contact is

$$\Delta A = \int_d^\infty dz N\Phi(z)\pi R(z - d) \tag{4.10}$$

and the total load

$$L = \int_d^\infty dz N\Phi(z)R^{1/2}(z-d)^{3/2}/E^*$$ (4.11)

Assuming a Gaussian height distribution and simplifying as we are only concerned for z close to d we can approximate $\Phi(z)$ as

$$\Phi(z) \approx Ae^{\lambda(z-d)}$$ (4.12)

where

$$A = \left(\frac{1}{2\pi l^2}\right)^{1/2} e^{-(d-z_0)^2/2l^2}$$

$$\lambda = \frac{d - z_0}{l^2}$$

where l is the rms width of the probability distribution.

Inserting the probability distribution into 4.9 and 4.10 we find

$$\Delta N = NA/\lambda$$ (4.13)

$$\Delta A = \pi NRA/\lambda^2$$ (4.14)

$$L = (2\pi)^{1/2} NR^{1/2}A/(E^*\lambda^{5/2})$$ (4.15)

This theory provides some interesting results. In general we can say that the real area of contact is *proportional* to the load and that the average size of the contact areas $\Delta A/\Delta N$ is *independent* of the load. **Physically this demonstrates that as the load increases and the rubber sinks into the asperities, new contact area are continuously being formed. Consequently, the real area of contact is growing from two sources: at the junctions that have already been formed, and at new junctions as the rubber sinks down and encounters other asperities.** It is in fact this phenomenon that forms the basis of the 1st Law of Friction (Coulomb's Law $F_x = \mu F_z$)which will be described in Chapter 6.

However, the simplifications made above consider *nominally* loaded rubber. As the vertical load on the rubber becomes highly elevated, there will be less asperities with which to come in contact with. As a result, at a certain point the real area of contact will *no longer* be proportional to the load since the rate of formation of new contact areas will decrease. This may be the case for aircraft tires which experiences contact pressures over $25bars$. This phenomenon will be explored in the Chapter on Tribology (6).

Rolling Tire

The previous section has dealt with the tire statically loaded. When a tire is rolling or braking, as in our case, we must also take into account the viscoelastic effect of the rubber as it is solicited by the surface asperities. We recall that the viscoelastic effect was described in Chapter 3(pg 68). As a consequence, in the equations (4.13) to (4.15) we must consider the variation in mechanical strength (E and G) as a function of temperature and frequency.

$$\frac{V=0}{(AFTER\ 15\ s)} \qquad \frac{V=5\cdot5\times10^{-5}}{cm/s}$$

$$\frac{V=1\cdot6\times10^{-2}}{cm/s} \qquad \frac{V=2\cdot5\times10^{-2}}{cm/s}$$

$$\frac{V=5\cdot7\times10^{-2}}{cm/s} \qquad \frac{V=4\cdot6\times10^{-1}}{cm/s}$$

$$\frac{V=7\cdot1\times10^{-1}}{cm/s} \qquad \frac{V=10\times10^{0}}{cm/s}$$
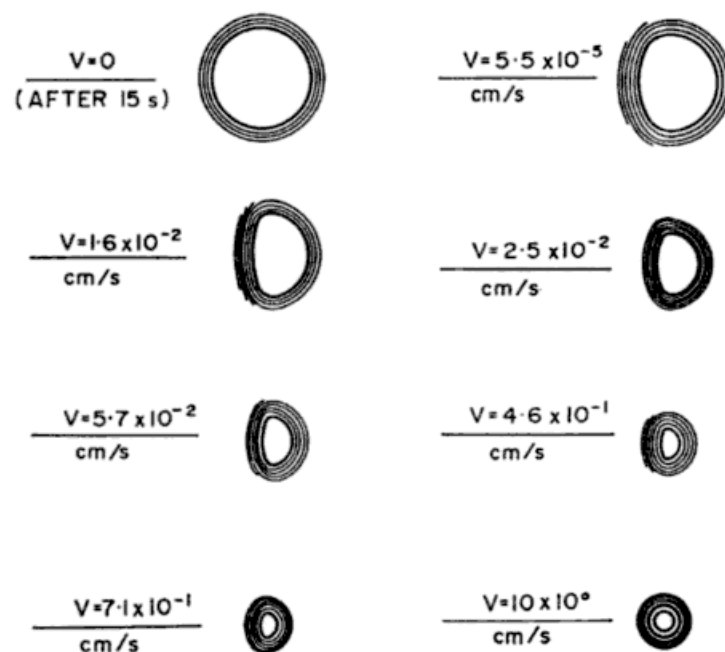
Figure 4.9: Images of a glass sphere rolling in an epoxy resin at differing speeds. From [20] The viscoelastic effect on the size and shape of the contact area is well demonstrated in this Figure. The photographs if the glass sphere rolling in an epoxy resin is taken from below and thus shows the contact area. At rest (top left) the contact area is spherical. As the sphere begins rolling (the sphere is rolling to the left), the contact area deforms. However, above a certain speed the frequency solicitation in the epoxy resin causes the resin to stiffen i.e. the loss shear modulus, E'' becomes large.

4.5 Runway Macrotexture

The previous sections have dealt principally with the characteristics of the tire. This section takes a look at the runway texture and its influence on

the tire-runway contact area. Airport runways are built to strict regulations governing the surface texture for friction characteristics. The majority of airports follow the definitions as set out in *ICAO Aerodrome Design Manual Part 3 - Pavements*. We will not go into details into this documents, but one of the primary criteria is:

– The average surface texture depth of a new surface shall be not less than 1.0 mm.

In terms of detailed analysis of textures, more information is available for automobile surfaces such as highways, roads and bridges. Some examples of surface textures used on highways in Europe is available from the National Concrete Pavement Technology Center [21]. In Figure 4.10, we show the surface characteristics for two highways, one which is has been recently refurbished 3 years ago, while the other highway surface is approximately 7 years old. Although a direct comparison can not be made regarding the amount of degradation of texture with age (since the highways were constructed at different times in different countries), the images show that the peaks of the asperities seem more worn with age.

What is important from a friction point of view is that surfaces typical of a runway or highway can be approximated as *self-affine fractal* surfaces. A fractal surface can be thought of as having *asperities within asperities*. That is to say if we zoom-in on a large asperity we will see that itself is covered in smaller asperities. Another zoom on these small asperities will reveal a set of even smaller asperities. More technically, a self-affine fractal surface does not vary under anisotropic magnification.

In the surface analysis of a runway we can plot the power spectral height density, $C(q)$ as a function of wavelength, q. For wavelengths greater than the cut-off wavelength, q_0 (usually $1mm$ corresponding to the larger stone sizes), we can model the power spectrum as a fractal surface by

$$C(q) = C_0 \frac{q}{q_0}^{-2(H+1)} \tag{4.16}$$

where C_0 is the rms-roughness amplitude. By regarding the power spectral height density as a function of the wavelength, we can determine the Hurst exponent, H, which varies between 0.6 to 0.8 for a typical runway. From H, we can determine the fractal dimension D_f by $H = 3 - D_f$. Thus for a typical runway, we expect a fractal dimension of $D_f \approx 2.2$ to 2.4. [12]
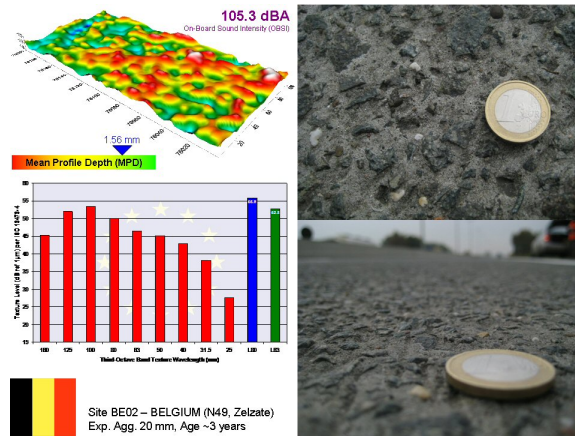
(a) 3 Years Old
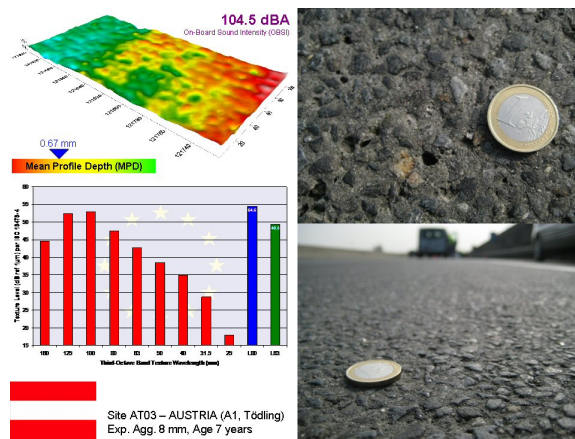
(b) 7 Years Old

Figure 4.10: Runway texture distribution for two different highways of different age [21].

4.6 Conclusion

This Chapter has been used to identify and describe the principal characteristics of the tire-runway contact zone that will affect the friction. We have put in place an empirical model to determine the length of the contact-zone, a, as a function of the vertical load, F_z. This model will provide the value of a to be inputted into the Brush Model equation (Eq. (2.30) pg 50).

The pressure distribution for an aircraft tire has been studied and found to be better represented by a 4th order polynomial then the 2nd order polynomial used in the original derivation in Chapter 2.

In addition, we introduced the concept of real area of contact. The implications of this theory will become more relevant in Chapter 6 - Tribology, but in general we have demonstrated that the rubber rests on the top of asperities which form the hard surface. This has two repercussions: the first being that the actual surface area which is in direct contact between the rubber and the hard surface is a small fraction of the apparent area of contact ($\approx 5 - 10\%$), while the second repercussion is that the contact stress is higher since the vertical load is supported by a much smaller surface area.

Lastly, we modeled the surface texture of typical road / runway surfaces. We found that we can represent a typical runway surface as a self-affine fractal surface. That is to say that large asperities, are themselves covered by small asperities of approximately the same height to wavelength ratio. Due to this fact we can mathematically model the runway texture and it has be shown that a typical runway surface has a fractal dimension of $D_f \approx 2.2$ to 2.4.

Chapter 5

Strength of Materials

Summary. L'objectif de ce chapitre est de produire un modèle capable de prédire la rigidité du pneu dans toutes les conditions. Comme nous l'avons vu dans la dérivation du modèle de la brosse, la zone de contact est constituée de deux forces principales : la force d'adhérence et la force de glissement. La force d'adhérence est due à la déformation longitudinale des poils et cette déformation est gouvernée par la rigidité de chaque poil. Ainsi, la rigidité du poil, et implicitement la rigidité de la bande de roulement, est l'une des premières données à entrer dans le modèle de la brosse qui influencera la taille relative des zones d'adhérence et de glissement. Cependant, les données fournies par les fabricants de pneus démontrent que la rigidité du pneu n'est pas constante : elle varie en fonction de plusieurs paramètres, tels que la pression interne du pneu, la charge verticale sur le pneu, la température, la fréquence de sollicitation et nous pouvons voir que la rigidité n'est pas constante avec la déformation horizontale. Pour obtenir un modèle de la brosse plus robuste, nous devons pouvoir prédire la rigidité du pneu en fonction des conditions. Nous devons donc trouver la source des variations de la rigidité du pneu qui réside dans les caractéristiques des matériaux du pneu. En utilisant la résistance des matériaux et la science des matériaux (Chapitre 3), nous pourrons modéliser la rigidité du pneu. Dans ce chapitre, nous allons dériver un modèle permettent d'estimer la rigidité du pneu sous forme d'une fonction de la charge verticale sur le pneu et de la pression interne du pneu.

Goal *The goal of this chapter is to use Strength of Materials to calculate the tire stiffness, C_p. The tire stiffness will have a direct impact on the variable c_{px} which is used in the derived form of the Brush Model (Pg 50) as developed in Chapter 2.*

5.1　Introduction

The goal of this section is to be able to generate a model that can predict the tire-stiffness under any conditions. Recall that in the derivation of the brush model, the contact zone is made up of two principal forces: the force due to adhesion and the force due to sliding. The adhesion force is due to the longitudinal deformation of the bristles and this deformation is governed by how stiff each bristle is. Thus the bristle stiffness, and implicitly the tread stiffness, is one of the primary inputs into the brush model that will influence the relative size of the adhesion and sliding zones.

However tire manufacturer data demonstrates that the tire stiffness is not constant. It varies depending on several parameters such as the internal tire pressure, the vertical load on the tire, the temperature, the solicitation frequency and it can be viewed that the stiffness is not constant with horizontal deformation. To obtain a more robust brush model, we need to be able to predict the tire stiffness depending on the conditions. For this we must find the source of these variations of tire-stiffness which lies in the material characteristics of the tire. Using the strength of materials and material science (Chapter 3), we will model the tire-stiffness.

5.2　Availability of Data

5.2.1　Manufacturer Supplied Data

As an aircraft manufacturer we do not always have access to the detailed material characteristics of an aircraft tire. Due to the competitive nature of the tire business, tire components and their corresponding characteristics are closely guarded secrets in order to retain the competitive advantage. In general, as an aircraft manufacturer we are supplied with the Mechanical Characteristics of a tire. This report will change slightly from manufacturer to manufacturer and additionally for different tires, but globally the same basic mechanical characteristics will be supplied. In general we will be supplied the following characteristics, usually at several different tire pressures and vertical loads.

- External Dimensions - the radius and width of both a new and grown tire, statically and dynamically (rolling)
- Footprint Test - the width and size (area) of the tire footprint. Including the gross area and the net area (due to the treads).
- Vertical Deflection Test - Under several different gauge pressures, the tire is loaded vertically and the resulting vertical deflection is measured. This test is performed both statically and dynamically. Dynamic testing appears to be performed with a rolling wheel, however the data from the manufacturer is not explicit. During the vertical deflection tests, the rise in gauge pressure due to the tire deformation

is also often noted.

– Cornering Characteristics - The drag force, self aligning torque and cornering force are measured in terms of slip angle.

– Tire Stiffness

– Longitudinal Stiffness - the tire is loaded vertically and then a longitudinal pulling force is placed on the tire. The resulting longitudinal deflection is measured.

– Lateral Stiffness - the tire is loaded vertically and then a lateral pulling force is placed on the tire. The resulting lateral deflection is measured.

– Torsional Stiffness - the tire is loaded vertically and then a torsional moment is placed on the tire and the resulting angular displacement is measured.

These are the basic characteristics that are readily available to us as an aircraft manufacturer. With regards to this thesis work, the most important tests are the tire stiffness tests. This allows for the computation of a global shear modulus, that is a shear modulus of the tire as a system. In order to have additional data than this, either special agreements must be put in place with the manufacturer or once the tires are in our possession certain tests can be performed to determine additional characteristics.

5.3 Experimental Tire Stiffness from Manufacturer Data

We choose a reference aviation tire, Tire B , for which we will attempt to create a simplified model capable of predicting the tire-stiffness for different operating conditions.

The longitudinal stiffness test follows the form as shown in Figure 5.1. The tire is loaded vertically at the tire axle and then a horizontal force, F_x, is applied at the axle and the corresponding deflection, Δx, is measured. For the current data set, this test was performed with three different tire pressures, 10.3, 15.5 and 17.2bar and repeated under four different vertical loads: 5000daN, 10000daN, 15000daN and 20000daN. *Note: That normal operation conditions for a large aircraft are 17.2 bar inflation pressure and 100% loading is 15000-30000 daN.*

Figure 5.2 plots the force-displacement data for a typical longitudinal stiffness test.

From the force-displacement data in figure 5.2 we can compute the tire-stiffness by taking the derivative $C_x = \Delta F / \Delta x$. However the raw data contains small oscillations. When computing the slope using two adjacent points, significant oscillations are revealed which makes identification of the tire stiffness difficult. An example of the plotted tire stiffness using raw data is plotted in figure 5.3.
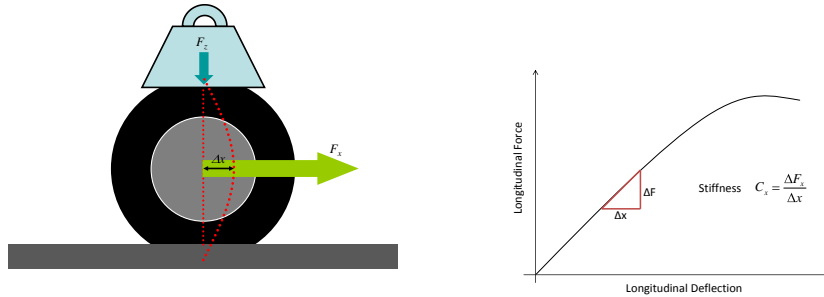
Figure 5.1: Schematic of tire stiffness testing. Results are of the form of a force-displacement curve. The slope of this curve is the tire-stiffness.

In order to remove the oscillations, polynomial curve fitting is used. Due to the relative simplicity of the force-displacement curves, a polynomial to the fourth degree is sufficient to accurately plot the data (Figure 5.4).

From figure 5.4 we are able to determine several characteristics about the tire-stiffness. The first is that the tire-stiffness increases with an increasing vertical load. We know that as the vertical load increases the tire's vertical deformation increases. This leads to the supposition that the tire-stiffness increases as the vertical deformation increases. However, manufacturer data is also available for several different tire pressures. From this data we find that as the pressure decreases the tire-stiffness decreases. Our original hypothesis was that the tire-stiffness increased with deformation, however the results from different pressures contradicts this results because as pressure decreases, the deformation increases. The exact mechanics are not fully understood, but it is supposed that the internal tire pressure adds rigidity to the tire-structure.

In order to model these effects, we first need to develop the relationship between the tire-stiffness and the mechanical properties of the tires. This is developed using the strength of materials which will incorporate the shear modulus and the form of the tire to calculate the tire-stiffness.

Figure 5.2: Force-Displacement curves for an aircraft tire for different vertical loads

Figure 5.3: Taking the derivative of the raw force-displacement data leads to significant noise in the curves.

Figure 5.4: Using a 4th order polynomial to smooth the tire-stiffness curves.

5.4 Tire-Stiffness as a Function of the Shear Modulus and Tire Shape

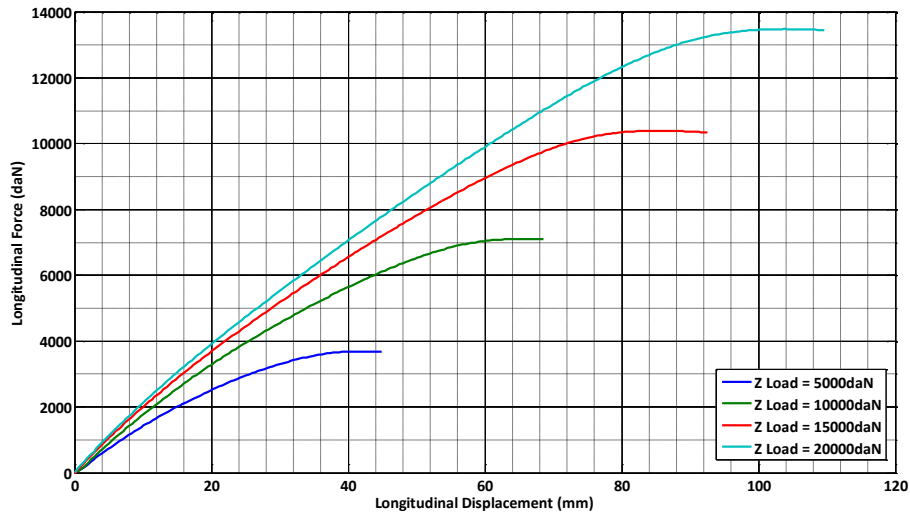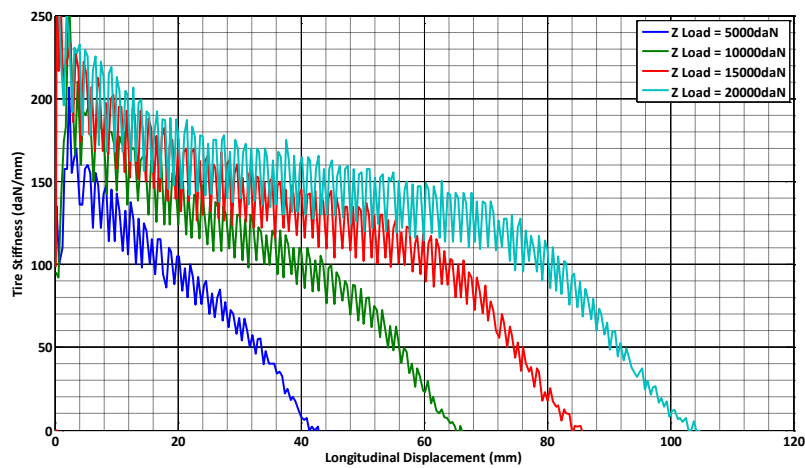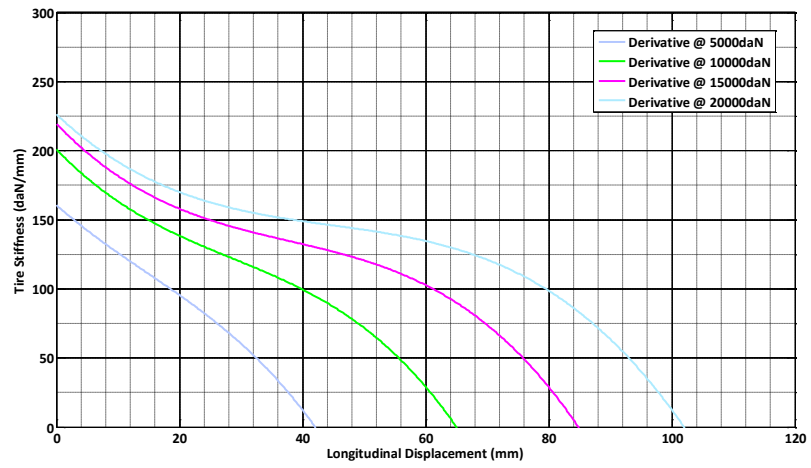If we regard the forces acting in the adhesion zone of the tire-runway contact zone, we note that the deformation is due to shear. The contact between the tire and runway is fixed while the axle of the tire continues to move forward. This shearing motion deforms the tire. The basic derivation of the shear modulus is as shown in figure 5.5 using a rectangular element. The shear modulus can be derived as

$$G = \frac{\tau_{xy}}{\gamma_{xy}} = \frac{F/S}{\Delta x/l} = \frac{Fl}{S\Delta x} \tag{5.1}$$

where τ_{xy} is the shear stress, γ_{xy} is the shear strain, F is the horizontal force, S is the reference surface area upon which the force is acting, Δx is the measured horizontal displacement and l is the height/thickness of the rectangular block.

We note that in the equation for the shear modulus we have the ratio $F/\Delta x$ which is the tire definition of stiffness. Substituting the tire-stiffness C_x we find that we can calculate the tire-stiffness as a function of the shear modulus, G.

$$C_x = \frac{GS}{l} \tag{5.2}$$

However we must take into account that a tire is neither or rectangular in shape, nor is it one homogeneous material. In fact a tire is a complex system composed of a myriad of elements that each contribute to the tire stiffness. Figure 5.6 shows the components of an automobile tire which clearly shows the complexity involved in tire construction. To simplify this we will make the assumption that the tire is composed of two elements: the tread and the carcass. These two elements will be rectangular in shape and thus the stiffness of each component can be computed using equation 5.2. We note that tire-stiffness coefficients can be added in the same way that combinations of springs are added. That is to say, springs in parallel are added, while springs in series are added using the inverse law. Thus the global tire-stiffness can be represented as

$$\frac{1}{C_g} = \frac{1}{2C_c} + \frac{1}{C_t} \tag{5.3}$$

Where the subscript g, c and t represent *global*, *carcass* and *tread* respectively. Replacing the stiffness coefficient with the formula for the shear modulus we arrive at the formula to predict the global tire-stiffness (C_g). (Figure 5.8

$$\frac{1}{C_g} = \frac{l_c}{2G_cS_c} + \frac{l_t}{G_tS_t} \tag{5.4}$$
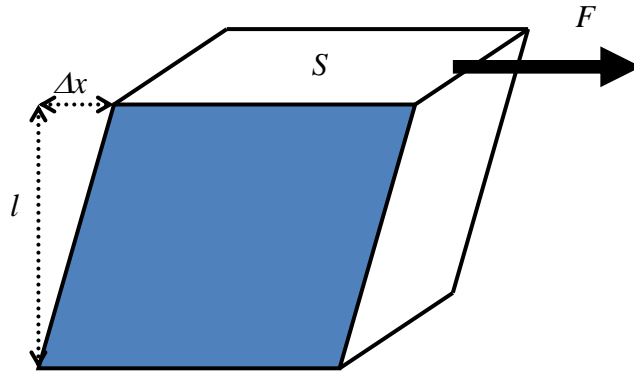
The derivation of the shear modulus based on the deformation of a rectangular element due to a shearing force.

Figure 5.5
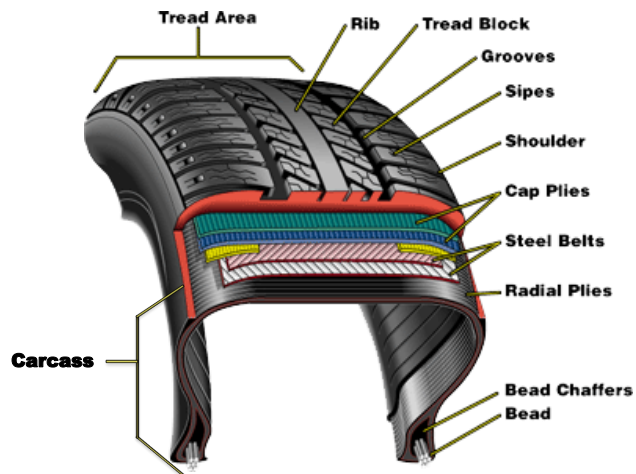
Figure 5.6: General schematic of automobile tire construction.
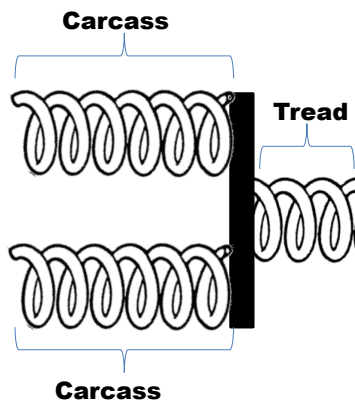
$$\frac{1}{C_{global}} = \frac{1}{2C_{carcass}} + \frac{1}{C_{tread}}$$

Figure 5.7: Combining tire-stiffness coefficients follow the same logic as adding spring stiffness'. The two sides of the carcass are treated as springs in parallel while they are attached to the tread as springs in series.

The proceeding section will develop models to predict the changes in the tire-stiffness due to the deformation of the tire under different pressures and vertical loads. external parameters.
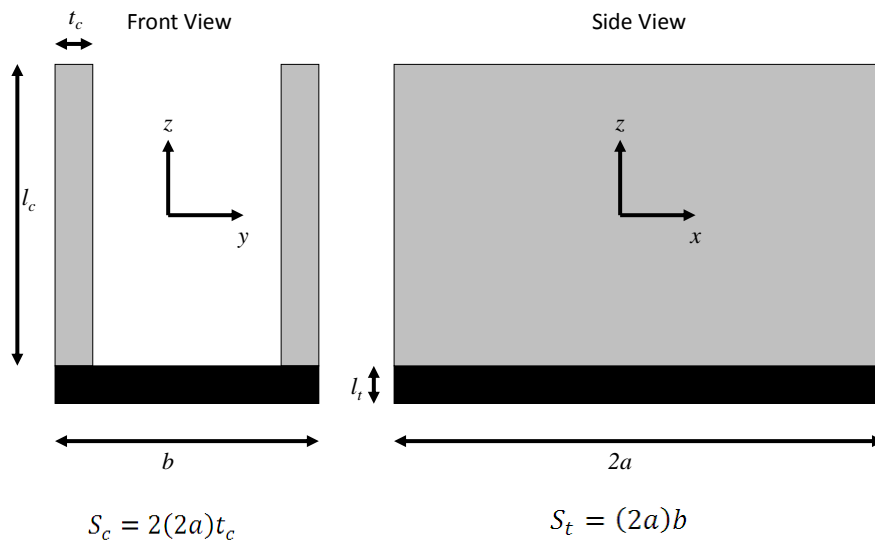
Figure 5.8: Representation of the tire-surface contact zone as two elements, the tread and the carcass. It is this area that contributes to the tire-stiffness.

5.5 Modeling Tire-Stiffness as a Function of Deformation

In order to compute the tire-stiffness as a function of deformation we will use equation 5.4. The first assumption that we will make is that the shear modulus (G) of the tread and the carcass are independent of the deformation of the tire. This leaves four variables to affect the tire-stiffness: the two surface areas S_c and S_t and the two thicknesses l_c and l_t. Due to the unknowns in treating a complex object such as a tire, we will depart with two different hypotheses and then use the manufacturer's data to test.

5.5.1 Hypothesis 1 - Tire-Stiffness Proportional to Tire-Runway Contact Size

A tire deforms as a function of two parameters: the tire internal pressure and the vertical load (F_z) on the axle. We know that as the tire pressure decreases the vertical deformation (Δz) increases. In the same manner, as the vertical load increases the vertical deformation increases. An increase in the deformation of the tire has two consequences: the tire-runway contact area grows, and the distance between the axle and the surface (an effective radius) decreases. A schematic is presented in Figure 5.9.

We note from the general definition of the shear modulus (Equation (5.2)) that as the surface area of an element increases the stiffness increases. This agrees with the manufacturer data that as the deformation increases the tire-stiffness increases. Additionally, the general definition of the shear modulus demonstrates that as the thickness of an element decreases, the stiffness will increase. This also is in agreement with the manufacturer data.

Therefore hypothesis 1, will use surface area of the tire-runway contact as the reference surface and the height of the elements will be derived from the height between the surface and the rim. We will make the assumption that the thickness of the tire tread is constant and independent of the vertical load. The deformation of the tread could be taken into account using *Young's Modulus* (E) of the tread, however the effect is seen as negligible. The change in height of the carcass changes with the vertical deformation will be taken into account in the model. This information is summarized in Table 5.1 and Figure 5.8.

As outlined in Section 5.2, the manufacturer performs footprint tests and vertical deformation tests. This data will be used to determined the dimensions of S and l for use in the modeling. Below and example using data from a Tire B will be used. The calculation is done using the nominal pressure for this tire which is $17.2 bar$.

For the modeling in this section, we do not wish to take into account the variation of the tire-stiffness with the horizontal deflection (Δx). Therefore

Deformation ↑ as Pressure ↓ And/Or Vertical Load ↑
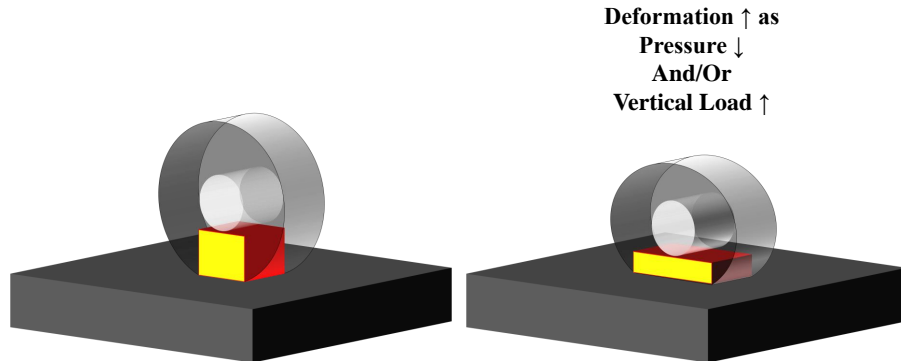
Figure 5.9: Effect of deformation on the surface area and the thickness of the elements used to compute the tire-stiffness

Table 5.1: Hypothesis 1 assumes the following constraints on the tire geometry

Variable	Reference
Sc	The reference surface area for the carcass will be the thickness of the carcass walls multiplied by the length of the tire-runway contact zone
St	The reference surface for the tread will be the gross surface area of the tire-runway contact zone derived from manufacturer testing.
lc	The reference height of the carcass will be the height between the surface and the wheel rim minus the thickness of the tire tread
lt	The reference height of the tread will be the thickness of the tire tread and remains constant under deformation

Table 5.2: Characteristic Data to be used for Hypothesis 1

Load	Footprint	Footprint Length	Vertical Deflection	Height Rim to Ground
(daN)	(cm2)	(mm)	(mm)	(mm)
5000	392	200	24.9	383.1
10000	713	274	43.8	364.2
15000	983	339	59.3	348.7
20000	1225	391	75.6	332.4

we will choose constant values of the tire stiffness corresponding with small deflections. Using the coefficients in Table 5.3, we will use the tire-stiffness at a displacement of $8mm$. The value of $8mm$ was chosen by regarding the data and choosing a value with small displacement but was less affected by the noise and oscillations of the first couple millimeters of deflection. Data in tabulated in figure 5.3.

Table 5.3: Tire Stiffness calculated for a horizontal displacement of $8mm$

Vertical Load (daN)	Tire-Stiffness @ X=8mm (N/mm)
5000	1323.4
10000	1694.96
15000	1879.6
20000	1976.9

We now have all the information necessary to predict the tire stiffness. The hypothesis is that the shear moduli of the tread and the carcass are constant values. However these values are unknowns. In general we will assume that the tread is composed of hard rubber of which shear modulus values vary between $1 - 4MPa$. We wish to test if, keeping the shear moduli constant, the change in surface area and deflected height are able to predict the change in tire-stiffness. We will use the following procedure to develop the model.

PROCEDURE

1. Rearrange equation (5.4) to solve for G_c

$$\frac{1}{G_c} = \frac{2S_c}{l_c}\left(\frac{1}{C_g} - \frac{l_t}{G_t S_t}\right)$$

2. Choose a value for the shear modulus of the tread (G_t) corresponding with values found in literature (between $1 - 4MPa$)

3. Use the experimentally derived tire-stiffness at near-nominal loads of 20,000daN to determine the shear modulus of the tread.

4. Using fixed values of G_t and G_c use equation (5.4) to predict the tire-stiffness when the surface area (S) and height (l) change with varying vertical loads (F_z).

$$\frac{1}{C_g} = \frac{l_c}{2G_c S_c} + \frac{l_t}{G_t S_t}$$

5. Compare the predicted and the experimental values of tire-stiffness C_g

The results are tabulated below in table 5.4 and 5.5.

Table 5.4: Predicted and Experimental Stiffness for $G_t = 4MPa$ and $G_c = 55.6MPa$

Vertical Load (daN)	Predicted Tire-Stiffness (N/mm)	Experimental Tire-Stiffness (N/mm)	Percent Difference
5000	805	1323	39.11%
10000	1227	1695	27.56%
15000	1615	1879	14.04%
20000	1977	1977	0.00%

Table 5.5: Predicted and Experimental Stiffness for $G_t = 1MPa$ and $G_c = 176MPa$

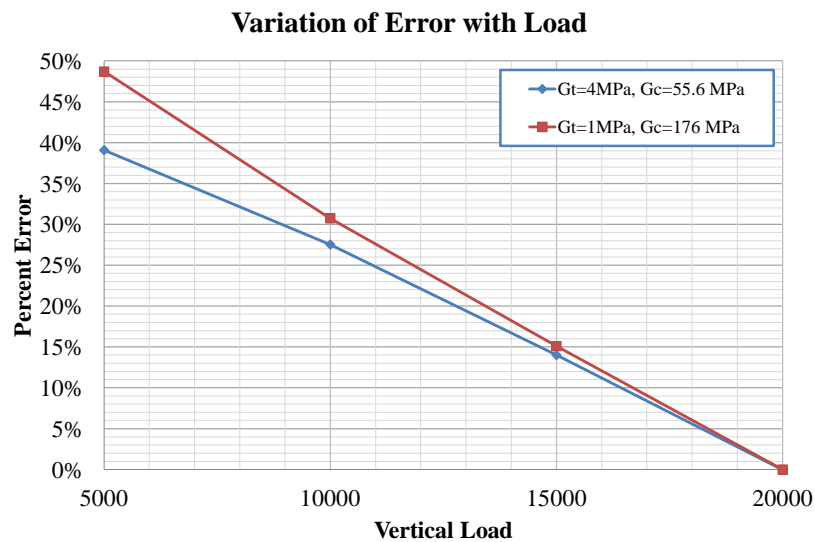| Vertical Load (daN)	Predicted Tire-Stiffness (N/mm)	Experimental Tire-Stiffness (N/mm)	Percent Difference
5000	678	1323	48.70%
10000	1174	1695	30.73%
15000	1595	1879	15.09%
20000	1977	1977	0.00%

Figure 5.10: Percent Error of predicted tire-stiffness to the experimental values using hypothesis 1.

5.5.2 Hypothesis 2 - Whole Tire Contributes to Tire-Stiffness

In the first hypothesis, we surmised that only the area directly above the tire-contact area contributed to the tire-stiffness. In this way, as the load/pressure changed, the area of the tire-surface contact zone changed. The second hypothesis is that the entire tire contributes to the tire-stiffness. In this sense the size of the tire-surface contact zone does not affect the tire-stiffness. Thus S_c and S_t are constant. However we still take into account the change in height to take into account the deformation caused by the changes in load/pressure. Thus in equation (5.4) we now only have one changing variable, l_c.

As the force is applied at the axle, we will take the area of half the tire. Thus the width remains the same, we will use the length equal to πR. Thus $S_c = 2t_c\pi R$ (to take into account the two sides of the carcass) and $S_t = \pi Rb$. We follow nearly the same procedure as in hypothesis 1 except that the surface area (S) will remain constant.

PROCEDURE

1. Rearrange equation (5.4) to solve for G_c

$$\frac{1}{G_c} = \frac{2S_c}{l_c}\left(\frac{1}{C_g} - \frac{l_t}{G_tS_t}\right)$$

2. Choose a value for the shear modulus of the tread (G_t) corresponding with values found in literature (between $1 - 4MPa$)

3. Use the experimentally derived tire-stiffness at near-nominal loads of 20,000daN to determine the shear modulus of the tread.

4. Using fixed values of G_t and G_c use equation (5.4) to predict the tire-stiffness when the height (l) changes with varying vertical loads (F_z).

$$\frac{1}{C_g} = \frac{l_c}{2G_cS_c} + \frac{l_t}{G_tS_t}$$

5. Compare the predicted and the experimental values of tire-stiffness C_g

The results are tabulated in 5.6, 5.7 5.8 and the percent error is plotted in 5.11

5.5.3 Conclusion

Considering the entire tire as contributing to the tire-stiffness (hypothesis 2) seems to provide the more accurate results. It should be noted that the normal operating conditions of the tire are above $15000daN$ where we see that the error is less than 3%. Hypothesis 2 also has the advantage of having only one input variable (l) that varies as a function of the vertical load. Thus we obtain a direct correlation for the tire-stiffness, C_x (for a

Table 5.6: Characteristic Data to be used for Hypothesis 2

Load	Footprint	Footprint Length	Vertical Deflection	Height Rim to Ground
(daN)	(cm2)	(mm)	(mm)	mm
5000	5800	1282	24.9	383.1
10000	5800	1282	43.8	364.2
15000	5800	1282	59.3	348.7
20000	5800	1282	75.6	332.4

Table 5.7: Predicted and Experimental Stiffness for $G_t = 4MPa$ and $G_c = 14.4MPa$

Vertical Load (daN)	Predicted Tire-Stiffness (N/mm)	Experimental Tire-Stiffness (N/mm)	Percent Difference
5000	1493	1323	-12.86%
10000	1786	1695	-5.39%
15000	1874	1879	0.24%
20000	1977	1977	0.00%

Table 5.8: Predicted and Experimental Stiffness for $G_t = 1MPa$ and $G_c = 16.4MPa$

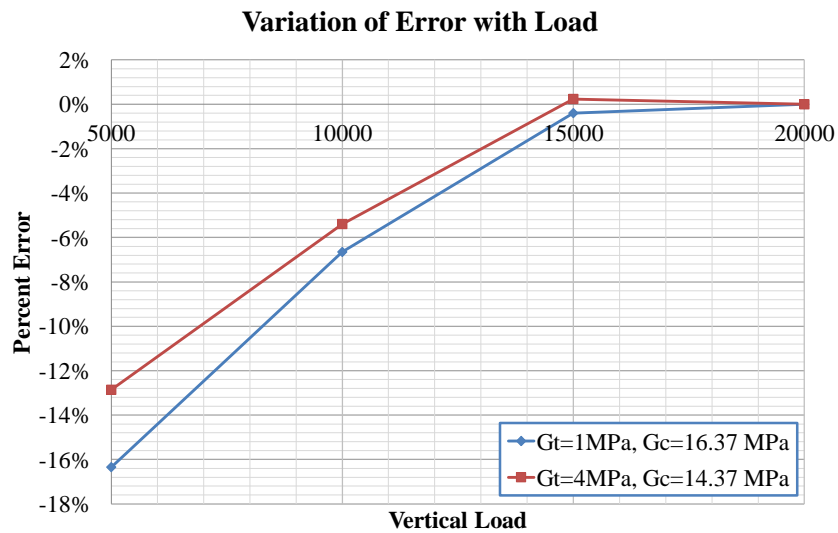| Vertical Load (daN)	Predicted Tire-Stiffness (N/mm)	Experimental Tire-Stiffness (N/mm)	Percent Difference
5000	1539	1323	-16.34%
10000	1807	1695	-6.65%
15000	1886	1879	-0.40%
20000	1977	1977	0.00%

Figure 5.11: Percent Error of predicted tire-stiffness to the experimental values using hypothesis 2.

given tire pressure), that varies directly as a function of the tire-deflection, Δz. This is in contrast to hypothesis 1 which had two input variables (S and l) that varies with the vertical load and the error is significantly larger than hypothesis 2.

5.6 Modeling Vertical Deformation as a Function of Changing Tire-Pressure and Vertical Loads

From Section 5.5 we have a model which can calculate the tire-stiffness, C_x, as a function of the vertical load, Δz. However, the analysis was made for one tire pressure (17.2 bar) and used directly the vertical deflection obtained from manufacturer testing. In order to complete the modeling, we must have find a way to calculate the vertical deflection as a function of the tire pressure, P, and the vertical load, F_z.

Figure 5.12 shows the manufacturers results for vertical deflection for various vertical loads and tire-pressures. The curves can be seen to be non-linear. However, this data represents a wide range of vertical loading not seen in normal operating conditions. For example, the tire is subjected to vertical loads of over $1250KN$ or $125,000daN$. This is nearly $4x$ the nominal (100%) of $33600daN$. If we restrict the data to opertional conditions of between $5000daN$ and $35000daN$ we can see that the vertical force-deflection curves are nearly linear. (Figure 5.13)

5.6.1 Double Linearization

Plotting linear trend lines through this operational load area gives slope and intercept values for each value of tire pressure. There are of the form

$$F_z = m_1\Delta z + b1 \tag{5.5}$$

We obtain a set of m_1 and b_1 values for each pressure. If we then plot these slope and intercept values as a function of pressure, we can also linearize these values in the form

$$m_1 = m_2 P + b_2 \tag{5.6}$$

$$b1 = m_3 P + b_3 \tag{5.7}$$

Resulting in the final equation that allows us to calculate the vertical-force-deflection curve for any inputs.

$$F_z = (m_2 P + b_2)\Delta z + m_3 P + b_3 \tag{5.8}$$

We then rearrange this equation to obtain the deflection as a function of the vertical load

$$\Delta z = \frac{F_z - m_3 P - b_3}{m_2 P + b_2} \tag{5.9}$$

Using experimental data, we obtain the final form of the coefficients as seen in Figure 5.14. To test the error associated with this model we calculate a predicted vertical deflection based on a given pressure and vertical load and compare this to the experimental values. Figure 5.15 gives the results of this
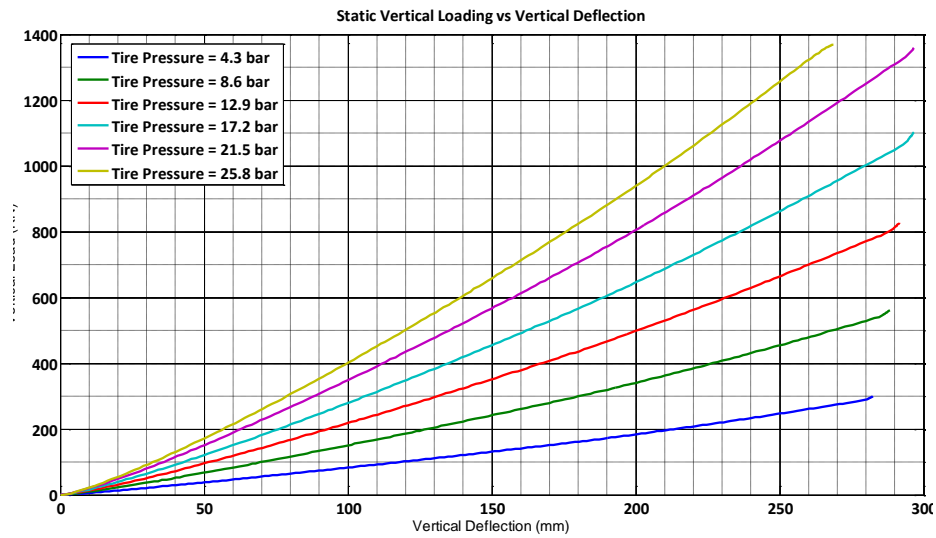
Figure 5.12: Vertical Deflection vs Vertical Load data set for Tire B
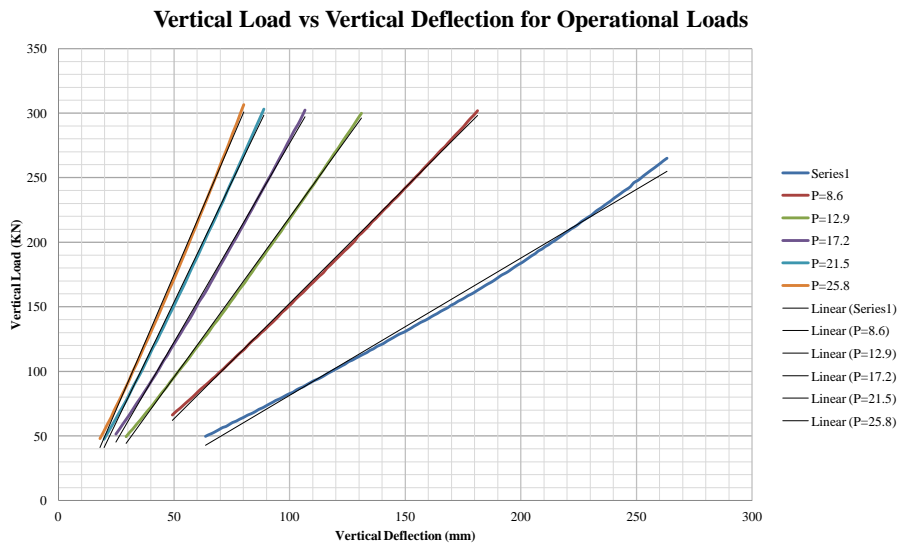
Figure 5.13: Vertical deflection curves are nearly linear for operational loading conditions (between 5000daN and 33000daN)

Slope and Intercept Values vs Pressure

		Linear Fit $m_1 = m_2(P) + b_2$ $b_1 = m_3(P) + b_3$		
		m2	**b2**	**R²**
Slope (m1)		0.1464	0.5168	0.9958
		m3	**b3**	**R²**
Intercept (b1)		-0.4605	-22.569	0.9745
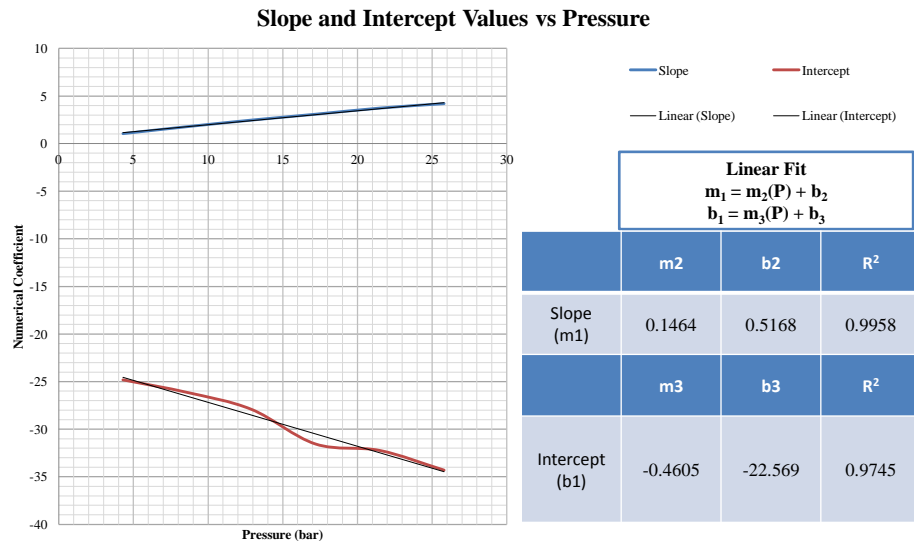
Figure 5.14: We use a double linearization to model the vertical deflection Δz as a function of the tire pressure, P, and the vertical load, F_z. The plot above shows that the hypothesis that both effects are linear is correct as both the slope and intercept line are linear.

test. As we can see, the errors grow at the extremities of the input variables. That is to say, the largest errors are found when the pressure $P = 25.8$ and $P = 4.3$ as well as when the vertical load is at 5000daN (50KN). However we note that for mid-range vertical loads (F_z) and pressures (P), those most normally found in operations, we have less than 5% error which is deemed sufficient for this study.

This model to predict the vertical deformation can now be inputted into the tire-stiffness model developed in Section 5.5.2 to predict the tire-stiffness as a function of the pressure and vertical load.

Table 5.9: Linear fit to model the vertical deflection of the form $F_z = m(\Delta z) + b$

Pressure (bar)	m	b	R2
4.3	1.063	-24.8	0.996
8.6	1.789	-26.1	0.999
12.9	2.472	-27.9	0.999
17.2	3.085	-31.6	0.999
21.5	3.724	-32.2	0.999
25.8	4.185	-34.3	0.999
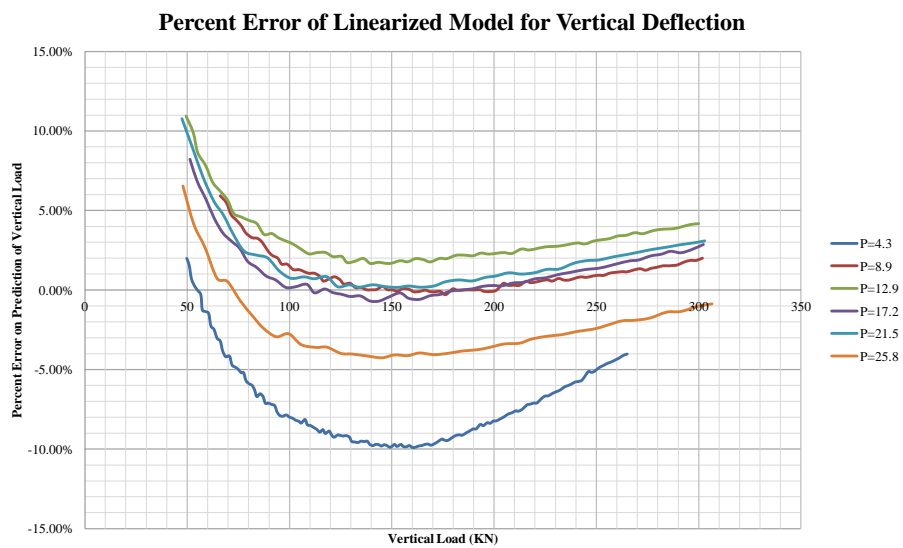
Figure 5.15: Percent Error for the linearized model of vertical deflection

5.7   Complete Model Tire-Stiffness

Putting the tire-deflection model into the tire-stiffness model we arrive with a final equation

$$\frac{1}{C_g} = \frac{l_c}{2G_c S_c} + \frac{l_t}{G_t S_t} \tag{5.10}$$

With the vertical deflection model we have

$$\frac{1}{C_g} = \frac{R - l_t - \frac{F_z - m_3 P - b_3}{m_2 P + b_2}}{2G_c S_c} + \frac{l_t}{G_t S_t} \tag{5.11}$$

Using the manufacturers tire-stiffness data for different pressures and vertical loads we can compare this against our predictive model. To neglect the effect of elongation on the tire-stiffness we choose constant tire-stiffness values at a small displacement of $x = 8mm$.

Table 5.10 gives the results of this model for Tire B

Table 5.10: The complete model allows to predict the tire-stiffness as a function of tire internal pressure and vertical load

Experimental Data

Pressure (bar)	Load (daN)			
	5000	10000	15000	20000
10.3	1251	1476	1539	1531
15.5	1307	1648	1833	1887
17.2	1323	1695	1880	1977
18.9	1336	1678	1932	2021

Predicted Data

Pressure (bar)	Load (daN)			
	5000	10000	15000	20000
10.3	1757	1896	2060	2254
15.5	1708	1801	1906	2024
17.2	1698	1782	1876	1979
18.9	1689	1766	1850	1943

Percent Error

Pressure (bar)	Load (daN)			
	5000	10000	15000	20000
10.3	40.40%	28.50%	33.80%	47.20%
15.5	30.70%	9.30%	4.00%	7.20%
17.2	28.30%	**5.10%**	**-0.20%**	**0.10%**
18.9	26.40%	**5.20%**	**-4.20%**	**-3.80%**

5.7.1 Conclusion

The derivation proves that we can obtain an approximate model of the tire-stiffness using the material properties of the tire carcass and the tire tread. This model takes into account the vertical deformation as a result of changing vertical loads and/or changing tire pressures. Although we have proven a rough estimation is possible, the model is not completely able to take into account the physical effects.

As the vertical force increases the vertical deflection of the tire *increases* and the tire-stiffness C_x *increases*. The change in the characteristic height of the carcass, l_c allows us to take into account this effect. However for the case if changing tire pressure, as the tire-pressure decreases the vertical deflection of the tire *increases*, but the manufacturers data shows that the tire-stiffness *decreases*. This is the opposite of the effect from the vertical load, and thus using the characteristic height of the carcass, l_c, we do not obtain the correct effect. We hypothesize that the internal tire pressure contributes to the rigidity of the carcass. This can be taken into account with the addition of a shape factor within the strength of materials. However, for the current modelisation we have sufficient accuracy for the nominal vertical loads and tire pressures that the effect of tire pressure will not currently be taken into account.

This modeling was done assuming a small, constant horizontal deflection of the tire. Figure 5.3 clearly shows that the stiffness diminishes significantly as the horizontal displacement increases. Knowing that as a bristle moves through the contact zone, the deformation increases, the bristle stiffness as a function of horizontal displacement must be taken into account. This will be addressed in the following section using Material Science as well as the effects of temperature and frequency.

Chapter 6

Tribology

Summary. La loi de Coulomb, $F_x = \mu F_z$, stipule que la force de résistance au mouvement, F_x, (ou force de frottement) d'un bloc est proportionnelle à la force verticale F_z. Le coefficient de proportionnalité est appelé coefficient de frottement. Il est souvent symbolisé par la lettre grecque μ (Mu). En général, nous considérons que le coefficient de frottement est constant. Même si des progrès significatifs ont été accomplis depuis l'époque de Coulomb (1800) dans la science des frottements, connue sous le nom de tribologie, il reste encore de nombreux phénomènes à expliquer. Il faut souligner que, au sein du département chargé des performances des avions, nous n'avons pas les moyens de mener des études approfondies sur le frottement du caoutchouc. Nous nous appuyons donc sur les travaux d'institutions externes et sur une bibliographie exhaustive pour acquérir une connaissance fondamentale de ce phénomène. Le domaine couvert par la tribologie est vaste et de nombreuses thèses ont été entièrement consacrées à l'étude du glissement du caoutchouc sur une surface dure. Dans le cadre de ce travail, une étude a été menée sur les recherches et les découvertes les plus récentes en tribologie pour identifier les principes qui gouvernent le frottement entre le pneu et la surface. Le coefficient de frottement statique est mesuré au moment où un objet sur une surface cesse d'être immobile et où le glissement entre les deux surfaces se produit. Cependant, en réalité, ce moment très bref est difficile à mesurer et il existe peu d'informations pour quantifier cette valeur, même dans la littérature. De plus, il a été démontré que le coefficient de frottement statique est un facteur du temps de repos. Autrement dit, en conditions de laboratoire, plus le bloc de caoutchouc reste longtemps en repos sur la surface, plus la liaison entre le caoutchouc et la surface augmente et plus le coefficient de frottement statique augmente quand le bloc est déplacé. Persson [17] cite quatre différents mécanismes pouvant entraîner une augmentation du coefficient de frottement statique quand le temps passé à l'arrêt augmente.

1. Formation de ponts capillaires dans une atmosphère humide

2. Augmentation de la zone de contact en raison d'une déformation plas-

tique dépendante du temps (activation par la chaleur)

3. Inter-diffusion des chaînes de polymères

4. Relaxation de la contrainte de cisaillement à l'interface

Cependant, si nous appliquons le modèle de la brosse aux applications de roulage des pneus, le temps écoulé entre le moment où un poil entre dans la zone de contact et le moment où se produit la transition entre le repos et le glissement est presque instantané. Le temps de repos est donc nul. Ainsi, pour modéliser le coefficient de frottement statique, nous prendrons le coefficient de frottement statique égal au coefficient de frottement dynamique à basses vitesses et basses températures. Nous pouvons décomposer le frottement dynamique en deux effets principaux :

1. Forces d'adhérence

2. Forces viscoélastiques dans le caoutchouc

Les forces d'adhérence sont associées aux forces de Van der Waals, autrement dit à l'attraction moléculaire entre deux matériaux en contact (dans ce cas, le caoutchouc et l'asphalte). Ces forces d'adhérence sont, dans le cas du frottement caoutchouc-asphalte, beaucoup plus faibles que les forces viscoélastiques, de l'ordre de quelques pourcents. Les forces d'adhérence jouent un rôle plus important lorsque sont impliquées des surfaces propres et lisses comme le verre. Les forces viscoélastiques dominent les forces de frottement. Ces forces proviennent de l'excitation du caoutchouc quand il traverse les aspérités de surface à la fréquence ω_o. Cette excitation dissipe l'énergie due à la nature viscoélastique du caoutchouc et cette dissipation de l'énergie est à l'origine de la force de frottement. Les recherches portant sur les facteurs modifiant le coefficient de frottement ont été menées en partenariat avec l'Institut de dynamique et de vibrations (IDS) de l'université Leibniz de Hanovre, Allemagne. Cet Institut bénéficie d'une large expérience dans la modélisation, la simulation et les tests du contact de frottement. L'IDS a reçu deux pneus à tester. La grille des tests est mentionnée au tableau 6.1. La procédure consistait à faire glisser des échantillons de caoutchouc sur une piste d'essai. L'essai comprenait une phase d'accélération jusqu'à une vitesse stable et une décélération rapide. Les principaux paramètres mesurés ont été la charge verticale sur l'échantillon, la vitesse et la force de frottement. Plusieurs essais ont été pratiqués sur chaque échantillon jusqu'à l'obtention d'une force de frottement stable. Finalement, un coefficient de frottement moyen a été obtenu pour chaque point de la grille de test. Cette recherche en tribologie a confirmé la complexité inhérente à la modélisation du glissement entre le caoutchouc et une surface dure. Nous avons identifié trois caractéristiques principales qui doivent être connues pour pouvoir quantifier le coefficient de frottement.

1. Les caractéristiques mécaniques du caoutchouc, en fonction du temps et de la fréquence, $G(\omega, t)$

2. La texture macroscopique de la surface h/l

3. Les propriétés thermiques du caoutchouc $G(T)$

Une fois ces trois caractéristiques connues, les modèles de Persson nous ont permis de quantifier le coefficient de frottement par glissement en conditions sèches. Les résultats expérimentaux obtenus à partir des tests de frottement par glissement permettent de valider la modélisation du frottement. En raison des contraintes de délais de cette thèse, la procédure de validation fera l'objet de travaux futurs au cours desquels les modèles de frottement de Persson seront comparés aux données obtenues à l'Université de Hanovre. Une fois les modèles de frottement validés, ils pourront être directement entrés dans le modèle de la brosse.

Pour la partie III de cette thèse, la validation du modèle de la brosse, nous n'utiliserons pas les modèles de frottement proposés par Persson dans le modèle, mais nous utiliserons les résultats expérimentaux de l'Université de Hanovre.

Coulomb's Law, $F_x = \mu F_z$, says that the force resisting movement, F_x, (or friction force) of a block is proportional to the vertical force F_z. The coefficient of proportionality is called the coefficient of friction and in most often symbolized by the Greek symbol μ (mu). In general we consider that the coefficient of friction is constant. Since Coulomb's time (1800), significant progress has been made into the study of friction, known as the science of Tribology, although there stills rests a number of phenomena to explain.

It should be noted that within the aircraft performance department we do not have the means with which to make in depth studies of rubber friction. As such we have relied heavily on the help of outside institutions as well as an extensive bibliography to obtain a fundamental understanding of friction. The domain of tribology is large and entire thesis' have been devoted to the study of rubber sliding on a hard surface. In the framework of this thesis work, a study has been made of the most recent research and advances in tribology to identify the principle effects that govern tire-surface friction. The results of this study are summarized below.

Goal   *The goal of this chapter is to develop the models to determine μ_{sx} and μ_{kx} for use in the derived form of the Brush Model (Pg 50) as developed in Chapter 2.*

6.1   Introduction

Friction is generally explained using the simple case of a rectangular block element placed on a horizontal surface. A vertical load, F_z, is placed on top of the rectangular element and a horizontal force, starting at zero and steadily increasing, is applied to the element. The force at which the
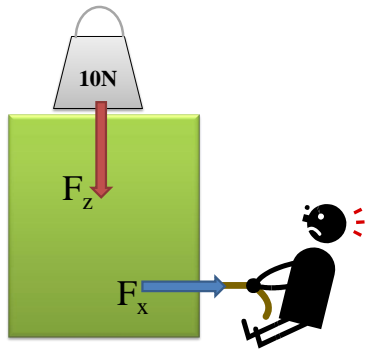
Figure 6.1: Schematic of Basic Friction Test

rectangular element begins to move is measured as F_{x_s} and the force needed to maintain a prescribed velocity, F_{x_k} is also measured. From these two forces we can define the static and dynamic coefficients of friction as follows

$$\mu_s = F_{x_s}/F_z$$

$$\mu_k = F_{x_k}/F_z$$

The principal properties governing friction were studied during the 18th and 19th century by Amontons, Coulomb and Euler. From this period three general laws of dry friction (friction between two surfaces without lubrication) were formulated.

$1^{st} Law$ - the force of friction, F_x, is directly proportional to the vertical load, F_z

$2^{nd} Law$ the force of friction, F_x, is independent of the apparent area of contact

$3^{rd} Law$ kinetic friction is independent of the sliding velocity, v_s

—

Although in certain conditions these laws still hold true, we will find that in the case of rubber friction, notably when rubber is sliding against a rough hard surface, there are deviations to the above laws that must be taken into account.

6.2 Qualitative Discussion

6.2.1 Coefficient of Friction as a Function of Vertical Load

The first law of friction states that the force of friction is directly proportional to the vertical load. Put in another way, the coefficient of friction, μ is independent of the vertical load. It was not until the 1950's that this phenomena began to be understood and in fact it was not until 1966 that

the term tribology - the science and technology of interacting surfaces in relative motion, was first used[7]. Friction began to be studied at the microscopic level, the interaction between the asperities of the two surfaces. As mentioned previously, when viewed microscopically, the surface texture of a surface such as asphalt resembles a mountain range, with large peaks and valleys. When two elements are in contact with each other, such as rubber and asphalt, the rubber is in fact resting on the peaks of these mountains i.e. the peaks of the asperities. This concept gave way to the notion of *real area of contact* as developed in Section 4.4. Real area of contact refers to the fact that the rubber is only in contact with the peaks of these asperities, thus the total surface area where there is direct contact between the rubber and the asphalt is significantly less than the apparent area of contact (See Section 4.1). *It was observed that under particular conditions the friction force was proportional to the real area of contact and that the real area of contact was proportional to the vertical load [1]. This was indeed a verification of the 1st law of friction, that frictional force was proportional to the vertical load.* However, this law does not always hold true, particularly for rubber-rough surface sliding under heavy loading. Under light loading, as the vertical load is increased the real area of contact does indeed increase proportionally to the vertical load. **However, as the rubber becomes heavily loaded the valleys between the asperities begin to become filled. Consequently, as the vertical load increases, the valleys between the asperities become saturated and the real area of contact is no longer proportional to the vertical load.**

This is the case for aircraft tires where the contact pressure is extremely elevated compared to simple rubber sliding applications. Aircraft tires may be loaded up to 30 tons per wheel, with an contact pressure exceeding $25Bar$. **For this reason, in aircraft tire applications we find that the coefficient of friction decreases with increasing vertical load.**
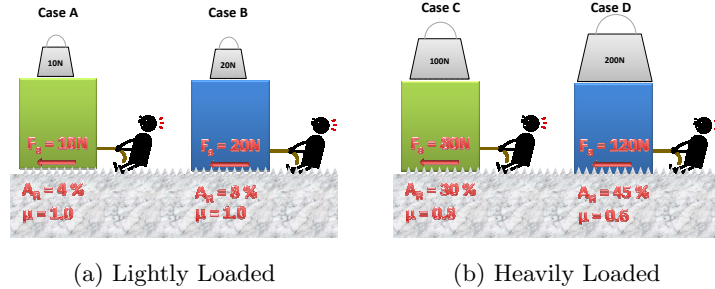
| (a) Lightly Loaded | (b) Heavily Loaded |

Figure 6.2: Schematic of the relationship between real area of contact, vertical load and friction force. Case A and B represent lightly loaded conditions where Coulomb's law applies. Case C and D represent heavily loaded conditions where Coulomb's law now longer applies.

Example 3. *We use an example to illustrate this concept (Figure 6.2). The numbers are fabricated to give an understanding of the process and do not represent real values.*

For Case A and B, the rubber blocks are lightly loaded. For Case A when $10N$ of vertical load are applied, the real area of contact, A_r, is 4% and the F_s is $10N$ giving a μ of 1.0. In Case B, if we double the applied load, A_r, doubles and since F_s is proportional to the real area of contact, it also doubles so that μ remains at 1.0. This is an example where Coulomb's law still applies. The sliding friction is proportional to the vertical load because the real area of contact is proportional to the vertical load.

Case C and D are examples of heavily loaded rubber. In Case C the vertical load is now $100N$. The cavities between the asperities are much more filled and we find a A_r of 30%, leading to a F_s of $80N$ and a μ of 0.8. If we double the vertical load to $200N$ such as in Case D we note that the valleys continues to be filled, but that it is no longer proportional. The A_r is no longer proportional to the F_z, however the friction force is still proportional to the real area of contact. Thus we find a F_s of $120N$ and a corresponding μ of 0.6. Thus we can see that for the heavily loaded applications in Case C and D, Coulomb's law no longer applies. The friction force is not proportional to the vertical load.

6.2.2 Coefficient of Friction as a Function of Sliding Speed

The third law of friction states that kinetic friction is independent of the sliding speed. However for rubber sliding on a rough surface this law does not generally hold true due to the effects of temperature and solicitation frequency. The section Material Science (3) demonstrated that rubber's mechanical properties change as a function of frequency and temperature due to the viscoelastic effects. When rubber is sliding on a rough surface, the asperities generate a solicitation frequency in the rubber. This solicitation frequency has the effect of increasing the mechanical strength (shear modulus and Young's modulus). This increase in stiffness results in the tire sinking less into the surface asperities for a given vertical load, thus decreasing the real area of contact and consequently the friction force. Inversely, as the rubber experiences prolonged sliding, the temperature of the rubber increases due to the frictional forces generating heat. Material Science demonstrated that as the temperature increases, rubber experiences a decrease in mechanical strength which, by the same mechanism as above, results in an increase in the frictional force.

To summarize, if temperature effects were not taken into account, an increase of velocity would result in a decrease in the coefficient of sliding friction due to the solicitation frequency effects. However due to the associated temperature rise in the rubber due to friction, this effect is partially neutralized. Consequently, in real world conditions, the effect of velocity on the coefficient of friction is often small due to these two competing effects.

6.3 Static Coefficient of Friction

The coefficient of static friction is measured at the moment that rest is broken and sliding between two surfaces is established. However in reality, this extremely brief moment in time is difficult to measure and as such, even in literature, very little information exists to quantify this value. In addition we have a second problem in that the static coefficient of friction has been shown to be a factor of resting time. That it to say that under laboratory conditions, the longer a rubber block is allowed to remain at rest in contact with the surface, the adhesive bond between the rubber and the surface increases, thus increasing the static coefficient of friction when the block is eventually moved from rest. Persson [17] cites four different mechanisms that may cause the static coefficient of friction to increase with stationary time

1. Formation of capillary bridges in a humid atmosphere

2. Increase in the contact area due to time dependent (thermally activated) plastic flow

3. Chain inter-diffusion for polymers

4. Shear stress relaxation at the interface

However in tire-rolling applications, if we take the brush model theory, the time from when a bristle enters the contact zone, to the point where the transition between stick and slip occurs, ranges from zero (in the case of pure slip) to a maximum value of the length of the contact area divided by the rolling speed of the wheel e.g. $0.4m$ divided by $50m/s = 0.008s$. The resting time needed to develop adhesive friction bonds is virtually non-existent in tire-rolling applications.

Despite the fact that the static friction itself is difficult to measure, we see the effects of the static coefficient of friction from test data in tire-rolling conditions. Chapter 2.5 shows the effect that changing the value of the static coefficient of friction has on the shape of the $\mu - slip$ curve. If the static μ is equal to the dynamic μ then the $\mu - slip$ curve has no peak, it becomes a flat line at $\mu_{max} = \mu_{sx} = \mu_{kx}$. **However braking test results show conclusively that the $\mu - slip$ curve has a peak with the friction coefficient diminishing on the unstable (right) side of the curve, clearly indicating that there is a difference between the dynamic and static μ.**

The test equipment at IDS for sliding friction samples data at $30,000Hz$. Thus during the dynamic friction testing, we were able to extract some basic results regarding the static coefficient of friction. Figure 6.3 shows the results from the four test runs measuring the coefficient of friction. We see as predicted by the Chapter 3 that the coefficient of friction, both static and dynamic, are a function of the contact pressure. The test results show a clear peak representing the static coefficient of friction.

Remark 4. *From Figure 6.3, this peak seems to be independent of the steady-state velocity. This agrees with theory since, by definition, static friction is the force needed to break the bonds between two non-moving surfaces.*

However, the data from Figure 6.3 involved a significant resting time and as a result the static friction measured is not applicable to the case of a braking tire where the resting time is negligible. IDS performed further tests to quantify the effect of resting time as shown in Figure 6.4. These tests show the strong impact of resting time on the static coefficient of friction. Nevertheless, it is problematic to measure resting times in the millisecond range as would be necessary to represent a braking tire. Neither is there a clear methodology with which to extrapolate the data to millisecond resting times. Based on the preceding analysis, there is no clear way forward to model the static coefficient of friction to be used in the brush model.

Persson has shown in [17] that for practical applications, such as a tire braking, the static coefficient of friction can be approximated as being equal to the dynamic coefficient of friction at low velocities. Persson showed that for rubber sliding at low velocities ($v = 3.3 \times 10^{-4}m/s$)on a hard surface, with
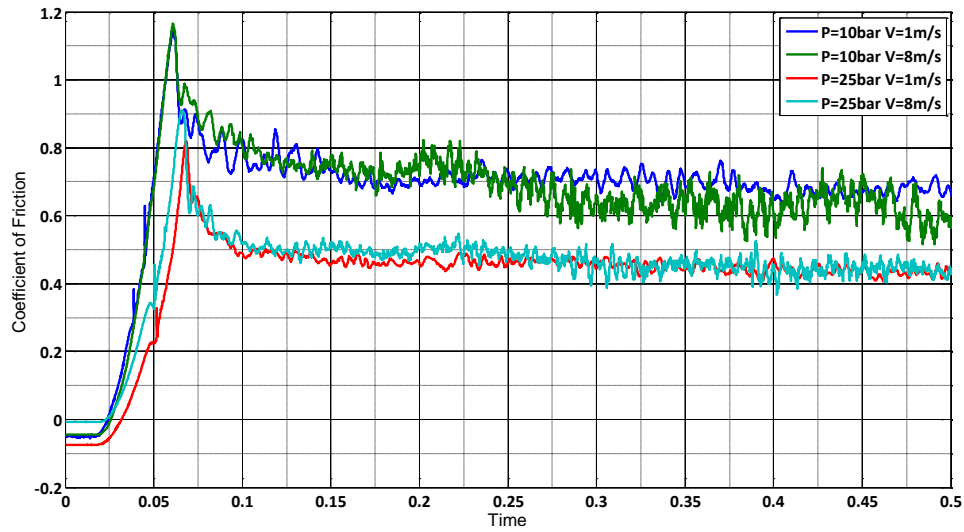
Figure 6.3: Coefficient of friction testing of the rubber found in an aviation tire tread. Measured at 30,000Hz permits the static coefficient of friction to be determined.

no resting time to develop molecular bonds, there was no peak which in the friction vs time curve which would define the static coefficient of friction.

This presents the best way forward for integration into the brush model. We will equate the μ_{sx} to the μ_{kx} determined experimentally by IDS at low sliding velocities. This approach will be discussed further in the Chapter on Brush Model Validation. However it should be noted that the definition of *low-speeds* are significantly different between IDS and Persson's experimentation e.g. Sliding speed of $1m/s$ for IDS and $3.3 \times 10^{-4} m/s$ for Persson.
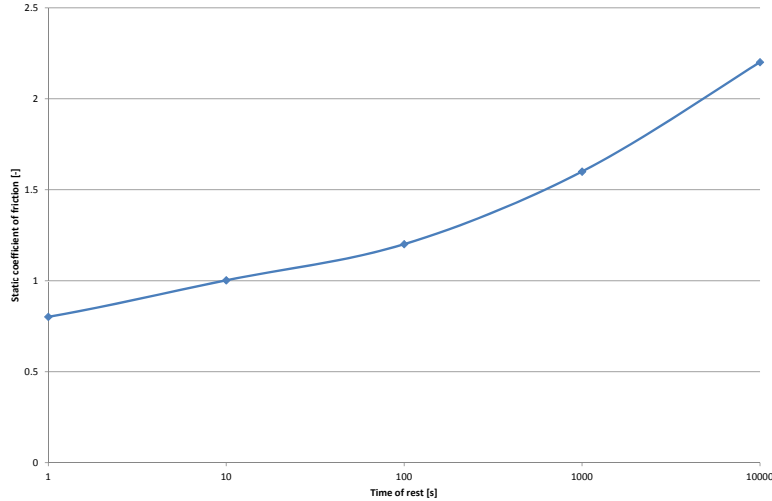
Figure 6.4: Static coefficient of friction as a function of resting time

6.4 Dynamic Coefficient of Friction

The literature is appreciably richer concerning the dynamic coefficient of friction, μ_k, as opposed to the static coefficient of friction, μ_s. This is almost certainly due to the relative ease in measuring the dynamic coefficient of friction from experimental tests. To determine the dynamic coefficient of friction for rubber on a hard surface, one simply needs to move the rubber sample across the hard surface at a fixed velocity and a constant vertical load while measuring the horizontal force needed to keep the block at a constant velocity. The coefficient of friction is found from $\mu_k = F_{x_k}/F_z$. This simple test procedure facilitates a clearer understanding of the factors affecting dynamic friction as external parameters such as vertical load, velocity, temperature, rubber type, runway texture are easily varied and their effect on μ_k identified. Section 6.6 will explore these effects through experimental results. The sections that follow will give a brief overview of the literature and the modeling of the dynamic coefficient of friction. For a much deeper understanding of tribolgy, the writer refers you to the pioneering works made by Grosch [5] and the extensive work done by Persson in the last 15 years [14][15][16][18][19].

In general we can break down the dynamic friction into two principal effects
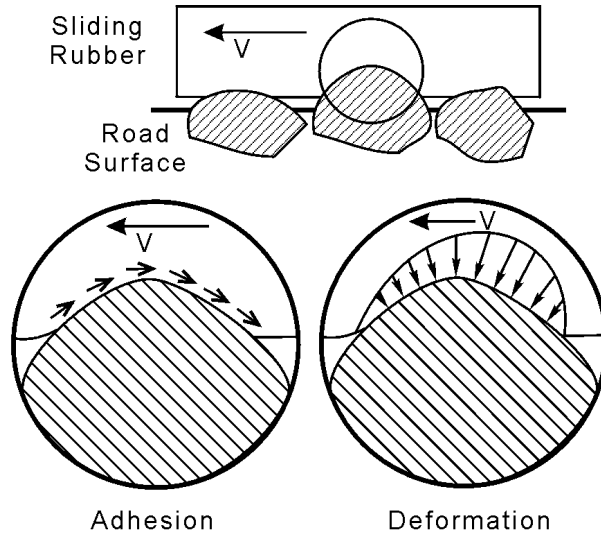
1. Forces due to adhesion

Figure 6.5: Two major effects identified for rubber-rough surface friction: adhesive forces and viscoelastic forces. Taken from

2. Viscoelastic forces in the rubber

Figure 6.5 attempts to visualizing these two principal effects. As we can see, the adhesive friction is generated from surface to surface contact between the two surfaces via the Van der Waals forces whereas the viscoelastic friction (or hysteresis) is an internal friction generated by the deformation of the rubber.

6.4.1 Adhesion Forces

The adhesion forces are associated with the Van der Waals forces i.e. the molecular attraction between two materials in contact (in this case the rubber and the asphalt). These forces of adhesion are, in the case of rubber-asphalt friction, much smaller compared to the viscoelastic forces, on the order of a couple percent. The adhesive forces play a more important role when dealing with clean, smooth surfaces such as glass.

Persson [20] proposes a formula that is valid if the rubber is sufficiently loaded that it fills all of the asperities i.e. in practice if the height of the asperities is less than $1000 Angstrom = 10^{-7} m$.

$$\mu_{ka} = -\frac{S}{F_z} \left(\frac{h}{\lambda}\right)^2 G''(\omega_o) \tag{6.1}$$

Where S is the surface of contact, F_z is the vertical load on the block, h is the height of the asperities, l is the horizontal distance between the

peaks of the asperities (in general $h/l = 1$) and G is the shear modulus of the rubber in function of the solicitation frequency ω_0. The solicitation frequency can be modeled by the velocity at which the rubber encounters the peaks of the asperities $\omega_o = vl$. G'' is the loss modulus (imaginary part of the shear modulus) which corresponds to the viscoelastic part of G (See Section 3.2.5).

Although the adhesive forces are small in comparison with the viscoelastic forces, they can still play an important role in establishing the viscoelastic forces due to the real area of contact. We note the relationship between the real area of contact and the adhesive forces; the bigger the real area of contact is under small loads, the bigger the adhesive forces will be. [20](p.87).

6.4.2   Viscoelastic Forces

The viscoelastic forces dominate the forces of friction. These forces come from the excitation of the rubber as it transverses the asperities of the surface with a frequency ω_o. This excitation dissipates energy due to the viscoelastic nature of the rubber and it is this dissipation of energy which is at the origin of the friction force. Persson [13][14] gives an analytical expression for the viscoelastic friction μ_{kv}

$$\mu_{kv} = -C\frac{E''(\omega_o)}{E'(\omega_o)} \tag{6.2}$$

where

$$\omega = v/l$$

$$C = (\delta/R)^{1/2} \approx 1$$

Where δ is the average value (rms) of the height of the asperities and R is the radius of the asperities. In general for runways and roads we consider that the ratio $\delta \approx R$ thus $C \approx 1$. As before, v is the sliding velocity and l is the horizontal distance between the peaks of the asperities. To give an example, for gravel the maximum size of the asperities l_o is on the order of a couple mm and the minimum size l_1 is around $0.03mm$. Chapter 3 developed the notion of the loss modulus (E'') and the storage modulus (E') as applicable to both the Young's Modulus, E, and the shear modulus, G. These dynamic moduli play an important role in the development of the viscoelastic forces. We recognize that the more viscous (larger phase lag ϕ and thus larger loss modulus E'') a material is, the larger the viscoelastic frictional forces will be. Thus the viscoelastic frictional forces are proportional to E''.

Maximum Viscoelastic Coefficient of Friction   Equation 6.2 for the viscoelastic friction has a maximum value when

$$\omega_o = 1/\tau$$

where

$$\tau = \exp^{\delta E/kBT}$$

τ is a relaxation time, but is also the *Boltzmann factor*. δE is the energetic transition barrier, kB is the Boltzmann constant $1.38 \times 10^{-23} J/K$ (SI) and T is the temperature in Kelvin.

Parameters affecting the viscoelastic friction

1. Type of rubber which determines the δE and thus the relaxation time τ as well as the excitation frequency which gives the maximum friction.

2. The temperature which affects the value of τ and thus has an influence in the same sense as number 1.

3. The size of the asperities l of the surface which determine the solicitation frequency $\omega = v/l$ for a give sliding velocity.

4. The sliding speed v which, for a given size of asperity, influences the solicitation frequency ω

Surface complexity The previous formulas are established for one size of asperity, however in reality a surface is composed of a number of different sized asperities. This surface can be modeled as fractal surface. Persson [14][15] gives some methods to take into account this complexity. In [15] the case of two different asperity sizes is treated where the larger asperity has an effective radius R_o and the smaller asperity has an effective radius R_1. For the larger asperity, there are $N1$ small asperities in contact with the rubber.

Hypothesis 1 - The rubber does not fill all of the cavities formed by the small asperities

$$\mu_{kv} = C_o \frac{E''(\omega_o)}{E'(\omega_o)} + C_1 \frac{E''(\omega_1)}{E'(\omega_1)} \tag{6.3}$$

with

$$C_o = \sigma_o/E(\omega_o) \approx 1$$

$$C_1 = \sigma_1/E(\omega_1)$$

The concentration of the small asperities $n = N1/A_o = 1/a^2$. The contact surface around the larger asperity is A_o. $nu = 0.5$.

Hypothesis 2 - The rubber fills all of the cavities formed by the small asperities

This is the most likely of the two cases. An automobile tire sliding with a minimal sliding velocity is in contact with only approximately 5% of the

large asperities, but the contact pressure is sufficient that the rubber fills all of the small asperities. In this case

$$\mu_{kv} = C_o \frac{E''(\omega_o)}{E'(\omega_o)} + C_1 \frac{E''(\omega_1)}{E'(\omega_1)} \tag{6.4}$$

with

$$C_o = \sigma_o / E(\omega_o) \approx 1$$

$$C_1 = \sigma_1 / E(\omega_1) = \frac{1}{C_o} \frac{h^2}{\lambda} \frac{E(\omega_o)}{E(\omega_1)}$$

where h and λ are the height and length of the large asperities. In general we can assume that $h/\lambda \approx 1$.

This result can be generalized for several size of asperities, but in addition, it can be generalized for the fractal surfaces *self-affine* as shown by Persson [15][12].

Persson [15] gives some important information with regards to the different sizes of asperities. If the rubber fills all of the cavities of the asperities, then μ_{kv} no longer depends on the height and length of the asperities. What is interesting to note is that even *rough* surfaces with larger asperities will give the same values for the viscoelastic friction if the ratio of h/λ is the same. This is often the case since h/λ often is equal to 1.

However, the roughness of the surface will contribute to μ_{kv} as a function of the velocity. Recall that $v = \lambda\omega$ and that the sliding speed defines the maximum of μ_{kv} when $v/\lambda = 1/\tau$. This fundamental results tells us that we must take into account the roughness of the surface (width of the asperities λ) in the calculation of μ_{kv}.

If we take an example of a surface with two different sizes of asperities [15](fig.2 p.3841) we make the assumption that the vertical force on the rubber is sufficient that the rubber fills the entirety of the grand cavity. We note that the contact pressure at the peaks of the large asperity is higher that in the valley of the cavity. Thus, concerning the small cavities located in the valley of the larger asperity, the contact pressure may not be sufficient for the rubber to fill these small cavities. Thus the participation of these small cavities in the viscoelastic frictional forces may be lost.

6.4.3 Additional Viscoelastic Forces

Heinrich [6] has also modeled the viscoelastic forces which provide some additional information to the work by Persson. He describes these forces as being an dissipation energy due the deformation of the tread. This can also be though of as hysteresis. Heinrich mentions that these forces are generally not taken into account in the literature and he gives a general formula to calculate these forces.

$$\mu_{kvd} = \mu_{kv}^2 \pi \sigma_o \frac{h}{L} \frac{G''(\omega, \epsilon, T)}{G'(\omega, \epsilon, T)}^2 \qquad (6.5)$$

where h is the thickness of the tire-tread, L is the length of the tire-tread contact zone, $\sigma_o = F_z/S$ is the average contact pressure (F_z is the vertical load and S is the apparent area of the tire-surface contact zone) and ϵ is the horizontal elongation of the tread. We note that the shear modulus G is a function of ω, ϵ and the temperature T as demonstrated in the chapter Material Science (3).

In effect, these additional forces represent the part of the spring energy (Hooke's Law) that is lost due to the viscoelastic nature of the rubber. In general these additional forces are small, on the order of 3% of the total viscoelastic forces. $\mu_{kvd} = 0.03 \mu kv$.

6.5 $\quad \mu_{hot}$ - μ_{cold} Theory by Persson

As has been outlined in the previous sections, the modeling of tire rubber sliding on a hard rough surface is complex. In additions, the complexity of the models adds to the computational cost which can pose a problem to implement the complete Brush Model theory in real-time simulations. It is for this reason that the latest simplified model proposed by Persson could prove to be very interesting for future development of the Brush Model. Due to the fact that the article describing Persson's new theory was published at the end of 2010, it was not possible to apply this model to the current work and validate with flight test data. Here we will briefly outline the model as a recommendation for future work on the Brush Model.

The model is presented as a *Phenomenological Rubber Friction Law* in [11]. The theories that Persson has developed model the affect of temperature that is generated a the rubber is sliding. As has been shown above, a cold rubber block experiences higher friction coefficients than a hot rubber block due to the viscoelastic properties of rubber. However as a block is sliding, this mechanical dissipation of energy generates heat within the rubber. Thus the longer distance that a block slides, the more heat generated and consequently the μ that the rubber experiences goes from being a μ_{cold} to being a μ_{hot}. **Persson has demonstrated that this sliding distance necessary to generate heat is surprisingly small. If the sliding distance is greater than the diameter of the asperities, D (on the order of $1cm$), then the friction experiences by the rubber is that of μ_{hot}.** Thus when the slip distance $r(t) << D$ then the $\mu(t) \approx \mu_{cold}(v(t))$ and for sliding distances $r(t) > D$ then $\mu(t) \approx \mu_{hot}(v(t))$. These can be combined to give a history dependent friction law

$$\mu(t) = \mu_{cold}(v(t), T_0)e^{-r(t)/r_0} + \mu_{hot}(v(t), T_0)[1 - e^{-r(t)/r_0}] \qquad (6.6)$$

where T_0 is the background temperature and $r_0 \approx 0.2D$. We can determine the functions $\mu_{cold}(v(t), T_0)$ and $\mu_{hot}(v(t), T_0)$ either through experimental data or by following Persson's full theory as presented in several of his articles.

The μ_{hot} - μ_{cold} effect seems analogous to the dynamic and static coefficients of friction without resting time. We have described in Section 6.3 and shown in Figure 6.4 that the static coefficient is related to the resting time, but that in tire-sliding applications the rest time is practically zero. Thus the small difference that is measured in experimental data between the μ_s and the μ_k is in fact the instantaneous heating effect as described by Persson's theory.

This theory gives a way forward to take into account the time-temperature effect of rubber sliding on a rubber surface. The basic brush model as developed in Chapter 2 assumed a constant μ_k all along the contact area. Using this hot-cold friction law permits for a μ which changes not only with the length of the contact area, but also the slip ratio, which defines how much of the contact zone is in sliding.

6.6 Experimental Data for the Dynamic Coefficient of Friction

The research into the factors affecting the coefficient of friction was done in partnership with the Institute of Dynamics and Vibration Research (IDS) at the University of Hannover in Germany. The institute has extensive experience in modeling, simulating and testing friction contact.

6.6.1 Experimental Setup

The goal of the study was to determine the sliding coefficient of friction as a function of four main parameters:
  – T_{amb} - ambient air temperature
  – V_s - sliding velocity
  – P - contact pressure
  – Runway properties including texture and contamination

IDS was given two tires, Tire A and Tire B with which to perform tests on. The test grid is shown in Table 6.1. The test procedure involved sliding rubber specimens on a test track. This involved an acceleration phase until a stable velocity was reached and a rapid deceleration. The principal parameters measured were the vertical load on the specimen, the velocity and the friction force. Several tests were performed on each specimen until a stabilized friction force was obtained. The end result was one mean coefficient of friction for each point on the test grid.

Table 6.1: Test grid for sliding friction testing of aircraft tires.

Tire Type	Tamb (° C)	P (bar)	V (m/s)	Runway
Tire A	-20	10	1	Highway - Dry
Tire B	0	15	4	Highway - Wet
	20	20	8	Runway
	40	25	12	
			15	

6.6.2 Results

A subset of the results will be given here and analyzed. Figure 6.6 shows a summary of the results obtained from the friction testing for one tire on a dry runway.
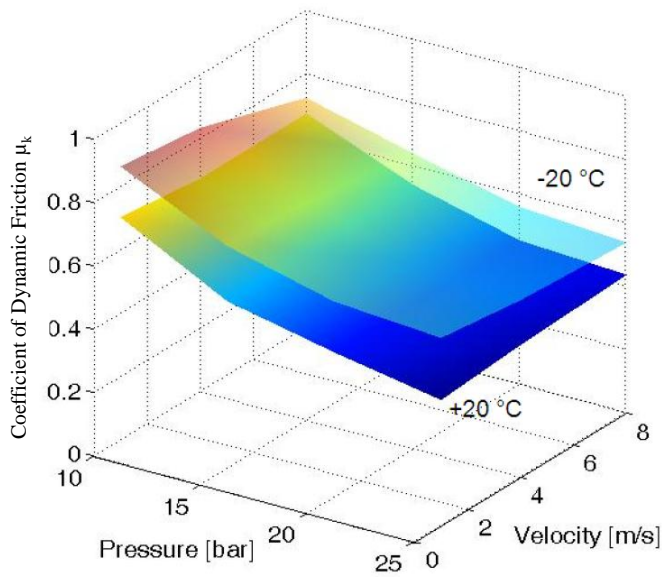

Figure 6.6: Summary of results for one tire on a dry runway giving coefficient of dynamic friction as a function of ambient temperature, contact pressure and velocity.

Coefficient of Friction as a Function of Contact Pressure The principal conclusions we can make from Figure 6.6 is that there is a strong effect of the contact pressure. As the contact pressure increases there is a decrease in the coefficient of friction. This corresponds well with the qualitative discussion from Section 6.2.1 which identified that heavily loaded applications

no longer follow the 1st law of friction. We recall that this is due to the asperity valleys becoming filled and consequently the real area of contact is no proportional to the vertical load. Aircraft tires qualify as a *heavily loaded* application due to the high contact pressures of aircraft tires ($> 18bar$). Thus the experimental results obtained verify the theory that the coefficient of friction is dependent on the contact pressure.

Coefficient of Friction as a Function of Ambient Temperature   The results from IDS also show the strong temperature effect on the coefficient of friction. From Figure 6.6 we see that the lower the temperature, the lower the coefficient of sliding friction. This effect can be explained by the fact that for the rubber used in aircraft tires, the friction is principally due to the viscoelastic effect as described in Section 6.4.2. The viscoelastic friction is proportional to the loss modulus, G''. From the Chapter on Material Science (3) we know that as rubber gets colder, the mechanical strength increases as the rubber is approaching its glass transition temperature, T_g. Thus the phenomena shown during experimental testing represents that predicted by Material Science and Tribology.

Coefficient of Friction as a Function of Sliding Speed   The results show that the sliding velocity has very little effect on the sliding coefficient of friction. Upon first glance, this result seems incoherent with the effects predicted by Material Science. We recall that we have previously demonstrated that the solicitation frequency, ω, is proportional to the sliding speed, v_s and that the loss modulus G' increases with solicitation frequency (in the frequency range normally encountered by tire sliding). From our viscoelastic friction equations, the friction coefficient is proportional to the loss modulus, consequently for higher sliding speeds we expect the friction coefficient to increase.

However this does not take into account the thermal effects of the rubber i.e. the fact that the mechanical dissipation of energy generates heat which is absorbed by the rubber. For higher sliding velocities, the solicitation frequency dissipates more energy which is absorbed by the rubber which raises the temperature of the rubber. Due to the fact that the experimental results show that there is very little effect due to sliding velocity we assume that the two opposing effects –decrease of G' due to increased temperature and increase of G' due to sliding speed– are approximately equivalent.

We represent this effect schematically in Figure 6.7 which gives the loss modulus as a function of solicitation frequency and temperature. We see that for four different velocities, the solicitation frequency is different, but due to the temperature effect, the loss modulus experienced remains more-or-less the same.
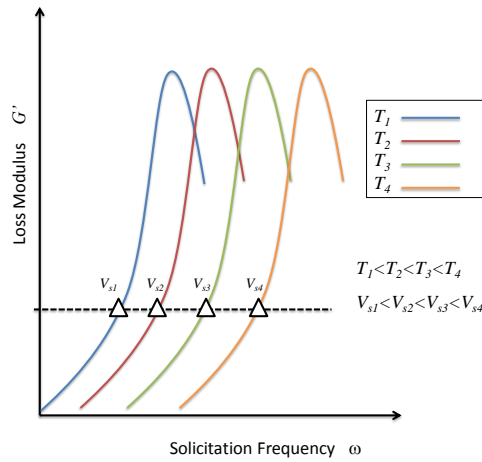
Figure 6.7: Velocity-Temperature effect. At higher velocities, the rubber temperature increases. Thus the net result is that the loss modulus remains the same.

Effect of Different Pavement Types Two different test surfaces composed of two pavement types were tested to determine the effect that pavement type as on rubber sliding friction. The first of these test surfaces, *Surface 1*, was constructed in a manner consistent with pavement used on German auto-routes. The second test surface, *Surface 2*, was constructed using stone type and composition consistent to an airport runway.

The majority of the friction tests were performed on *Surface 1* while several tests were performed on *Surface 2* to determine the variation of the friction coefficient due to the runway surface. The results showed that the friction coefficient between the two surfaces did not vary significantly between the two surfaces. Results were generally within 10% with no clear tendence for one surface over the other.

From this result we conclude that the macro texture between a highway developed for cars and a runway constructed for aircraft are not appreciably different in terms of their effect on friction. In addition, the majority of airports are constructed using standard construction techniques to ensure consistent friction for aircraft. **As a result, the experimental data obtained by IDS is applicable to aircraft landing on standard runways.**

However, there are several other runway construction techniques that may have an influence on friction. Some example of these runway types are: Porous Friction Course (PFC) runways used at some airports where heavy rain is frequent or grooved runways which are more commonly used in the United States. Future work of tire-modeling may try to take these other runway types into account. But for this work, we will ensure that any flight test data comes from an airport that has a standard runway construction.

Runway Contamination Effect on Friction Coefficient The tests performed at IDS also included tests on a wet runway. The level of water was no explicitly defined, however the water thickness was less than the asperities height so that there was no visible *standing-water*. However, the nature of the test setup is different than what a rolling tire would experience.

When a tire rolls on a wet-runway, the principal effect is that the rolling tire traps the water so that the water can not easily escape from the path of the tire. This trapping of water causes the tire to partially lose *real area of contact* and it is primarily this effect that causes lower friction on wet runways. The test setup by IDS uses a square sample that experiences pure sliding without any rolling effect. As such, the water is pushed away from the sample and the sample experiences nearly dry friction. Consequently, the wet runways friction coefficients are not directly applicable to the rolling/braking tire and as such will not be exploited here.

6.7 Conclusion and Way Forward

This research into tribology has confirmed the complexity inherent in modeling the sliding between rubber and a hard surface. We have identified three principal characteristics which must be known in order to quantify the friction coefficient.

1. the mechanical characteristics of the rubber both as a function of time and frequency, $G(\omega, t)$

2. the surface macroscopic texture, h/l

3. the thermal properties of the rubber $G(T)$

With these three characteristics known, the models by Persson allow us to quantify the sliding friction coefficient for dry conditions. The experimental results obtained from sliding friction tests permit to validate the friction modeling. Due to time constraints with the bounds of this PhD work, this validation procedure will be accomplished in future works. The future work will aim at comparing Persson's friction models with the data obtained from the University of Hannover. Once the friction models have been validated they can be used as direct inputs into the Brush Model.

For Part III of this PhD work, the Brush Model validation, we will not use the friction models as proposed by Persson in the Brush Model and instead will use the experimental results given by the University of Hannover.

Part III

Validation

Chapter 7

Flight Test Data Cleaning

Summary. Avant de pouvoir comparer les données des essais en vol au
modèle de la brosse, ces données doivent être prétraitées : correction des
erreurs, élimination du bruit et ajustement des valeurs erronées. Les avions
de série modernes enregistrent des milliers de paramètres en vol (et au sol) et
les avions d'essais en vol instrumentés en enregistrent beaucoup plus. Pour
cette étude, nous nous sommes limités aux avions d'essais en vol instru-
mentés car ils sont équipés de deux capteurs supplémentaires, indispensables
à cette analyse. Ces capteurs mesurent :

– $F_{z_{lg}}$ - La charge verticale mesurée sur le train d'atterrissage - N
– T_q - Le couple appliqué par les freins sur la roue - Nm

Nous avons utilisé deux autres paramètres (disponibles sur les avions d'essais
en vol et les avions de série) :

– v_x - La vitesse au sol des avions - m/s
– v_c - La vitesse tangentielle des pneus obtenue à partir de la vitesse de
rotation, ω - m/s

En utilisant la charge verticale connue qui s'exerce sur la fusée de roue, nous
calculons la taille de la zone de contact, a, à l'aide d'une donnée empirique
fournie par le fabricant des pneus qui relie la taille de la zone de contact,
$2a$, à la charge verticale sur la roue, F_z. Cette donnée empirique est fournie
à Airbus quand le fabricant livre ses pneus. Elle comporte les propriétés
mécaniques de base du pneu et les essais qualification pratiqués sur ce pneu.

Nous disposons maintenant de quatre variables, F_x, F_z, s et a, qui sont
directement mesurées et peuvent être entrées dans le modèle de la brosse. Il
reste trois variables supplémentaires pour compléter ce modèle : c_{px}, μ_{kx} et
μ_{sx}. Il n'existe actuellement aucune méthode précise et fiable pour obtenir
les variables c_{px}, μ_{kx} et μ_{sx} directement à partir des données des essais en
vol. Deux options permettent d'analyser ces variables :

– Estimation : à l'aide des théories scientifiques développées dans les
chapitres 3 à 6

– Identification : à l'aide de l'algorithme d'ajustement de courbe développé au chapitre 8

Cependant, avant de pouvoir effectuer l'identification du modèle de la brosse, il convient de vérifier et d'ajuster les données des essais en vol afin de s'assurer qu'elles fournissent des valeurs cohérentes. Ce chapitre donne un bref aperçu de ce procédé. Le couple et la charge verticale sont deux variables qui ne peuvent être obtenues que lors des vols d'essais, principalement parce que la mesure de ces variables pose des difficultés techniques et parce que de fréquents réétalonnages sont nécessaires pour assurer leur fiabilité. En conséquence, ces capteurs ne sont pas installés sur les avions de série. Ces deux variables sont sensibles au bruit qui doit être réduit au minimum dans les données avant de pouvoir les introduire dans le modèle de la brosse. Nous utilisons donc des filtres pour diminuer le bruit dans ces deux paramètres. Cependant, la nature du bruit est significativement différente entre les deux signaux. Les filtres doivent donc être ajustés séparément pour chaque paramètre afin d'obtenir le vrai signal derrière le bruit. Nous utilisons un filtre Savitzky-Golay (SG) qui est une technique de lissage des données sur la tendance passée et la tendance future du signal. Nous pouvons nous représenter le filtre SG comme un ajustement par morceaux d'une fonction polynomiale de ces données. Le filtre SG sera utilisé pour filtrer les mesures du couple et de la charge verticale. À cause de l'antidérapage, nous devons analyser ces données pour éliminer les points où ce système déclenche une réduction de la pression de freinage, ce qui entraîne une mise en rotation du pneu, c'est-à-dire une augmentation de la vitesse de la roue. Dans ces moments, les capteurs de couple mesurent les effets d'hystérésis qui ne sont pas pris en compte dans le modèle de la brosse. L'effet d'hystérésis est dû aux propriétés viscoélastiques du caoutchouc décrites au chapitre 3. Nous réutilisons une donnée indiquée au chapitre 3 pour la présenter Figure 7.9. Un matériau parfaitement élastique suivra le même tracé sur une courbe contrainte-déformation, que la contrainte soit appliquée ou relâchée. En revanche, un matériau viscoélastique suivra un tracé différent après la diminution de la contrainte, en raison de la perte d'énergie due au frottement à l'intérieur du matériau. Ce phénomène se nomme l'hystérésis. Un couple appliqué à la roue, puis relâché, a le même effet. Ainsi, les points de données mesurés après relâchement du couple de freinage seront situés significativement plus bas que les points mesurés lorsque le couple est appliqué. Ces points déforment la courbe $\mu - slip$ et interfèrent avec une identification correcte. Pour éliminer ces points, nous utilisons un procédé simple dont l'efficacité a été prouvée. Nous utilisons la dérivée de la vitesse circonférentielle, dv_c/dt, c'est-à-dire l'accélération de la roue. Nous éliminons tous les points où l'accélération de la roue est positive (mise en rotation). La Figure 7.10 ci-dessous donne un exemple de tracé de la vitesse de la roue avec élimination de tous les points d'hystérésis. Le chapitre suivant (8) présente la technique d'ajustement de la courbe utilisée pour identifier, à l'aide des données des essais en vol, les

paramètres du modèle de la brosse. Le chapitre (9) présente les résultats de cette technique d'ajustement.

Goal *The goal of this chapter is to pre-process the flight test data which may contain unwanted noise, false values and parameters which need adjustment. From flight test data, we will measure the braking force, F_x, the vertical load, F_z, and the slip ratio, σ_x. With these parameters obtained from flight testing, we can use the curve fitting algorithm, presented in Chapter 8-Identification, to determine the remaining three parameters, c_{px}, μ_{sx} and μ_{kx} as is presented in Chapter 9. This resolves all of the parameters contained within the Basic Brush Model derived in Chapter 2.*

7.1   Introduction

Before the flight test data can be compared to the Brush Model, the flight test data should be pre-processed to correct any errors, remove noise, and adjust false values. Modern serial aircraft record thousands of parameters during flight (and on ground) while instrumented flight test aircraft record significantly more. For this current study, we restrict ourselves to instrumented flight test aircraft as they contain two extra sensors that are fundamental to this analysis. These additional sensors measure

– $F_{z_{lg}}$ - Vertical load measured at the landing gear - N
– T_q - Torque applied by the brakes to the wheel - Nm

We use two additional parameters (available both on flight test aircraft and serial aircraft):

– v_x - ground speed of the aircraft - m/s
– v_c - the tangential speed of the tire(s) obtained from the rotational speed, ω - m/s

With these four variables, we have everything necessary to compare the braking force from flight test to the Brush Model. The mathematical computations are straightforward. To determine the braking force we divide the torque by the rolling radius, which itself is an estimated value

$$F_x = T_q/R_R \qquad (7.1)$$

The vertical load on each braked tire, F_z, is estimated based on the repartition of vertical load on the landing gear, $F_{z_{lg}}$, and the number of wheels on the landing gear, $n_{w_{lg}}$. The slip ratio, s, is computed using the ground speed and the wheel rotational speed

$$s_x = (v_x - v_c)/v_x \qquad (7.2)$$

or

$$\sigma_x = (v_x - v_c)/v_c \qquad (7.3)$$

Note the two definitions of slip ratio. The slip ratio of the form, s, is the value more commonly used in industry. It varies between 0 for a free-rolling wheel and 1 for a blocked wheel. The slip ratio of form, σ_x, is the ratio used in the derivation of the Brush Model. It varies from 0 for a free rolling wheel to ∞ for a blocked wheel. Although the Brush Model is derived with σ_x, the $\mu - slip$ curves that are plotted below use the form,s, in the x-axis as it holds more physical sense. The derivation of both slip ratios can be found in Section 2.2.3 pg 36.

Using the known vertical load acting on the tire axle, we compute the size of the contact patch, a, using an empirical data obtained from the tire manufacturer which relates the size of the contact patch, $2a$, to the vertical load on the wheel, F_z. This empirical data is supplied to Airbus when the tire manufacturer delivers a tire. It contains basic mechanical properties of the tire and the qualification tests performed on the tire.

We now have four variables, F_x, F_z, s and a, that are directly measured and can be used as inputs into the Brush Model. This leaves three additional variables to complete the Brush Model: c_{px}, μ_{kx} and μ_{sx}. There currently does not exist a precise, reliable method with which to obtain the variables c_{px}, μ_{kx} and μ_{sx} directly from flight test data. To analyze these variables there exists two options, the variables can be:

– **Estimated**: using the scientific theories developed in Chapters 3 through 6

– **Identified**: using the curve fitting algorithm that is developed in Chapter 8

Figure 7.1 provides a visualization of the link between the parameters from flight test and the Brush Model parameters.

However before Brush Model identification can be accomplished, the flight test data must be checked and adjusted to ensure they provide consistent values. This Chapter will give a brief overview of this process.
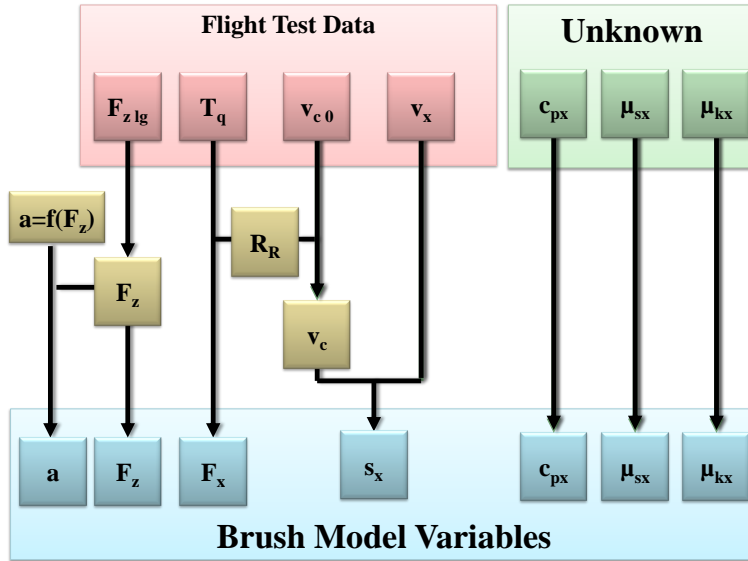
Figure 7.1: Schematic of the process to use flight test data to obtain the parameters needed for the Brush Model

7.2 Filtering Torque and Vertical Load

The torque and the vertical load are two variables that are available only on flight test aircraft. This is primarily due to the technical difficulty posed in measuring these variables and the frequent recalibration necessary to ensure reliability. Consequently, these sensors are not installed on serial aircraft. These two variables are subject to noise in the data which needs to be minimized before injection into the Brush Model.

As such, we use filters to minimize the noise from these two parameters. However, the nature of the noise is significantly different between the two signals. Thus the filter should be adjusted separately for each parameter in order to best capture the true signal behind the noise.

We use a Savitzky-Golay (SG) type filter, which is a data smoothing technique based on the past and future tendency of the signal. We can think of the SG filter as a piece-wise fitting of a polynomial function to the data. The SG filter has two primary inputs: the frame, F, and the order, O. The frame describes the number of data points to be used for the spline fit. The order determines the polynomial order of the spline that is fit through the data points.

As an example, at the position, x_i, we know the point $P(x_i)$. In this case we take an order, O, of 1 (linear fit) and a frame, F, of 5. To determine the new point, $P'(x_i)$, we make a second order least squares best fit, $f_1(x)$ of the interval $[x_i - 2 : x_i + 2]$. From this polynomial best fit, we determine the new point at x_i by $P'(x_i) = f1(x_i)$. This process is repeated for every
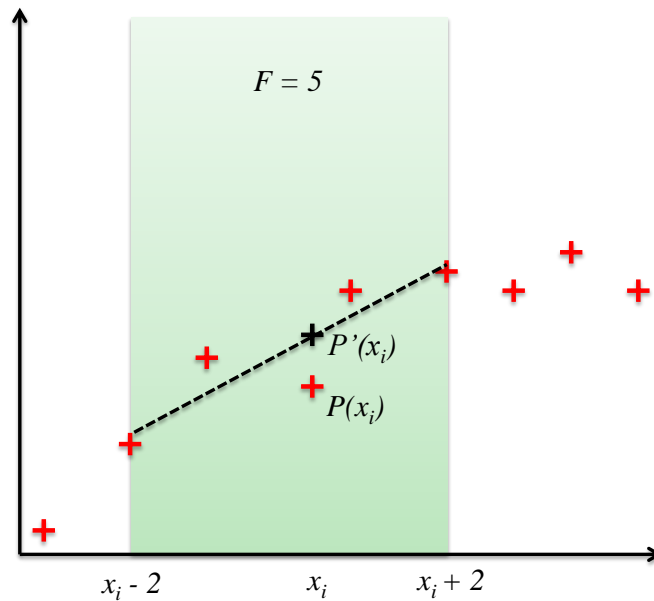
Figure 7.2: An example of Savitzky-Golay filtering using an Order of 1 (linear fit) and a Frame of 5.

point. An example of the Savitzky-Golay filter is shown in Figure 7.2.

7.2.1 Torque Filter

The torque data is subject to high frequency noise in the signal. However, the torque signal also contains large changes in values that are physically relevant and thus must be preserved. These large changes in value are due to the anti-skid system. When braking hard, the anti-skid system regulates the brake pressure by monitoring the wheel speed. If the anti-skid system detects that the wheel is *falling* into a skid, then the brake pressure is cut-off. This brake pressure cut-off results in a rapid decrease of the brake torque. Thus, it is normal to observe a high level of torque (as more brake pressure is applied) followed by a sharp decline of the torque value coinciding with the anti-skid system cutting the brake pressure.

Using the SG smoothing technique, it is advantageous to use a larger frame to eliminate the noise; yet for the torque signal, when the frame was increased, the sharp cut-offs in torque due to the anti-skid system were smoothed out as well. The effect is less noticeable for dry runway tests, as the wheels do not often skid on dry runways. For wet runways, with significant skidding, an SG filter with a large frame would omit these anti-skid actions.

A sensitivity analysis was performed by varying the frame rate and order and observing the signal output and the average error. Forom this analysis

the results were to use a small frame a 3rd order fit was used. While some low-frequency noise is retained the actions of the anti-skid system are well defined. Figure 7.3 shows the result of the chosen SG filter for a dry runway while Figure 7.4 shows the results for a wet runway.
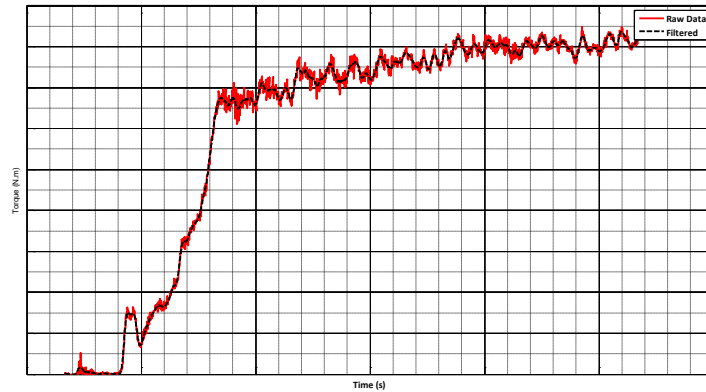

Figure 7.3: Torque raw data and filtered for dry runway after using the Savitzky-Golay filter with a small frame
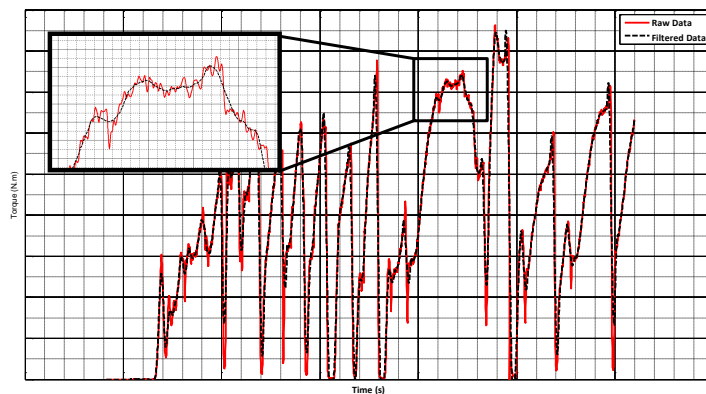

Figure 7.4: Torque raw data and filtered for a wet runway using the Savitzky-Golay filter with a small frame. We see that the filter removes the high-frequency noise, but retains the torque cut-off caused by the anti-skid system

7.2.2 Vertical Load Filter

The vertical load filtering presented a different problem. There is very little variation in the vertical load when the aircraft is on the ground. This naturally leads to the assumption that we can use a very large frame to remove the high and low frequency noise. However, many of the flight tests studied were landings, where the vertical load is zero until touchdown, after

which an immediate large force is placed on the wheels. This time-interval, the detection of the touchdown, is very important in the identification process for the recalculation of the rolling radius (see Section 7.3). As a consequence, a proper estimation of the vertical load is needed for the time interval between touchdown and full weight on the wheels. If a large frame is used, the important load variation during this time interval is smoothed out. On the other hand, using a small frame for the entire time interval results in the retention of the low and high frequency noise.

The solution is to use a variable frame for the vertical load. We first identify the touchdown by monitoring the vertical load on the wheels. The variable frame is implemented as:

– from the beginning of the data up until a point in time 4 seconds after touchdown – a small frame is used which captures the dynamic conditions associated with the point of touchdown

– from the point 4 seconds after touchdown until the end of the data – a large frame is used which smooths the oscillations present in the data

The time period of 4 seconds was chosen as a result of an analysis which showed that the dynamic conditions present at the moment of touchdown are present for approximately 4 seconds
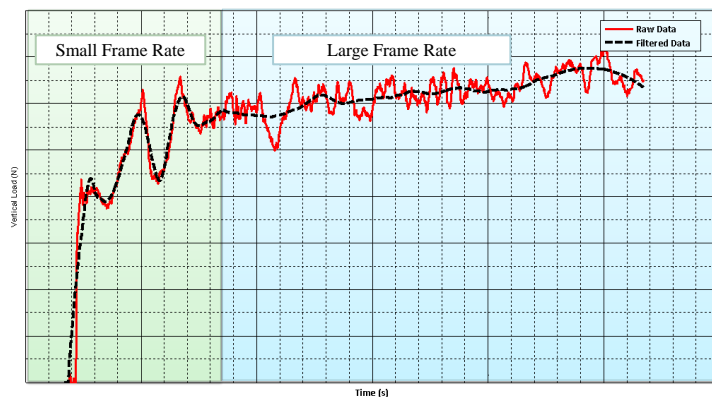
The result of this variable frame is shown in Figure 7.5

Figure 7.5: Variable frame Savitzky-Golay filter to model the vertical load taking the importance of the touchdown into account

7.3 Rolling Radius Estimation

The rolling radius, R_R, is the effective radius of the tire when it has been deformed. The most reliable way to measure the rolling radius is to measure the distance traveled in one revolution by a tire under loading. The distance traveled, d, is then related to the rolling radius by $d = 2\pi R_R$

The rolling radius is a critical parameter as it appears in both equations (7.1) due to the transformation of torque into a braking force and (7.3) as it is used to calculate the circumferential velocity, v_c, from the angular velocity ω_w. However, it is also one of the most difficult parameters to calculate as there exists no direct method with which to measure it, and it is affected by several other factors such as tire pressure, vertical load on the axle and tire braking.

It has been found that in general, the rolling radius varies between 3 to 4% for a tire of nominal gauge pressure and is nominally vertically loaded. For the calculation of the braking force, F_x, by equation (7.1), this results in a small but negligible error of 3 to 4% since the braking force is directly proportional to the rolling radius. For the calculation of the slip ratio, σ_x, this will also induce an error of 3 to 4%, however as we will demonstrate below, this will have a much larger consequence on the estimation of the braking force from the Brush Model.

7.3.1 Sensitivity of Braking Force on Rolling Radius

As we have seen in the derivation of the Brush Model (Chapter 2), the final equation which computes the braking force (eq (2.30)) is a cubic polynomial as a function of the slip ratio. Due to the form of this curve, for small slip values, a small error on the slip ratio creates a very large error on the computed braking force (and thus the global coefficient of friction μ). In Figure 7.6, we plot the effects of a 3% error in the slip ratio which would result from a 3% error in the rolling radius estimation. As we can see, the percent error is enormous. If we assume that our aircraft's anti-skid system is functioning in order to regulate the slip ratio at between $8 - 12\%$, we see that we could have an error in the μ estimation (or the braking force estimation) of $10 - 40\%$. **Consequently, we must have millimeter accuracy on the rolling radius estimation in order to minimize the error on our braking force.**

7.3.2 Method - Ground Speed Matching

The most straight forward method to determine the rolling radius is to equate the distance traveled by the axle of the wheel to an equivalent circumferential distance. By this method, we can equate the velocity of the axle of the actual tire and the circumferential velocity of our equivalent perfectly circular tire with rolling radius, R_R. *However, this method is only applicable if the wheel is free rolling i.e. no tire braking is occurring.* The rolling radius is strongly a function of the vertical load. It is for this reason that we cannot use the nose wheel (which has no brakes) to determine constantly the rolling radius. On the aircraft, there are several sources available to measure the ground speed. Due to the advances in GPS technology, the preferred source
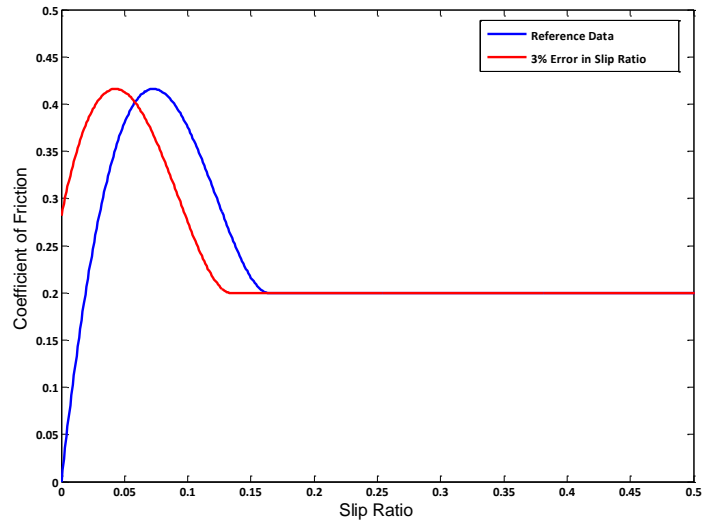
(a) $\mu - slip$ Curve for Error in Slip of 3%
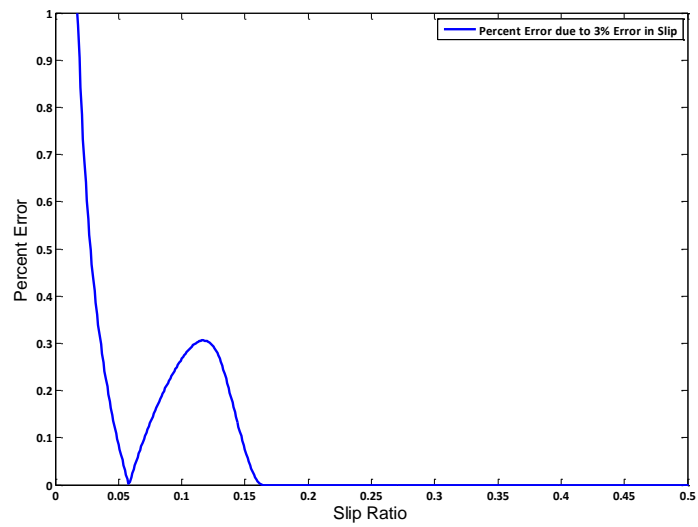
(b) Percent Error of μ due to an Error in Slip of 3%

Figure 7.6: We demonstrate the effects that a 3% error in the slip ratio has on the estimated values of μ from the Brush Model.
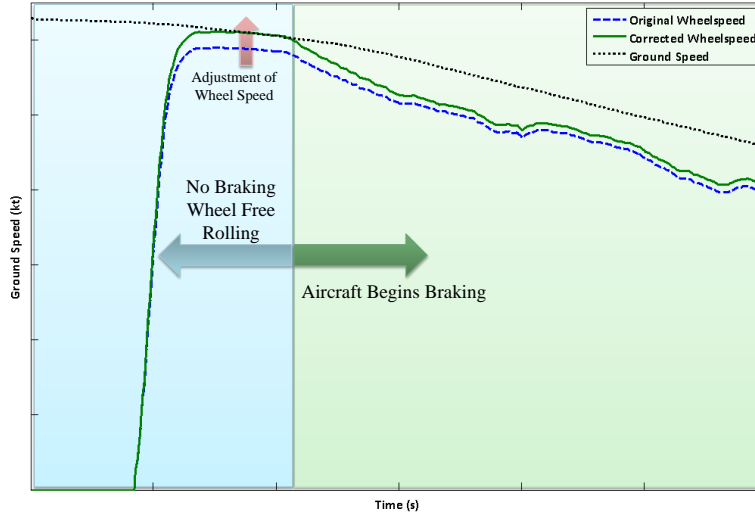
Figure 7.7: Original wheelspeed with pre-defined wheel radius is adjusted to match the ground speed when the tire is free-rolling (no braking)

is to use the GPS longitudinal velocity as the reference ground speed, v_x along with the tachometer sensors available on each wheel to measure the ω_w. From this we can equate

$$v_x = v_c = \omega_w R_R \tag{7.4}$$

That is to say, when the tire is free rolling, the circumferential speed, v_c, of an equivalent wheel with a rolling radius, R_R, should be equivalent to the velocity in the $x - axis$ of the wheel axle, v_x.

From flight test data, the angular velocity of the wheels, ω_w, is measured using tachometers on each wheel. In the flight test data used, the angular velocity is multiplied by a constant rolling radius (usually underestimated), R_{R_0} to obtain a reference wheel speed, v_{c_0}. We see this data in Figure 7.7. As a consequence, we re-calculate the angular velocity by $\omega_w = v_{c_0}/R_{R_0}$ before determining the new rolling radius by matching with the ground speed.

7.4 Anti-Skid Functioning

Aircraft are equipped with an anti-skid system similar to the design used in automobiles more commonly known as *ABS*. A detailed explication of the anti-skid system will not be given here as it is not necessary for an understanding of friction modeling, as well there are in fact several different types of anti-skid systems. A brief explanation of the anti-skid systems follows below.

We retrace the generic form of the $\mu - slip$ curve as generated by the Brush Model equation (2.30) and displayed in Figure 7.8. In anti-skid anal-
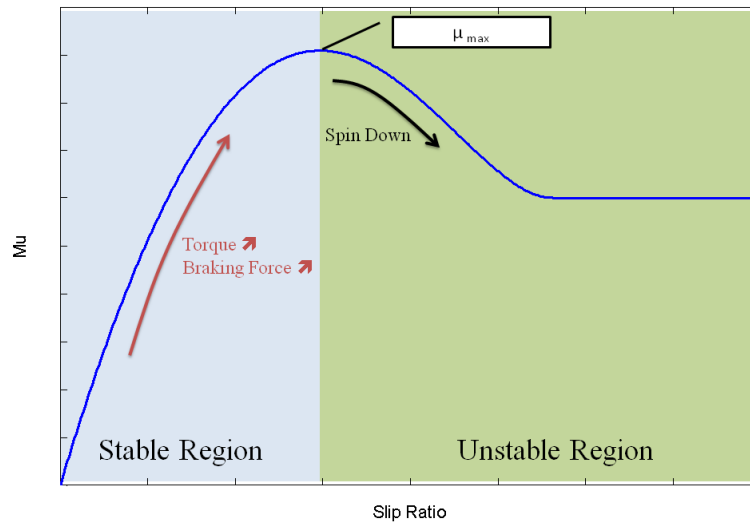
Figure 7.8: $mu - slip$ curve from an anti-skid point of view

ysis, we partition this curve into two regions: stable and unstable regions. The stable region is found to the left of the peak of the $\mu - slip$ curve, while the unstable region is found to the right of the $\mu - slip$ curve.

If we visualize the braking system as applying a torque that starts at zero and continuously increases, assuming that the rolling radius and vertical load remain constant, this increasing torque directly results in the μ increasing ($F_x = T_q/R_R$ and $\mu = F_x/F_z$). As the torque continues to increase, the μ will increase to its maximum value μ_{max}. If the torque continues to increase, we pass to the unstable side of the $\mu - slip$ curve and the tire slip ratio will rapidly increase. This is known as the tire *falling* into a skid. A skidding tire poses two problems: the μ is lower than its optimum value therefore braking ability is lost, and more importantly, significant heating will occur in the tire that may lead to a tire burst if the skid is prolonged.

Thus the basic functioning of the anti-skid system is to monitor the slip ratio (via the wheel speed) to ensure that the torque applied to the wheel keeps the braking system on the stable side of the $\mu - slip$ curve. If the anti-skid system detects that the wheel is falling into a skid, the system intervenes by modulating the pressure applied to the braking system thus modulating the torque applied to the wheel.
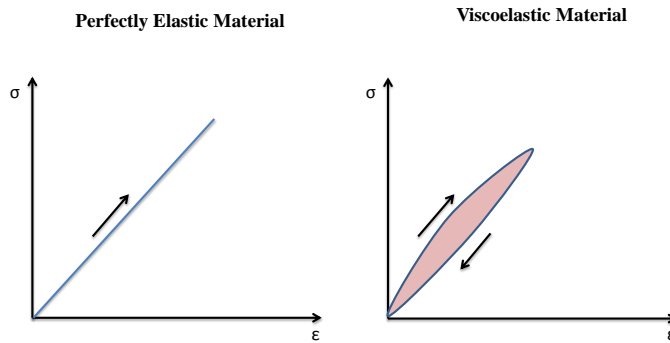
Perfectly Elastic Material   **Viscoelastic Material**

Figure 7.9: Using the derivative of the wheel velocity to remove the data points when the wheel is spinning-up

7.5 Brake Release Removal

It is due to the anti-skid functioning that we have to analyze the data to remove the points where the anti-skid system is triggering a reduction in the brake pressure that causes the tire to *spin-up* i.e. increase its wheel speed. During these moments, the torque sensors measure the hysteresis effect which are not taken into account in the Brush Model.

The hysteresis effect is due to the viscoelastic properties of the rubber. Chapter 3 described the viscoelastic properties that rubber has. We reuse a figure from Chapter 3 and present it in Figure 7.9. A perfectly elastic material will follow the same line on a stress-strain curve whether the stress is being applied or released. However a viscoelastic material will follow a different line on after the reduction of stress due to the energy lost due to the internal friction of the material, known as hysteresis. The torque being applied to the wheel and then released has the same effect. As such, the data points measured after the brake torque has been released will be significantly below the points during which the torque was being applied. These points distort the shape of the $\mu - slip$ curve and interfere with a correct identification.

To remove these points, we use a simple procedure that has proven to be effective. We use the derivative of the circumferential speed, dv_c/dt i.e. the wheel acceleration. We remove all points where the wheel acceleration is positive i.e. the wheel is spinning-up. An example of a the wheel-speed plotted with all of the hysteresis points removed is shown below in Figure 7.10.
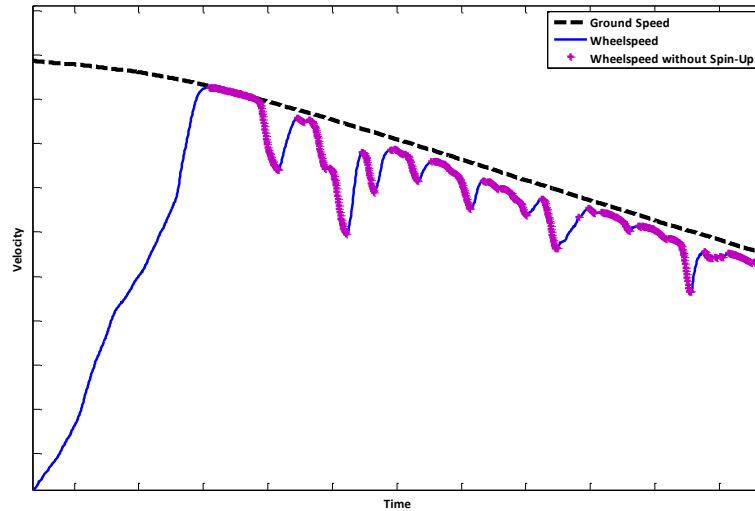
Figure 7.10: Using the derivative of the wheel velocity to remove the data points when the wheel is spinning-up

7.6 Skid Detection

It will be shown in Chapter 9 that it is beneficial to determine the data points that are on the unstable side of the $\mu - slip$ curve as they will help in the curve-fitting techniques. Thus we demonstrate a method to determine if the tire is *falling* into a skid.

We use the derivative of the wheel speed to obtain the wheel circumferential acceleration. We then identify all of the zero crossings of the derivative for which the derivative is a local minimum. These zero-crossings represent the bottom of the skid i.e. the point where the wheel begins to *spin-up* again.

However, there may be small fluctuations in the torque which cause local zero-crossings of the wheel acceleration that do not represent a true skid, or the bottom of the skid. Thus we determine whether the local minimum represents a true skid by taking the average of the wheel acceleration for the 0.1 seconds preceding and following the local minimum. If the mean of the preceding points surpasses a set threshold AND the mean of the subsequent points surpass a different set threshold then we conclude that the local minimum is a *true-skid*. The thresholds vary on tire-design and are manually adjusted for tire types to achieve maximum detectability of the skids.

Figure 7.11 displays the true-skids detected for an aircraft braking using the above explained algorithm. We notice that there are several local minimums that are not taken into account as they do not meet the criteria of a true skid.
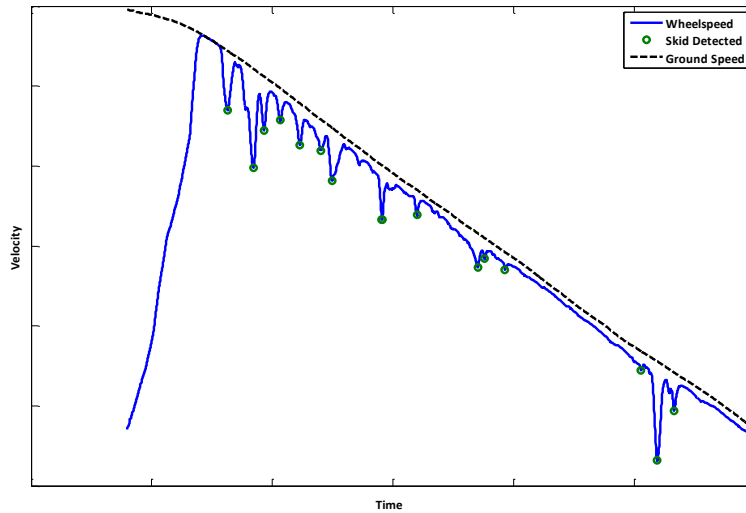
Figure 7.11: Skid-Detection algorithm

7.7   Conclusion

This Chapter dealt with the preprocessing of the flight test data for use both within the Brush Model and as a comparison to the Brush Model output. The preprocessing focused on three major themes: filtering the data to remove noise, determining the rolling radius and identifying the functioning of the anti-skid system. An extensive validation of the processed data was made to ensure that the final product generated consistent, accurate results. The validation results are not shown here.

The following Chapter (8) presents the curve-fitting technique used to identify the Brush Model parameters using flight test data. While the subsequent Chapter (9) presents the results of this curve-fitting technique.

Chapter 8

Identification Algorithm

Summary. Nous avons démontré au chapitre 7, qu'il est possible de dériver la force de freinage, F_x, à partir des paramètres mesurés sur les avions utilisés pour les tests en vol. Ces paramètres permettent également de dériver la charge verticale, F_z, la longueur de la zone de contact, a et le taux de glissement longitudinal $sigma_x$. Il reste donc trois paramètres inconnus ou restant à estimer : la rigidité du pneu, c_{px}, et les coefficients de frottement statique et dynamique, μ_{sx} et μ_{kx}. Ces trois paramètres peuvent être, soit estimés par les techniques vues aux chapitres 3 à 6, soit identifiés à partir des données des essais en vol. Nous allons dériver un algorithme de minimisation qui permettra d'identifier les paramètres inconnus en minimisant l'erreur entre le modèle de la brosse et les données des essais en vol. La dérivation prend comme hypothèse que ces trois paramètres sont inconnus, mais l'algorithme peut également être utilisé pour une optimisation à un ou deux paramètres, c'est-à-dire si l'un des paramètres est identifié.

Goal *The goal of this chapter is to derive an identification algorithm that will minimize the error between the braking force measured in flight tests and the braking force predicted by the Brush model by varying unknown coefficients within the Brush Model.*

8.1   Introduction

The Brush Model, as derived in Chapter 2 is rewritten below. We have demonstrated in Chapter 7, that from flight test data we can derive the braking force, F_x, from parameters measured on the flight test aircraft. From these measured aircraft parameters we can also derive the vertical load, F_z, the length of the contact area, a and the slip ratio $sigma_x$. This leaves three parameters unknown or to be estimated: the tire stiffness, c_{px}, and the static and dynamic coefficients of friction, μ_{sx} and μ_{kx}. These three

parameters can either be estimated using the science derived in Chapters 3 through 6 or they can be identified from flight test data.

We will derive a minimization algorithm that will identify the unknown parameters by minimizing the error between the Brush Model and the flight test data. The derivation will assume that all three parameters are unknown, but the algorithm can also be used for a one or two parameters optimization i.e. if one of the parameters is identified.

We recall the form of the Brush Model:

If $\sigma \leq \sigma^o$ then

$$F_x = -2c_{px}a^2\sigma_x + \frac{4}{3}\frac{c_{px}^2 a^4 \sigma^2}{F_z \mu_{sx}}\left(2 - \frac{\mu_{kx}}{\mu_{sx}}\right) + \frac{8}{27}\frac{c_{px}^3 a^6 \sigma^3}{F_z^2 \mu_{sx}^2}\left(-3 + 2\frac{\mu_{kx}}{\mu_{sx}}\right) \quad (8.1)$$

Else if $\sigma_x > \sigma_x^o$ then

$$F_x = -\mu_{kx}\frac{v_g}{|v_g|}|F_z|$$

where

$$\sigma^o = \frac{3F_z \mu_{sx}}{2a^2 c_{px}}$$

8.2   Notation

The following analysis will use the notation below.

Supercripts

^{M} - Model

^{E} - Flight Test (Essai)

^{V} - Real/True Value (Vrai)

^{o} - Initial Value

8.3   Algorithm

We can represent the Brush Model by:

$$F_x^M(i) = f\left(c_{px}^V, \mu_{sx}^V, \mu_{kx}^V, F_z^V(i), \sigma_x^V(i)\right)$$

The goal of this optimization is to minimize the error between the horizontal braking force given by the brush model, F_x^M and the horizontal braking force calculated from the flight test data analysis F_x^E.

$$min(|F_x^E - F_x^M|)$$

8.3.1 Simplification

In general, the flight test data consists of one landing which has a duration of approximately 30 seconds. Because the flight test data are braking tests, for each moment of time the velocity is decreasing. **In order for the minimization to function, we assume that during the time interval in which we are making using the algorithm, the three coefficients c_{px}, μ_{sx} and μ_{kx} remain constant.** The discussion as to the validity of this assumption is presented in Chapter 9 Section 9.2. Therefore the minimization function may be repeated several times for different velocity intervals. The derivation below is described for the data points contained within one chosen interval.

The interval of time chosen will be represented by H where $i = 1...H$

Additionally, aircraft have n tires braking simultaneously. As such for each time step i, we may have $j = 1...n$ data points for each time step. For simplicity in the derivation, we will not represent the minimization algorithm as a function of the number of tires n. The minimization algorithm contains the ensemble of data points from all chosen tires.

8.3.2 Flight Test Error

Flight test data may include an error or bias. Chapter 7 demonstrated several preprocessing steps taken to remove data error. However there may still be residual error included in the data which we do not want to affect the minimization algorithm. Therefore we make the hypothesis that the data coming from flight test data has a known error. Thus the real value (denoted with superscript ^{V}) of the variable must be found within an interval of uncertainty.

$$\left| F_z^V(i) - F_z^E(i) \right| \leq \epsilon_1$$
$$\left| \sigma^V(i) - \sigma^E(i) \right| \leq \epsilon_2$$
$$\left| F_x^E(i) - F_x^V(i) \right| \leq \epsilon_3$$

We will assume that the real value of the braking force, F_x^V is associated with the value calculated from flight test data, within a zone of uncertainty.

$$F_x^E - \epsilon_3 \leq F_x^V \leq F_x^E + \epsilon_3$$

If we input the variables that are available from flight test data we obtain

$$F_x^M = f(c_{px}, \mu_{sx}, \mu_{kx}, F_z^E + \epsilon_1, \sigma^E + \epsilon_2)$$

8.3.3 Initial Conditions

We choose initial conditions of the three unknown parameters as c_{px}^o, μ_{sx}^o and μ_{kx}^o. The curve fitting algorithm will attempt to identify the correct values of these parameters by varying $[\lambda_c, \lambda_s, \lambda_k]$ where

$$c_{px}^V = c_{px}^o + \lambda_c c_{px}^o$$
$$\mu_{sx}^V = \mu_{sx}^o + \lambda_s \mu_{sx}^o$$
$$\mu_{kx}^V = \mu_{kx}^o + \lambda_k \mu_{kx}^o$$

The most general constraint we will place on the parameters is that $\lambda_i > -1$. This ensures that c_{px}^V, μ_{sx}^V and μ_{kx}^V are always positive.

We define in the next section several additional constraints that will bound the problem based on the physics of tire-runway contact theory.

8.3.4 Constraints

The comparison of the Brush Model form with flight test data poses a particular difficulty to correctly identify the unknown parameters. The problems associated with the form of the flight test data itself will be treated in Chapter 9 Section 9.3. The second problem is due to the form of the model as a third order polynomial in σ_x with three unknowns. In most cases, there is a near infinite number of solutions (local minimums) that satisfy the constraints. Although the solution may be a local minimum, the identified parameters c_{px}^V, μ_{sx}^V and μ_{kx}^V may not represent a realistic value based on our knowledge of contact physics e.g. a solution could be found where $\mu_{sx}^V = 10$ while $\mu_{kx}^V = 1E^{-10}$. We represent schematically the problem of several solutions satisfying the flight test data in Figure

Therefore we must correctly bound the problem by representing the physics of the problem using constraints on the permitted values.

Constraint 1   The first constraint is that $\mu_{sx} > \mu_{kx}$. This constraint is based on tribology (Chapter 6) which has shown that the static coefficient of friction is greater than the dynamic coefficient of friction for rubber sliding.

Constraint 2   We will constrain the static coefficient of friction so that $\mu_{sx} < 1.5$. This constraint is based on the specific case of aircraft tires and runways. Although rubber friction can reach higher values than 1.5 in other applications, the types of rubber used in the aircraft industry, combined with the elevated contact pressures have shown that the static coefficient of friction is not greater than 1.5.

Constraint 3   We will constrain the upper limit of the tire-stiffness, c_{px}, to a maximum of 10 times the initial value. This is done because we have a good initial estimate of the tire-stiffness, c_{px}^o. We know that the tire-stiffness varies as a function of vertical load, tire-pressure and temperature, however it has not been experimentally shown to vary by orders of magnitude.

Constraint 4   The flight test data that is being used are specific tests were the aircraft is braking at its maximum ability. As such, we assume that the anti-skid is active and regulating the braking to obtain the maximum braking on the $\mu - slip$ curve. During the interval where the identification is being performed, we compute the maximum braking force. We recall that in Chapter 2 Section 2.5 we identified key points on the $\mu - slip$ curve. One of these key points was the maximum braking force predicted by the Brush Model

$$F_{x_{max}} = \frac{3\mu_{kx} - 4\mu_{sx}}{(2\frac{\mu_{kx}}{\mu_{sx}} - 3)^2} F_z$$

Thus we can add a constraint that the maximum braking force predicted by the brush model must be close to the actual maximum braking force measured during the flight test interval with a certain uncertainty

$$0.9 F_{x_{max}}^E < F_{x_{max}}^M < 1.1 F_{x_{max}}^E$$

8.3.5   Curve-Fitting Algorithm

Recall that the brush model, has the form

$$F_x^M(i) = f\left(c_{px}^V, \mu_{sx}^V, \mu_{kx}^V, F_z^V(i), \sigma_x^V(i)\right)$$

Knowing the error associated with the flight test parameters, we can determine the boundaries that the real value must be found within.

$$max(0, F_z^E(i) - \epsilon_1) \leq F_z^V \leq F_z^E + \epsilon_1$$
$$max(0, \sigma^E(i) - \epsilon_2) \leq \sigma^V \leq \sigma^E + \epsilon_2$$

Looking at the form of equation (8.1) we note that:
As F_z^V increases, F_x^M decreases
As σ^V increases F_x^M increases
Therefore we can ascertain that the maximum possible value of the horizontal force, $\overline{F}_x^M$, occurs when F_z^V is at the minimum and σ^V is at the maximum. While the minimum possible value of the horizontal force, $\underline{F}_x^M$, occurs when F_z^V is at the maximum and σ^V is at the minimum. Such that

$$\overline{\psi}(i, \lambda_c, \lambda_s, \lambda_k) = \overline{F}_x^M \left(i, c_{px}^o + \lambda c_{px}^o, \mu_{sx}^o + \lambda \mu_{sx}^o, \mu_{kx}^o + \lambda \mu_{kx}^o, max(0, F_z^E(i) - \epsilon_1), \sigma^E(i) + \epsilon_2 \right)$$

$$\underline{\psi}(i, \lambda_c, \lambda_s, \lambda_k) = \underline{F}_x^M \left(i, c_{px}^o + \lambda c_{px}^o, \mu_{sx}^o + \lambda \mu_{sx}^o, \mu_{kx}^o + \lambda \mu_{kx}^o, F_z^E(i) + \epsilon_1, max(0, \sigma^E(i) - \epsilon_2) \right)$$

Therefore we know that the horizontal force calculated by the brush model must fall within the boundary

$$\overline{\psi}(i, \lambda_c, \lambda_s, \lambda_k) \leq F_x^M \leq \underline{\psi}(i, \lambda_c, \lambda_s, \lambda_k)$$

Additionally, we know that the comparative horizontal force coming from flight test data must also fall within the boundary of its error

$$max(0, F_x^E(i) - \epsilon_3) \leq F_x^V(i) \leq F_x^E(i) + \epsilon_3$$

Difference between Model and Flight Test

$$\underline{\psi}(i, \lambda_c, \lambda_s, \lambda_k) - \left(F_x^E(i) + \epsilon_3 \right) \leq F_x^M(i) - F_x^V(i) \leq \overline{\psi}(i, \lambda_c, \lambda_s, \lambda_k) - max(0, F_x^E(i) - \epsilon_3)$$

$$\underline{\psi}(i, \lambda_c, \lambda_s, \lambda_k) - \left(F_x^E(i) + \epsilon_3 \right) \leq F_x^M(i) - F_x^V(i) \leq \overline{\psi}(i, \lambda_c, \lambda_s, \lambda_k) - max(0, F_x^E(i) - \epsilon_3)$$
$$\underline{B}(i, \lambda_c, \lambda_s, \lambda_k) \leq F_x^M(i) - F_x^V(i) \leq \overline{B}(i, \lambda_c, \lambda_s, \lambda_k)$$
$$\left| F_x^M(i) - F_x^V(i) \right| \leq max \left(\overline{B}(i, \lambda_c, \lambda_s, \lambda_k), \underline{B}(i, \lambda_c, \lambda_s, \lambda_k) \right)$$
$$\left| F_x^M(i) - F_x^V(i) \right| \leq E(i, \lambda_c, \lambda_s, \lambda_k)$$

Minimize the error between the flight test and the model while obeying the constraints posed by the physical representation of the model.

$$min \sum_{i=1}^{T} E(i, \lambda_c, \lambda_s, \lambda_k)$$

Find $\lambda_c^*, \lambda_s^*, \lambda_k^*$

$$c_{px}^V = c_{px}^o + \lambda_c^* c_{px}^o$$
$$\mu_{sx}^V = \mu_{sx}^o + \lambda_s^* \mu_{sx}^o$$
$$\mu_{kx}^V = \mu_{kx}^o + \lambda_k^* \mu_{kx}^o$$

8.4 Conclusion

We have defined an identification algorithm which will identify up to three unknown parameters by minimizing the error between flight test data and the Brush Model. The algorithm is flexible in its usage. The unknown parameters can be estimated before hand using the theories developed within this report. In this case the three parameter identification can become either a two or one parameter fitting. Chapter 9 will explore several different applications of this identification algorithm for both three parameter fitting and two parameter fitting.

Chapter 9

Comparison Brush Model and Flight Test

Summary. Nous avons au total sept coefficients : F_x, F_z, a, σ_x, c_{px}, μ_{sx} et μ_{kx}. À partir des données des essais en vol, nous mesurons (ou calculons à partir des données mesurées) les quatre coefficients suivants : F_x, F_z, a et σ_x. Il reste donc trois paramètres inconnus : c_{px}, μ_{sx} et μ_{kx}. Comme mentionné au chapitre 7, il existe deux méthodes pour obtenir ces paramètres inconnus :

  – Estimation : à l'aide des théories scientifiques développées dans les chapitres 3 à 6
  – Identification : à l'aide de l'algorithme d'ajustement de courbe développé au chapitre 8

Dans ce chapitre, nous allons évaluer plusieurs méthodes de détermination de ces paramètres, soit par identification, soit par estimation. La Figure 9.1 présente de manière schématique le procédé qui est mis à jour dans chaque chapitre pour présenter l'approche choisie. Pour pouvoir utiliser l'algorithme d'identification, nous allons ajuster la courbe sur une plage de points de données. Nous prenons comme hypothèse que, pour la plage de points de données considérée, les paramètres inconnus restent constants, autrement dit, nous allons chercher la ou les valeurs uniques qui remplissent les critères de la minimisation. Au cours de l'optimisation, cette hypothèse nous oblige souvent à faire un choix sur la plage de points de données à choisir et sur la validité de l'hypothèse que, sur cette plage, les paramètres inconnus restent constants. Il existe des avantages et des inconvénients à augmenter le nombre de points de données. Si le nombre de points augmente, nous avons un ensemble de données plus large sur lequel nous pouvons effectuer l'ajustement de la courbe, augmentant ainsi la confiance dans l'exactitude des valeurs trouvées lors de cet ajustement. À l'inverse, un ensemble de données plus large augmente le risque que les paramètres inconnus ne soient plus constants sur la plage complète. Nous présentons deux options à considérer pour déterminer l'ensemble de données pour l'algorithme de minimisation.

Nombre de roues Les avions sont équipés de plusieurs roues freinées. Les avions de la flotte d'Airbus sont équipés de quatre roues freinées au minimum et de 16 roues freinées simultanément au maximum. Ceci signifie que, pour un seul pas de temps, nous pouvons avoir jusqu'à 16 points de données. En prenant en compte toutes les roues, nous multiplions la taille de notre ensemble de données par le nombre n de roues. Considérant que chaque pneu est freiné indépendamment des autres, nous obtenons une plage de données beaucoup plus large pour effectuer l'identification. Cependant, utiliser toutes les roues dans l'ensemble de données suppose que tous les pneus ont des caractéristiques mécaniques et un comportement analogues (la piste peut être partiellement contaminée par des dépôts de caoutchouc de manière à ce que seulement certaines roues entrent en contact avec le contaminant). L'un des paramètres inconnus est c_{px}, la rigidité du pneu. Comme indiqué au chapitre 5, la rigidité du pneu est principalement fonction de la charge verticale sur le pneu et de la pression du pneu. En outre, les recherches menées en science des matériaux (Chapitre 3) ont démontré que la rigidité du pneu varie également à cause de la chaleur produite lors du freinage. En utilisant tous les pneus dans le même ensemble de données, nous considérons que tous les pneus ont les mêmes propriétés mécaniques et rencontrent les mêmes conditions sur la piste. Nous allons démontrer l'effet d'une utilisation de tous les pneus ou d'un traitement de chaque pneu séparément dans le chapitre résultats. Intervalles de vitesse La taille de l'ensemble de données dépend de l'intervalle de temps sur lequel les données sont incluses. Comme tous les tests sont associés au freinage, à chaque pas de temps, la vitesse diminue. De la même manière que précédemment, un intervalle de temps plus large augmente le nombre de points de données sur lesquels effectuer l'identification. Un ensemble plus large de données comprend en général une plus grande variation dans les points de données, ce qui augmente la confiance dans l'identification des paramètres. Cependant, cette méthode repose sur l'hypothèse que les paramètres inconnus sont constants sur l'intervalle. Nous rappelons que les paramètres inconnus sont c_{px}, μ_{sx} et/ou μ_{kx}. Comme nous l'avons vu dans le chapitre sur la tribologie (6), le coefficient de frottement dépend de la vitesse de glissement, qui se modifie constamment sur l'intervalle de temps. De plus, l'absorption de chaleur due au freinage augmente en fonction du temps et modifie les caractéristiques mécaniques du caoutchouc. En conséquence, la rigidité du pneu et le coefficient de frottement sont modifiés. Nous allons analyser les effets de l'intervalle de vitesse et allons essayer de trouver une optimisation entre un nombre de points suffisant pour identifier les paramètres et l'hypothèse que les paramètres inconnus sont constants sur l'ensemble de données. Difficultés Partitionnement des données La Figure 9.3 rappelle la forme de la courbe $\mu - slip$. Si le pilote freine à l'aide des pédales, au moment où il commence à appuyer sur les pédales, la pression de freinage augmente, ce qui entraîne une augmentation du couple de freinage. Suivant la courbe $\mu - slip$, une augmentation du

couple de freinage entraîne une augmentation du taux de glissement longitudinal. Si le pilote continue d'appuyer sur les pédales (et si les freins ont un couple suffisant), la force de freinage atteint un maximum et les pneus peuvent patiner, autrement dit le taux de glissement longitudinal continue à augmenter alors que la force de freinage diminue. Cette situation déclenche le système antidérapage de l'avion, qui régule la pression appliquée sur les freins pour maintenir la force de freinage la plus élevée sans dérapage des roues. En général, plus le système antidérapage est perfectionné, plus les points de données $\mu - slip$ sont densément groupés en partie haute de la courbe $\mu - slip$. Alors qu'un système antidérapage performant est essentiel pour optimiser le freinage des avions, il présente des inconvénients dans l'utilisation des algorithmes d'identification. Plus les points de données sont densément groupés, plus il est difficile de déterminer la forme réelle de la courbe $\mu - slip$ à l'aide des algorithmes d'identification. Ceci augmente le nombre de solutions possibles, comme montré schématiquement Figure 9.2. Les travaux futurs sur ce sujet peuvent utiliser des essais en vol spécifiques où le freinage est régulé pour obtenir une plage plus grande de points de données. Freinage à couple limité Nous avons montré que le système antidérapage maintient la force de freinage sur la partie stable de la courbe $\mu - slip$. Cependant, il existe une autre condition qui peut également limiter les points de données sur la partie stable de la courbe : la limitation de couple. Ceci se produit quand les freins ne peuvent pas donner plus de force de freinage que le maximum de la courbe $\mu - slip$. En conséquence, même au freinage maximum, la roue ne patine pas et reste sur la partie stable. Cette situation est plus susceptible de se produire sur des pistes sèches. Comme nous le verrons au chapitre 9.4, les points groupés principalement sur la partie stable de la courbe rendent difficile l'identification correcte de μ_{sx} et μ_{kx}, s'ils sont tous les deux inconnus. Cela est dû au fait que les variables μ_{sx} et μ_{kx} ont une plus forte influence sur la forme de la courbe $\mu - slip$ quand le taux de glissement longitudinal augmente. Les raisons de ce phénomène peuvent être déterminées à partir de la dérivation du modèle de la brosse (voir chapitre 2). Dans tous les cas, sans points de données sur la partie instable de la courbe, il est presque impossible de déterminer les variables μ_{sx} et μ_{kx}, comme démontré Figure 9.4. Comme nous pouvons le constater, malgré des différences significatives entre les valeurs de μ_{sx} et μ_{kx}, la partie stable (à gauche) de la courbe a sensiblement la même forme.

Pistes sèches contre pistes humides Pour toutes les raisons précédentes (points de données groupés, freinage à couple limité), le procédé d'identification est plus robuste pour les essais effectués sur des pistes humides que sur des pistes sèches. Sur les pistes humides, il est moins probable d'avoir une limitation de couple et, comme la piste est généralement plus glissante, la roue entre plus souvent en dérapage, avec comme résultat une plage plus grande de points de données sur la courbe $\mu - slip$. Une telle plage de points de données rend l'algorithme d'identification plus précis et augmente

la confiance dans les résultats. Néanmoins, les pistes humides posent des problèmes particuliers en raison des effets de l'hydrodynamique sur le frottement. Ces effets dépendent de la vitesse des avions, qui, comme mentionné au chapitre 9.2.2, diminue pour chaque pas de temps. Ainsi, l'hypothèse que les variables inconnues, à savoir les coefficients de frottement, restent constantes lors d'un intervalle devient contestable. Nous pouvons réduire l'intervalle de temps des données pour minimiser la modification de la vitesse sur cet intervalle, mais nous devons alors réduire le nombre de points de données dans l'intervalle pour effectuer l'identification. Néanmoins, la majorité des essais en vol s'effectuent sur des pistes sèches. Certains essais sont exécutés sur des pistes humides (ou des pistes contaminées : glace, neige, eau stagnante), mais, souvent, ils ne sont pas accompagnés de mesures précises ou d'une description de l'état de la piste (profondeur de l'eau ou de la contamination, parties de la piste recouvertes par la contamination..). En conséquence, il est difficile de corréler les données des essais en vol avec l'état exact de la piste. Données bruitées Le chapitre 7 a présenté le procédé utilisé pour éliminer et/ou filtrer le plus de bruits possible. Les points des données des essais en vol contiennent néanmoins toujours du bruit qui déforme les points $\mu - slip$. Comme illustré Figure 9.4, des modifications importantes des coefficients peuvent ne pas modifier significativement la forme de la courbe $\mu - slip$. Nous avons développé un algorithme (voir chapitre 8) qui cherche à réduire les effets du bruit sur l'algorithme d'identification. Malgré tout, le bruit reste un obstacle non négligeable pour une identification précise. Optimisation multi-paramètres La difficulté d'une optimisation multi-paramètres réside dans le fait qu'il existe plusieurs solutions au problème, voire une infinité de solutions. Alors que la solution peut être un minimum mathématique, les paramètres identifiés peuvent ne pas avoir de signification physique. Le problème se complique encore quand les points de données mesurés sont groupés pendant l'intervalle de temps, en raison du système de freinage, comme nous l'avons expliqué au chapitre 9.3.1. Plus les points sont proches les uns des autres, plus il est difficile de faire une identification correcte. Afin de minimiser le nombre de solutions possibles, il est impératif de circonscrire le problème en utilisant des contraintes qui représentent la physique du problème. Ces contraintes ont été définies au chapitre 8. La solution la plus avantageuse est de réduire le nombre d'inconnues en utilisant des paramètres estimés à la place des paramètres inconnus. Le chapitre 9.5 apporte la démonstration de cette procédure. Les résultats de cette comparaison sont présentés dans ce chapitre. Les travaux se poursuivant sur ce projet, leur objectif sera d'étendre la validation à un plus grand nombre d'essais en vol. L'intégration des effets thermiques dans le problème permettront d'expliquer les tendances décelées dans les paramètres identifiés. En outre, une prochaine étape sera de déterminer le coefficient de frottement pour chaque pas de temps, sur la base de la vitesse réelle de glissement.

Nous avons démontré qu'il est possible d'utiliser le modèle de la brosse avec les données des essais en vol et que, quand les paramètres ont été identifiés, ce modèle donne une valeur de la force de freinage, F_x^M égale à 2% près à celle mesurée lors des essais en vol, F_x^E. Nous avons donc démontré que le modèle de la brosse représente correctement la physique du contact entre le pneu et la piste lors du freinage.

Goal *The goal of this chapter is to use the identification algorithm developed in Chapter 8 along with flight test data to identify unknown parameters in the Brush Model. We will explore several options by varying the known and unknown parameters to determine the level of confidence needed for each of these parameters.*

9.1   Introduction

We present again the form of the Brush Model as derived in Chapter 2 on page 50.

If $\sigma_x \leq \sigma_x^o$ then

$$F_x = -2c_{px}a^2\sigma_x + \frac{4}{3}\frac{c_{px}^2a^4\sigma_x^2}{F_z\mu_{sx}}\left(2 - \frac{\mu_{kx}}{\mu_{sx}}\right) + \frac{8}{27}\frac{c_{px}^3a^6\sigma_x^3}{F_z^2\mu_{sx}^2}\left(-3 + 2\frac{\mu_{kx}}{\mu_{sx}}\right)$$

Else if $\sigma_x > \sigma_x^o$ then

$$F_x = -\mu_{kx}\frac{v_g}{|v_g|}|F_z|$$

In total we have seven coefficients: F_x, F_z, a, σ_x, c_{px}, μ_{sx} and μ_{kx}. From flight test data, we measure (or calculate from measured data) the following four coefficients: F_x, F_z, a and σ_x. This leaves three parameters as unknown: c_{px}, μ_{sx} and μ_{kx}. As mentioned in Chapter 7, there are two methods to obtain these unknown parameters:

- **Estimate**: using the scientific theories developed in Chapters 3 through 6
- **Identify**: using the curve fitting algorithm that is developed in Chapter 8

This chapter will evaluate several methods of determining these parameters, either through identification or estimation. A general schematic of the process is presented in Figure 9.1 and is updated in each section to display the chosen approach.
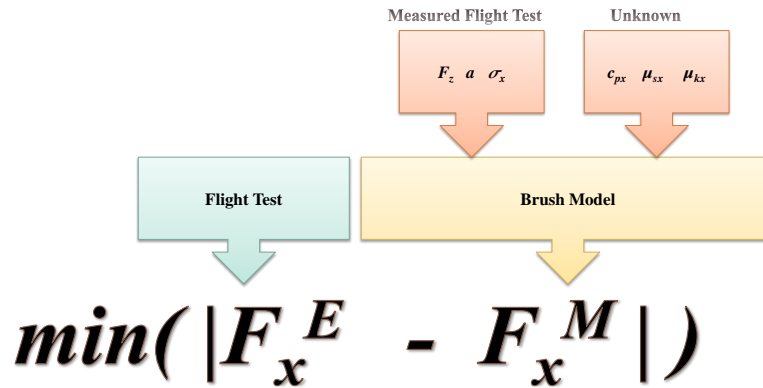
Figure 9.1: The identification algorithm will minimize the error between the brush model frictional force, F_x^M, and flight test data frictional force, F_x^E, by estimating or varying the unknown parameters

9.2 Algorithm Option Discussion

In order to use the identification algorithm, we will make the curve fitting on a range of data points. We make the assumption that for the range of data points considered, the unknown parameters remain constant i.e. we will attempt to find the unique value(s) that satisfies the minimization criteria. Due to this assumption, throughout the optimization process we often have to make a choice concerning the range of data points we wish to have and the validity of the assumption that during this range, the unknown parameters remain constant. There are both advantages and disadvantages to increasing the number of data points. As the number of points increases,we have a larger data set with which to perform the curve fitting, thus in general, increasing the confidence that the values found during the curve fitting technique are correct. Contrary to this however, is the fact that the larger the data set, the increased chance that the unknown parameters may not be constant for the complete data set.

We present two options to be considered when determining the data set for the minimization algorithm.

9.2.1 Number of Wheels

Aircraft are fitted with several braked wheels. For the particular fleet of aircraft that Airbus uses, we have a minimum of 4 braked wheels, to a

maximum of 16 simultaneously braked wheels. This implies that for a single time step, we may have up to 16 data points. Taking into consideration all of the wheels, we multiply the size of our data set by n number of wheels. Given that each tire is braking independently of the others, this generally gives us a much wider range of data with which to make the identification.

However, using all of the wheels in the data set assumes all of the tires have analogous mechanical characteristics and behavior i.e. runway may be partially contaminated by rubber deposits so only certain wheels encounter the contaminant. One of the unknown parameters is c_{px}, the tire-stiffness. As seen in Chapter 5, the tire-stiffness is primarily a function of the vertical load on the tire and the tire-pressure. In addition, the research into Material Science (Chapter 3) demonstrated that the tire-stiffness will also vary due to the heat generated by the braking. By using all of the tires in the same data set, we consider that all of the tires share the same mechanical properties and encounter the same conditions on the runway.

We will demonstrate the effect of using all the tires, or treating each tire separately in the results section.

9.2.2   Velocity Intervals

The size of the data set will depend on the time interval for which we include the data. Due to the fact that all tests are associated with braking, at each time step the velocity will be different i.e. decreasing. In the same way as above, a larger time interval will increase the number of data points for which we will make the identification. A larger data set will usually include a greater variation in the data points present which in general will increase the confidence in our parameter identification.

However this method comes with the assumption that the unknown parameters are constant during the interval. We recall that the unknown parameters may consist of c_{px}, μ_{sx} and/or μ_{kx}. From the Chapter on Tribology (6), we recognize that the coefficient of friction is dependent on the sliding speed which is constantly changing during the time interval. In addition, the heat absorption from braking will increase as a function of time and affect the mechanical characteristics of the rubber. Consequently, both the tire-stiffness and the coefficient of friction will be affected.

We analyze the effects on the velocity interval and attempt to find an optimization between a sufficient number of points for parameter identification and the assumption that the unknown parameters are constant in the data set.

9.3 Difficulties

9.3.1 Clustered Data Points

We recall the shape of the $\mu - slip$ curve below in Figure 9.3. If the pilot was manually braking with the pedals, as the pilot begins to press on the pedals, the brake pressure would increase causing the brake torque to increase. Following the $\mu - slip$ curve, as the brake torque increases, the slip ratio will also increase. If the pilot continues to press on the pedals (and if the brakes have sufficient torque), the braking force will reach a maximum and the tires may fall into a skid i.e. the slip ratio will continue to increase while the braking force will decrease. This will trigger the activation of the anti-skid system of the aircraft, which will regulate the pressure applied to the brakes in order to maintain the highest braking force without the wheel falling into a skid. In general the more advanced the anti-skid system, the more densely clustered the $\mu - slip$ data points will be near to the peak of the $\mu - slip$ curve.

While a well functioning anti-skid system is essential to optimize the aircraft braking, it is disadvantageous for using identification algorithms. *The more closely clustered the data points are, the more difficult it is to determine the true shape of the $\mu - slip$ curve using the identification algorithms.* This increases the number of possible solutions. We demonstrate this problem schematically in Figure 9.2. Future works on this subject may use specific flight tests where the braking is regulated to obtain a wider range of data points.

9.3.2 Torque Limited Braking

We have shown that the anti-skid system functions to keep the braking force on the stable side of the $\mu - slip$ curve. However, there is another condition that can also limit the data points to the stable side of the curve – torque limited. This occurs when the brakes are not capable of providing more braking force than the maximum of the $\mu - slip$ curve. As a result, even at max braking, the wheel does not fall into a skid and it remains on the stable side. This situation is most likely to occur on dry runways.

As we will see in Section 9.4, points clustered primarily on the stable side of the curve make it difficult to correctly identify μ_{sx} and μ_{kx} if both are unknown. This is due to the fact that the variables μ_{sx} and μ_{kx} have a stronger effect on the shape of the $\mu - slip$ curve as the slip ratio increases. The reasons for this can be determined from the derivation of the Brush Model in Chapter 2. In any case, without data points on the unstable side of the curve, it is nearly impossible to determine the variables μ_{sx} and μ_{kx}. We demonstrate this effect in Figure 9.4. As we can see, despite significantly different values of μ_{sx} and μ_{kx}, the stable (left) side of the curve has nearly the same shape.
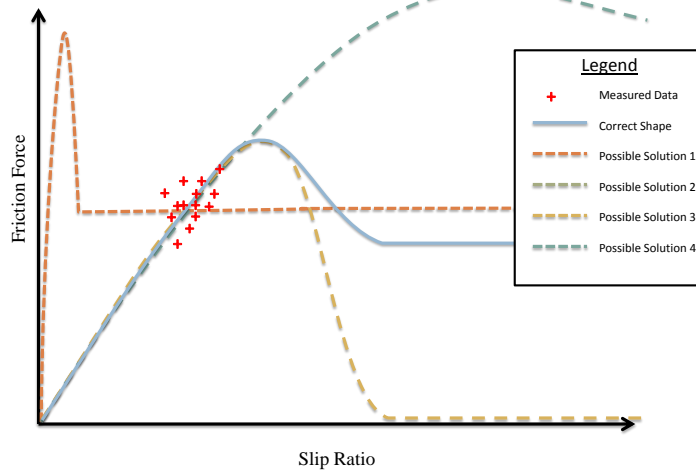
Figure 9.2: This schematic identifies the numerous possible solutions available with a three parameter optimization. The problem is made more difficult when the data points are clustered together as is often the case when braking due to the anti-skid system
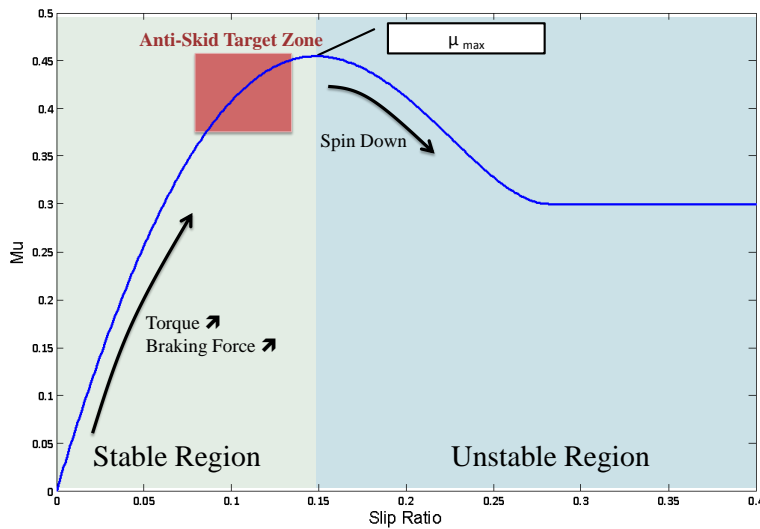

Figure 9.3: The general shape of the $\mu - slip$ curve showing the stable and unstable sides of the curve. When the anti-skid system is functioning, it regulates the braking pressure to obtain the maximum friction force while remaining on the stable side of the curve. The more advanced the anti-skid system, the closer together the $\mu - slip$ data points will be clustered.
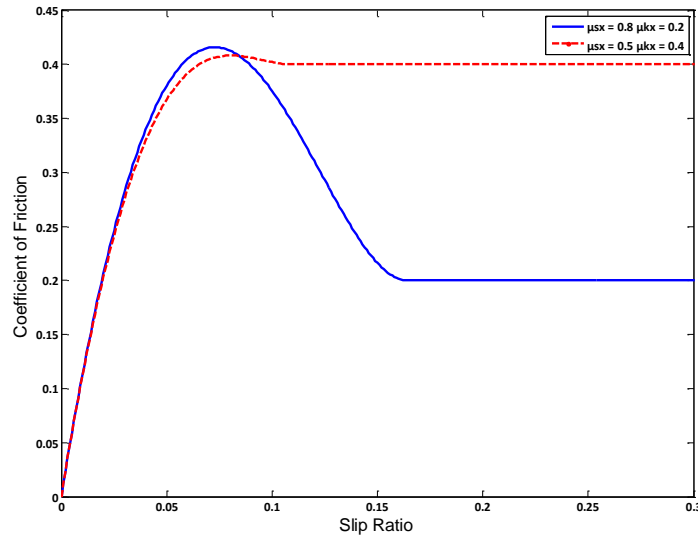
Figure 9.4: The blue curve shows the $\mu - slip$ curve for a $\mu_{sx} = 0.8$ and $\mu_{kx} = 0.2$, while the red-dotted curve uses $\mu_{sx} = 0.5$ and $\mu_{kx} = 0.4$. We see that the stable (left) side of these curves are nearly identical. Consequently, if the flight test data contains only points on the stable side, the identification algorithm will have problems to correctly identify the μ_{sx} and μ_{kx}.

9.3.3 Dry vs Wet Runways

For all of the reasons above (clustered data points, torque limited braking), the identification process is more robust for flight tests performed on wet runways than on dry runways. On wet runways, we are less likely to be torque limited and, because the runway is in general more slippery, the wheel will more often fall into skids, resulting in a larger range of data points on the $\mu - slip$ curve. This larger range of data points makes the identification algorithm more accurate resulting in higher confidence of the results.

Nevertheless, wet runways pose particular problems due the effect of hydrodynamics on friction. The hydrodynamic effects are dependent on the velocity of the aircraft, which, as mentioned above in Section 9.2.2, is decreasing for each time step. Thus the assumption that the unknown variable(s), namely the friction coefficient(s), remains constant during an interval is questionable. We can reduce the data time interval to minimize the change in velocity during the interval, however we then reduce the number of data points in the interval to make the identification.

Regardless, the majority of the flight tests are performed on dry runways. There exists some flight tests performed on wet runways (or contaminated runways: ice, snow, standing water), however these flight tests are often not accompanied by an accurate measurement or description of the runway state

i.e. depth of water or contaminant, portion of the runway covered by said contaminant. As a result, it is difficult to correlate the flight test data with an exact runway state.

9.3.4 Data Noise

In Chapter 7 we presented the process followed to remove and/or filter as much of the noise as possible. Nevertheless, the flight test data points still contain noise that distort the $\mu - slip$ points. As we have seen in Figure 9.4, large changes in the coefficients may not significantly change the shape of the $\mu - slip$ curve. We have developed an algorithm (Chapter 8) that attempts to reduce the effect that the noise can have on the identification algorithm. Even so, data noise will remain a significant hurdle to an accurate identification process.

9.3.5 Multi-Parameter Optimization

What is difficult with a multi-parameter optimization is that there are often several (if not infinite) solutions to the problem. While the solution may be a mathematical minimum, the identified parameters may not have a physical sense.

This problem is further complicated by the fact that the measured data points may be clustered together during the time interval due to the braking system as explained in Section 9.3.1. The closer the points are clustered, the more difficult it is to make a correct identification.

In order to minimize the number of possible solutions, it is imperative to properly constrain the problem using constraints that represent the physics of the problem. These constraints were defined in Chapter 8. The most favorable solution is to reduce the number of unknowns by using estimated parameters in the place of the unknown parameters. This procedure will be demonstrated in Section 9.5.

9.3.6 A Note about Data Presentation

Analyzing braking data and presenting it in a coherent understandable manner is not an easy task. Some of the flight tests were performed on an aircraft with 16 braked tires, a landing lasts approximately 30 seconds and data is recorded at up to 128 Hertz. This results in approximately $60,000$ data points.

In addition, as explained in Section 9.2, if we cut the data into velocity intervals and treat each tire separately this increases the number of cases e.g. five velocity intervals and sixteen tires will produce eighty different correlations for one landing.

As such, we will present only a subset of the data below to identify the robustness of the algorithm and the confidence in the identification process.
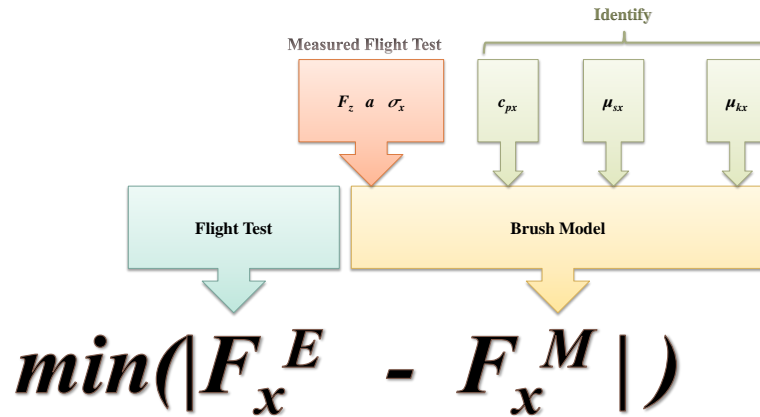
Figure 9.5: The identification algorithm will minimize the error between the brush model frictional force, F_x^M, and flight test data frictional force, F_x^E, by varying c_{px}, μ_{sx} and μ_{kx}

9.4 Three Parameter Optimization

We start with the worst case scenario i.e. the most difficult identification case. This is the case where none of the three unknown parameters, c_{px}, μ_{sx} and μ_{kx}, can be estimated. We will use the identification algorithm as derived in Chapter 8, to identify all three of these unknown parameters.

The process is straight-forward: we will use the identification algorithm developed in Chapter 8 which will vary the three unknown parameters in order to minimize the error between the flight test data and the Brush Model. The process is shown schematically in Figure 9.5

To consolidate the results, we will present two flight tests: one flight test that was performed on a dry runway while the other was performed on a wet runway (a runway is considered wet if there is less than $3mm$ of water, although for this flight test, no water depth measurement was actually taken).

9.4.1 Dry Runway

All Tires - No Velocity Intervals

The first result will make the identification on the ensemble of data points for all tires together, as well as for the entire landing i.e. the data points will not be separated into velocity intervals. As such, the identification algorithm

will fit one $\mu - slip$ curve through the entire range of $60,000+$ points.

Results The identification algorithm identified the three parameters as shown in Table 9.1. We plot the $\mu - slip$ curve in Figure 9.6. The first observation for Figure 9.6 is the dispersion of the data. With 16 tires all braking, there is a significant dispersion in the data. The $\mu - slip$ curve found by the Brush Model is shown as the dotted black line. We clearly see that it passes well through the middle of the points. However, the lack of points on the unstable side of the curve is evident. As such, the determined form of the curve on the unstable (right) side is clearly an estimation. Although the result is a mathematical solution to the problem, the values as shown in Table 9.1 leave some doubt on the validity of the result. In particular, the identified value of μ_{kx} is lower than expected. Through the experimental friction tests performed by the University of Hannover and described in Chapter 6 (page 136), we expect a value of μ_{kx} in the range 0.4 to 0.6. Nevertheless, the difficulty to correctly identify the unknown parameters does not come as a surprise due to the data clustering and lack of points on the unstable side of the curve.

Figure 9.7 presents the overall results comparing the braking force from flight test data to the braking force calculated using the Brush Model equation and the identified parameters. It is surprising to see the accuracy between the Brush Model and the flight test. In general, we have less than 2.5% relative error in the Brush Model despite the fact that we know at least one of the parameters, μ_{kx}, is far from a realistic value. On one hand, this shows the robustness of the Brush Model to determine the braking force despite variations in the input parameters. On the other hand, this demonstrates that the percent error is not a reliable indicator of a correct identification. It is for this reason, we will concentrate on the shape of the $\mu - slip$ curve and value of identified parameters to indicate a correct fitting.

Table 9.1: Identified parameters for a dry runway using all tires without velocity intervals

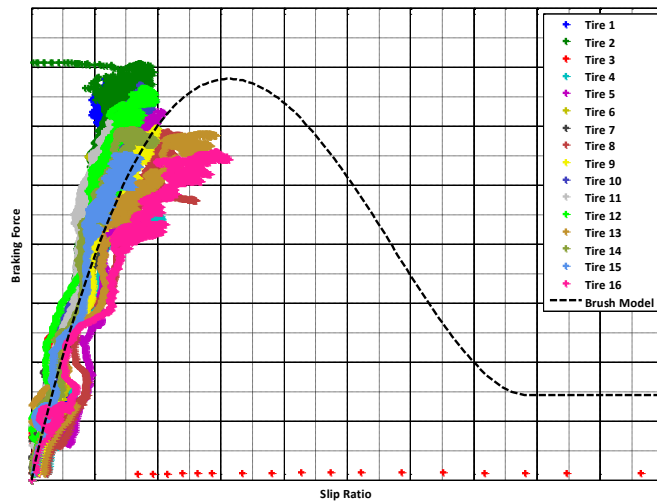| c_{px} (N/m^2)	μ_{sx}	μ_{kx}
4.02E+07	0.957	0.096

Figure 9.6: The $\mu - slip$ curve for a three parameter identification on a dry runway for all tires, without velocity intervals.
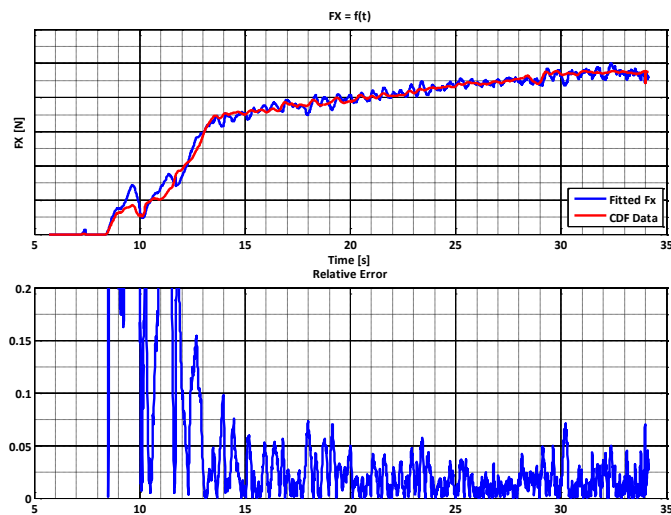

Figure 9.7: The braking force as a function of time, and the relative error between the Brush Model and Flight Test data for a three parameter identification on a dry runway for all tires, without velocity intervals.

All Tires - Five Velocity Intervals

The second fitting will use all of the tires data points together, but will divide the data into velocity intervals. A choice of five velocity intervals was made which is an optimization to have as many intervals as possible while still having sufficient number of points within the velocity interval to make an accurate estimation. The five velocity intervals in *knots* are

1. $120 < GS$
2. $100 < GS < 120$
3. $80 < GS < 100$
4. $60 < GS < 80$
5. $GS < 60$

With this fitting, we hope to be able to identify the effect that speed has on the shape of the $\mu - slip$ curve.

Results The identified parameters are shown below in Table 9.2. In this case, we do not plot the braking force as a function of time because it is nearly identical to that of the case with no velocity intervals (Figure 9.7). That is to say, that regardless of the accuracy of the identified parameters, the robustness of the Brush Model algorithm ensures a close fit (in this case less than 5% error).

In Figure 9.8 we plot the shape of the $\mu - slip$ curve for the five different velocity intervals. However, the clustered data points once again pose a problem to the identification. Although the identified $\mu - slip$ curves are well fit on the stable (left) side of the curves, the unstable (right) side of the curve is simply a best guess by the algorithm.

For speed interval number 1, the identified $\mu - slip$ curve is far from expected with a μ_{sx} higher than expected and a μ_{kx} lower than expected. In addition, the shape of the curve is significantly different than for the other velocity intervals.

Speed intervals 2 through 5 present a more consistent shape. In general, we see that the μ_{max} is increasing as the velocity decreases. This corresponds with our expectations as explained in the Tribology Chapter (6). However, simply from the observations of $\mu - slip$ curves in literature, we expect a larger difference between the μ_{sx} and μ_{kx} which creates the hump (or hill) shape of the $\mu - slip$ curve. In the identified parameters, we have $\mu_{sx} \approx \mu_{kx}$ and thus the hump of the $\mu - slip$ curve is not pronounced.

Table 9.2: Identified parameters for a dry runway test using all tires and five velocity intervals.

Ground Speed (m/s)	c_{px} (N/m^2)	μ_{sx}	μ_{kx}
$120 < GS$	3.58E+07	1.454	0.145
$100 < GS < 120$	5.15E+07	0.361	0.343
$80 < GS < 100$	5.06E+07	0.374	0.356
$60 < GS < 80$	4.75E+07	0.413	0.392
$GS < 60$	4.73E+07	0.436	0.415
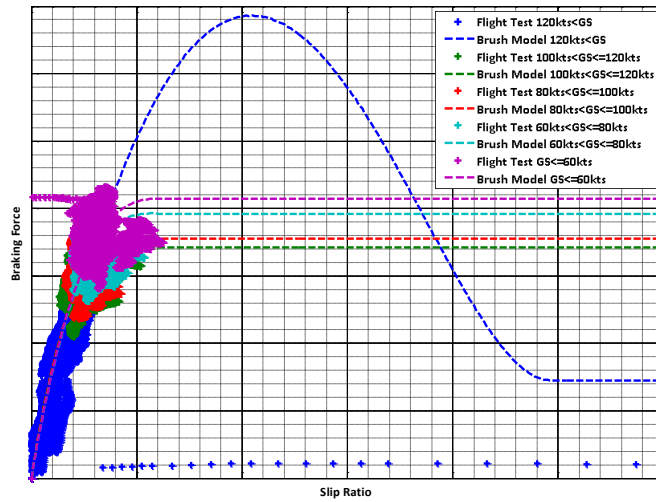
Figure 9.8: The $\mu - slip$ curve for a three parameter identification on a dry runway for all tires, with five velocity intervals.

9.4.2   Wet Runway

We will now repeat the procedure with a flight test performed on a wet runway. As explained in Section 9.3.3, the wet runway will provide more points on the unstable side of the curve as the anti-skid works to prevent the wheel from falling into a skid on the wet runway. However, the velocity effect will be much more pronounced for wet runways. Thus we will skip the identification *All Wheels - No Velocity Interval* as the dispersion of the ensemble of data points is enormous and thus a simple fit through the middle of this large dispersion of points does not give any meaningful results.

All Tires - Five Velocity Intervals

Due to the large dispersion of data points, we have divided the data for each velocity interval creating five subgraphs in Figure 9.10. The three identified parameters are shown in Table 9.3. The first observation is the large range of points found for each velocity interval. As opposed to the dry runway where for certain velocity intervals the points were clustered, the wet runways has a wide range of data points for the entire range of data. In addition, we note the significant number of points on the unstable (right) side of the curve. Visually, in Figure 9.10, we can see that the shape of the $\mu - slip$ curves corresponds well with the data points on both the left and right side of the curves.

We plot the data of Table 9.3 in Figure 9.9. From here we can determine trends in the identified parameters as a function of velocity. We note that in general, the coefficients of friction, μ_{sx} and μ_{kx} increase as the velocity decreases. This is consistent with the experimental data and the tribology theory shown in Chapter 6. For the low speed case, Interval 5, the μ_{kx} is contrary to the trend and the resulting value is lower than expected. However, a closer look at the data displayed in Figure 9.10e, we see that the identified $\mu - slip$ curve does not correspond well to the data on the unstable (right) side of the curve. We see that the majority of the points form a straight line higher than that of the identified curve. In our estimation, a better fit to the data points would have been achieved with a μ_{kx} of approximately 0.3 which would also correspond with the trend shown in Figure 9.9

However, we still note that there is a significant data dispersion due to all of the tire data being used at once. Thus we will perform another identification with each tire separately.

Table 9.3: Identified parameters for a wet runway test using all tires and five velocity intervals.

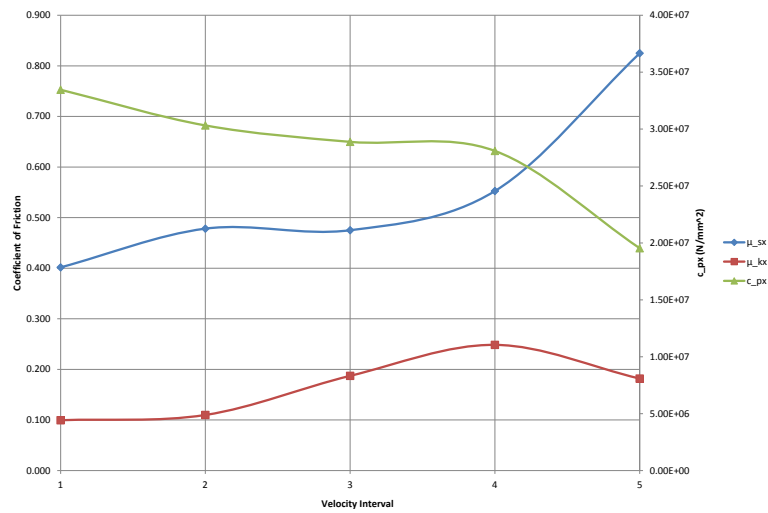| Ground Speed (m/s)	c_{px} (N/m^2)	μ_{sx}	μ_{kx}
$120 < GS$	3.35E+07	0.402	0.099
$100 < GS < 120$	3.03E+07	0.478	0.110
$80 < GS < 100$	2.89E+07	0.475	0.187
$60 < GS < 80$	2.81E+07	0.553	0.248
$GS < 60$	1.95E+07	0.825	0.182

Figure 9.9: We plot the identified parameters c_{px}, μ_{sx} and μ_{kx} as identified for each velocity interval 1 through 5.
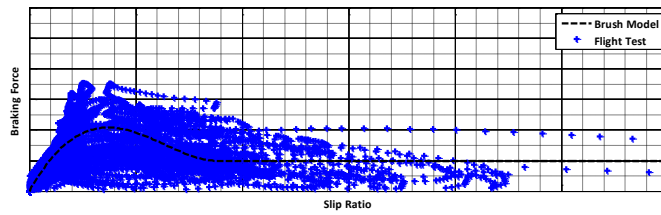
(a) Velocity Interval 1 – 120 < GS
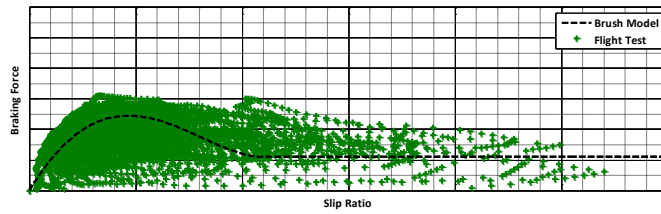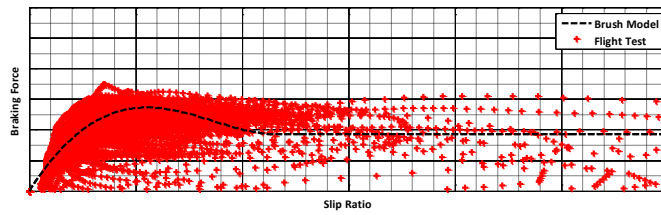
(b) Velocity Interval 2 – 100 < GS < 120

(c) Velocity Interval 3 – 80 < GS < 100
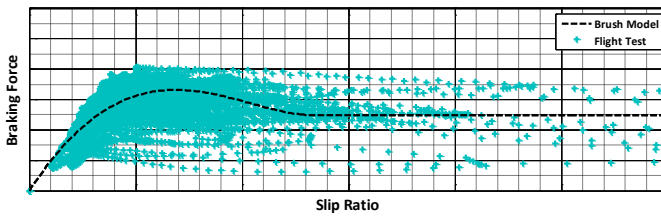
(d) Velocity Interval 4 – 60 < GS < 80
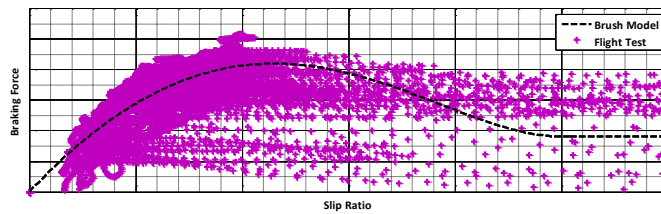
(e) Velocity Interval 5 – GS < 60

Figure 9.10: We plot the $\mu - slip$ curve for different velocity intervals using all tires for a wet runway. Note: All curves are using the same scale for comparison.

Each Tire - Five Velocity Intervals

For this identification, we consider the data points from only one particular tire at a time. Consequently, we perform 80 identifications (16 tires multiplied by 5 velocity intervals). Due to the large amount of data, we display below in Figure 9.12 the data for one tire in the five velocity intervals. The particular tire was to represent an average outcome; some tires had data points which were easier to identify, whereas some tires had data points with a much larger discrepancy resulting in a poorer fit.

Figure 9.12 shows both the advantages and disadvantages of performing the fit on one tire. The dispersion of the data is significantly less when using data points from only one tire. For example for velocity intervals 3 and 5, we note that the identified $\mu - slip$ curve follows well the shape of the data points. On the other hand, we see the effect of having reduced the number of data points by a factor of 16. For example on velocity interval 4, there are no points on the unstable (right) side of the curve with which to influence the identification process. This is contrary to velocity interval 4 for all tires in Figure 9.10 where there are an abundance of points on the unstable side.

We present the identified parameters in the form of three sub-figures within Figure 9.11, one for each parameters c_{px}, μ_{sx} and μ_{kx}. The data is in the form of a bar graph, one bar for each tire and as a function of the velocity interval as shown before in Figure 9.9. Additionally, we plot the mean of the 16 tires and plot this data over-top of the bars.

We note that the mean curves follow the same form as for the 'all-tire' identification i.e. the coefficients of friction are increasing as the velocity decreases and the c_{px} is decreasing as the velocity decreases. In addition to having the same tendency, the mean lines also have roughly the same values. It is encouraging to see that the identification algorithm arrives at roughly the same conclusion whether the identification is made on all tires or each tire individually.

However, we note the large range of values present in the identified parameters. In the same velocity interval but for different tires we have a μ_{kx} of 0.3 and 0.08. In the same way, we see that the c_{px} value varies by a factor of 4 in one velocity interval from 1×10^7 to 4×10^7. This undermines the confidence in the identification as two tires traveling on the same runway, experiencing the same runway state, but the identification process finds two drastically different values.
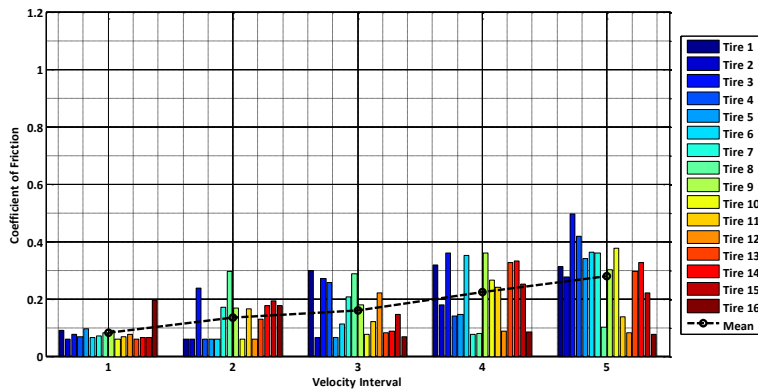
9.4.3 Conclusion

The three parameter identification was performed as it provides the worst case scenario. That is to say, when there is no information available concerning the three unknown parameters. The result of this analysis provided two important conclusions:
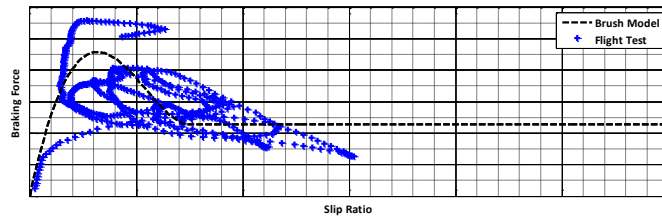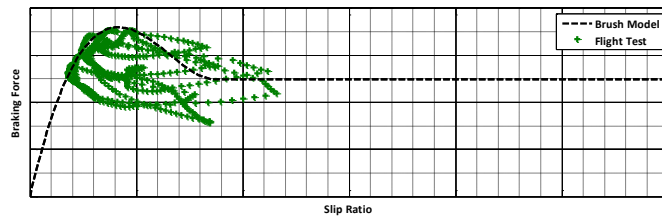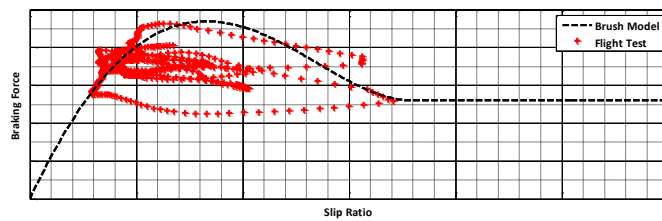
(a) c_{px}

(b) μ_{sx}
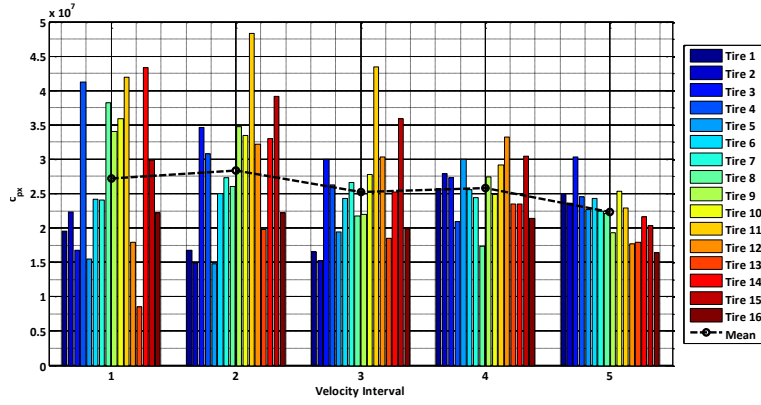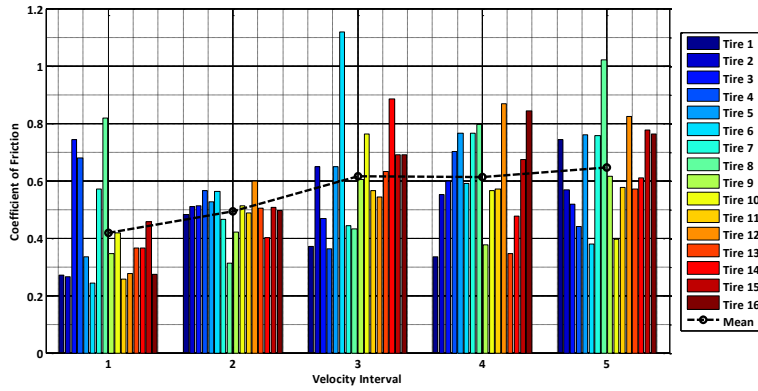
(c) μ_{kx}

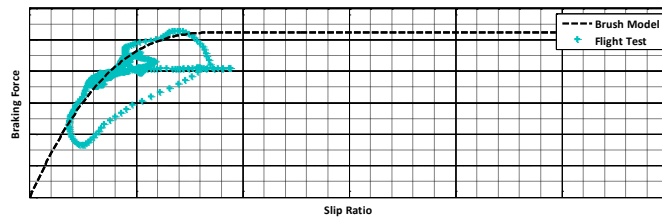Figure 9.11: We plot the identified parameters as a function of the tire number and for different velocity intervals
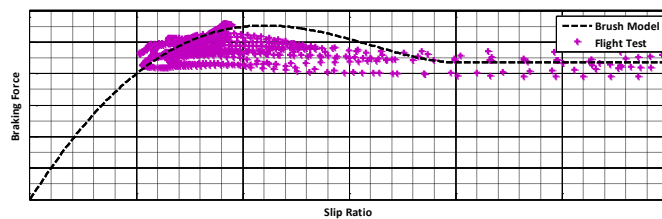
(a) Velocity Interval $1 - 120 < GS$

(b) Velocity Interval $2 - 100 < GS < 120$

(c) Velocity Interval $3 - 80 < GS < 100$

(d) Velocity Interval $4 - 60 < GS < 80$

(e) Velocity Interval $5 - GS < 60$

Figure 9.12: We plot the $\mu - slip$ curve for different velocity intervals on one tire for a wet runway. Note: All curves are using the same scale for comparison.

1. The form of the μ-slip curve is robust. Despite little variation in the data, and identified parameters that were non-physical, the resulting braking force calculated by the Brush Model was within 5% of the measured braking force. This result allows for a certain tolerance in future modeling attempts. That is to say, when using estimated values in place of the unknown variables, the estimated values will provide a correct result as long as they remain within a certain tolerance.

2. The quality of the identification process is directly related to the distribution of the data points in slip. When the data points are clustered around a small range of slip, σ_x, values, a correct identification becomes impossible. However, the greater the distribution of slip values, the more confidence in the identification algorithm. This could lead to future modifications in the algorithm that calculate a confidence value based on the distribution of slip values.

Although the confidence in the determined values is low, two general trends can be derived from the three parameter fitting:
   – that the coefficients of friction are inversely proportional to the velocity
   – that the tire stiffness, c_{px} is proportional to the velocity.

The next section will use estimated values to replace one of the unknown variables, μ_{kx}, resulting in a two parameter identification process.

9.5   Two Parameter Identification

As we have seen in the previous section, using the curve-fitting algorithm with three unknowns leads to uncertain results concerning the identified values. In particular, the dynamic coefficient of friction, μ_{kx}, identified in the three parameter fitting was susceptible to large variations which are not physical. Due to the variability in the dynamic friction coefficient, there was a general lack of confidence in the identified static coefficient of friction, μ_{sx}, as the value is related to the dynamic friction. The identified tire stiffness, c_{px}, from the three parameter fitting was more robust. The identified values from different velocity intervals and different tires were in the same range indicating that the identification algorithm was consistently finding a similar value giving us more confidence in the results.

In order to improve the identification process, we will estimate one of the unknown values using previous experimental results thus leaving two variables to be identified. The choice was made to estimate the μ_{kx} value, thus using the identification algorithm to find c_{px} and μ_{sx} (Schematic in Figure 9.13). The dynamic coefficient of friction proved to be the most erratic variable from the three parameter fitting. From our knowledge of tire-contact physics and the Brush Model, we know that the dynamic friction has a greater impact when a larger portion of the tire-contact zone is sliding i.e. when the slip ratio is greater. As we saw in the previous identification and discussed in Section 9.3.1, on dry runways the anti-skid system regulates the braking so that the slip ratio remains on the stable side of the curve. The lack of data points on the unstable side of the curve prevent an accurate identification. By estimating the μ_{kx} value and inserting it into the Brush Model, we remove the uncertainty due to the unstable side of the mu-slip curve. In addition, the μ_{sx} identification will be improved as it is linked to the μ_{kx}.

To estimate the dynamic coefficient of friction, we use the experimental results obtained from the University of Hannover, Germany. A subset of the results have been presented in Section 9.3.1(pg 136). To estimate the μ_{kx}, for each test and wheel, we first identify the tire pressure and the ambient temperature. To simplify the algorithm, we currently choose an average sliding speed value as seen on the flight test. This results in using one μ_{kx} value for all of the flight test (since the tire pressure, ambient temperature and sliding speed are simplified as constants). Future work of the modeling may integrate an estimation of μ_{kx} at each time step taking into account the sliding speed at that time step along with the thermal effects due to tire-heating.

There is currently no experimental results to estimate the μ_{kx} on wet runways. As such, the following analysis will be performed only for the dry runway case.
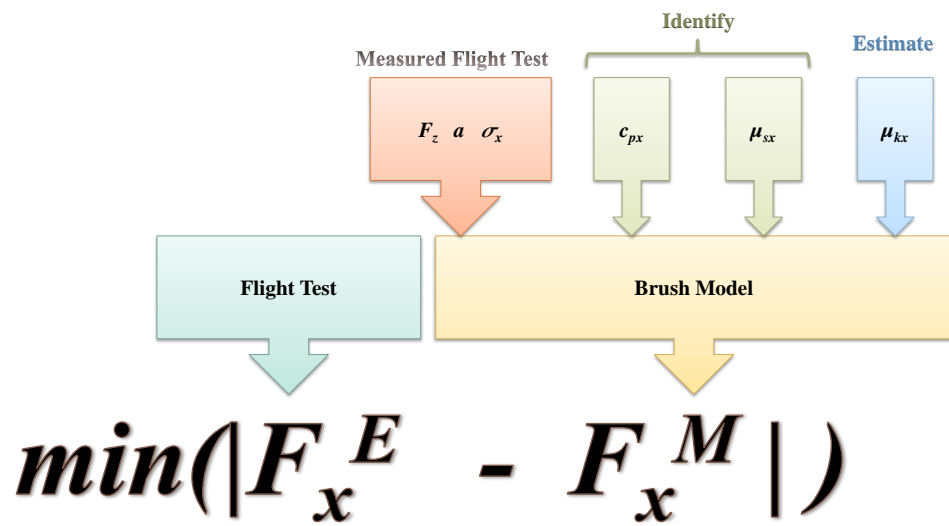
Figure 9.13: Schematic of the Curve Fitting algorithm for two parameters by estimating the μ_{kx} value from experimental results

Remark 5. *The chosen flight test for the two parameter fitting on dry runways is different than the flight test used for the three parameter fitting. The flight test data for the three parameter fitting had a mature anti-skid regulation that functioned very well to keep the slip ratio on the stable side of the curve resulting in clustered data points.*

For the two parameter fitting, a new flight test was found which involved the development of the anti-skid system. For this test, the anti-skid system was not as well regulated resulting in a greater dispersion of data points including a greater portion of data points on the unstable side of the curve. Using this test with the data points on the unstable side of the curve permits to demonstrate that accuracy of the two-parameter fitting. In particular, we can observer the correlation of the points on the unstable side of the curve with the estimated μ_{kx} value.

Remark 6. *The three parameter fitting used five velocity intervals where the first velocity interval was for speeds above 120 knots. The flight test data used for this fitting does not have speeds above 120 knots, thus the data has been divided into four velocity intervals. For clarity, the same color scheme has been used as the three parameter fitting.*

9.5.1 Four Velocity Intervals - All Tires

The first case to be identified will use velocity intervals and all tires. That is to say, we will use the curve fitting to identify the two parameters using the ensemble of points from all 16 braked tires for one velocity interval. The end result is that we identify 4 μ_{sx} and 4 c_{px} values. The results are tabulated below in Table 9.4.

We notice two general trends from the identification process. The first is that, as seen in the three parameter fitting for both dry and wet runways, the tire stiffness, c_{px}, decreases with time of the braking (perhaps an effect of velocity or tire-heating or both). However the tire-stiffness data has shown that it does not change significantly during a test e.g. a reduction of 20% is seen in the data. The second trend is that the μ_{sx} value is seen to be increasing with time of the braking. Once again, the total variation of μ_{sx} over the full test is quite small at around 8%.

Plotting the output of the Brush Model, the braking force F_x^M, against the braking force measured from the flight test, F_x^E, we see once again that there is a very good correlation. The two parameter fitting shows a better correlation than the three parameter dry-runway fitting with an average error (disregarding the start of the test) of less than 2%.

Figure 9.15 presents the μ-slip points for the four velocity intervals.

Table 9.4: Two Parameter fitting with four velocity intervals on all tires.

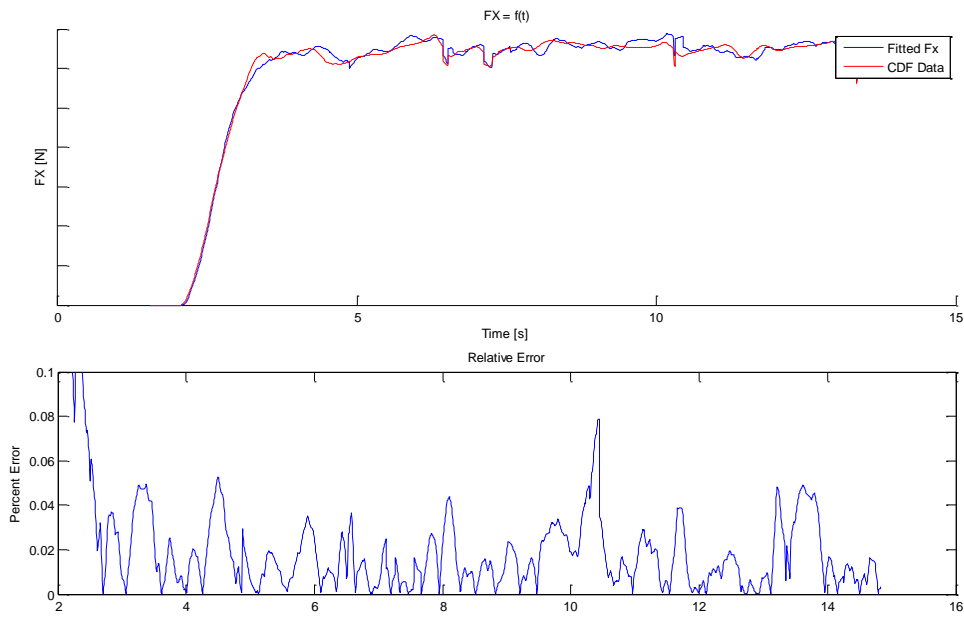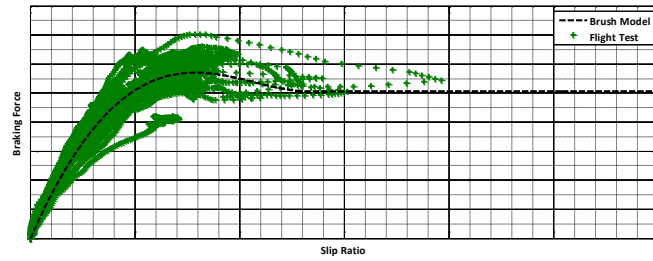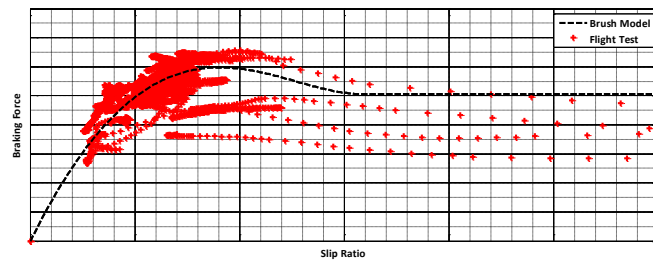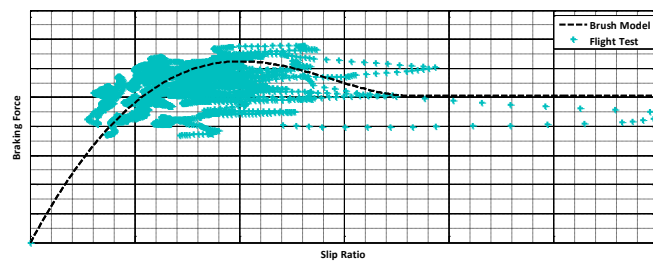| Ground Speed (knots)	c_{px} (N/m^2)	μ_{sx}	μ_{kx}
$100 < GS < 120$	$4.35E + 07$	0.837	0.506
$80 < GS < 100$	$3.79E + 07$	0.916	0.506
$60 < GS < 80$	$3.49E + 07$	0.990	0.506
$GS < 60$	$3.42E + 07$	0.908	0.506

Figure 9.14: A comparison of the F_x^M from the Brush Model and the F_x^E calculated from the flight test data for a two parameter fitting on a dry runway

(a) Velocity Interval $2 - 100 < GS < 120$

(b) Velocity Interval $3 - 80 < GS < 100$

(c) Velocity Interval $4 - 60 < GS < 80$

(d) Velocity Interval $5 - GS < 60$

Figure 9.15: For the two parameter fitting, we plot the $\mu - slip$ curve for different velocity intervals using **all tires** for a dry runway. Note: All curves are using the same scale for comparison.

9.5.2 Four Velocity Intervals - Each Tire

We repeat the identification process done in the previous section, but in this case we perform the identification on each individual tire within each velocity interval. In other words, for each tire we will identify the tire-stiffness and static friction coefficient based on the data points of that specific tire i.e for 16 tires we will identify 16 tire-stiffness coefficients. We recall that this process allows us to determine the characteristics of each tire which could have varying characteristics due to different tire pressures or tire wear. The disadvantage of this process is that there are significantly less data points within each velocity interval to make the identification. As such, there is generally less confidence in the curve-fitting.

To simplify the results, we show the μ-slip curve for one chosen tire, and then show the identified parameters of the ensemble of velocity intervals and tires. Table 9.5 shows the results of the identification giving the mean value of the 16 tires. The results are slightly different than the *All-Tires* fitting. Contrary to the *All-Tires* fitting, we see that the tire-stiffness, c_{px}, has little to no change as a function of the braking time, while the static friction, μ_{sx}, decreases slightly with the braking time, which is the inverse of the *All-Tires* fitting. Although the difference is small, this does cast doubt on the precision of the identification. The μ-slip curve for a single tire is shown in Figure 9.16 and a bar graph of the values found for all 16 tires for the tire stiffness, c_{px} and the static coefficient of friction, μ_{sx} are shown in Figure 9.17

Table 9.5: Two Parameter fitting with four velocity intervals on each tire. The values below represent the mean value found among the 16 tires (Also plotted as the black dotted line in Figure 9.17).

Ground Speed (knots)	Mean c_{px} (N/m^2)	Mean μ_{sx}	μ_{kx}
$100 < GS < 120$	$3.88E+07$	0.968	0.506
$80 < GS < 100$	$3.97E+07$	0.941	0.506
$60 < GS < 80$	$3.87E+07$	0.848	0.506
$GS < 60$	$3.57E+07$	0.892	0.506

9.5.3 Conclusion

Mathematically, the results of the two parameter fitting were obvious. When one of the unknowns is removed from the equation by introducing an experimentally validated value, the confidence of the identification process and the end results improved considerably. The μ-slip curves found from the curve fitting correspond well to the flight test data points. The identified
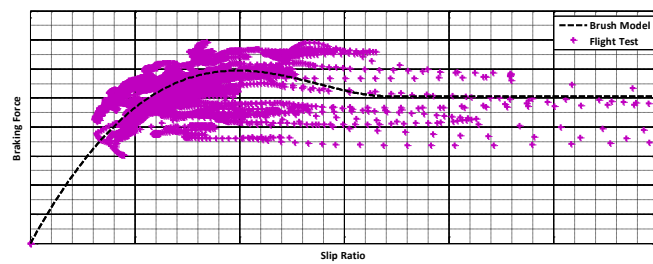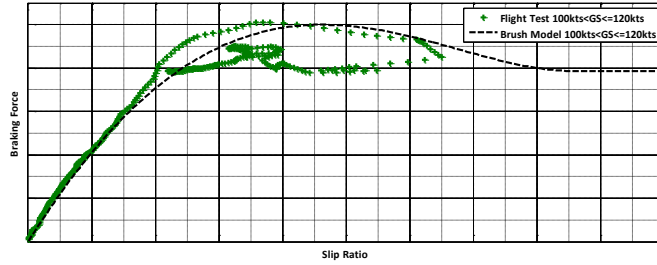
(a) Velocity Interval 2 – $100 < GS < 120$
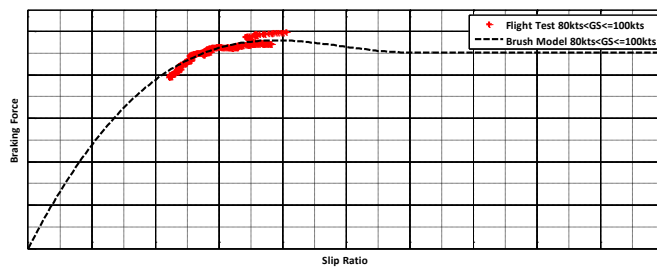
(b) Velocity Interval 3 – $80 < GS < 100$
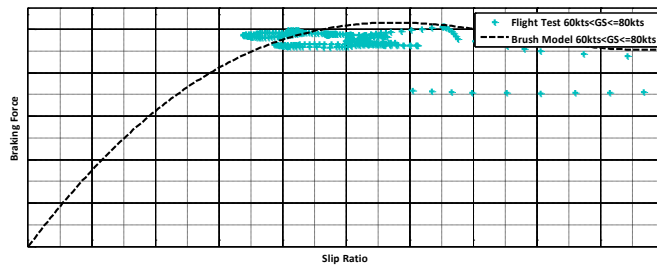
(c) Velocity Interval 4 – $60 < GS < 80$
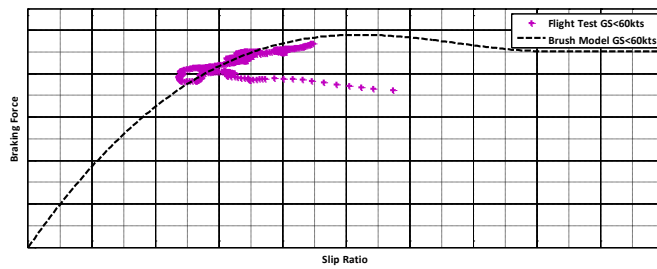
(d) Velocity Interval 5 – $GS < 60$

Figure 9.16: For the two parameter fitting, we plot the $\mu - slip$ curve for different velocity intervals using **a single tire** for a dry runway. Note: All curves are using the same scale for comparison.
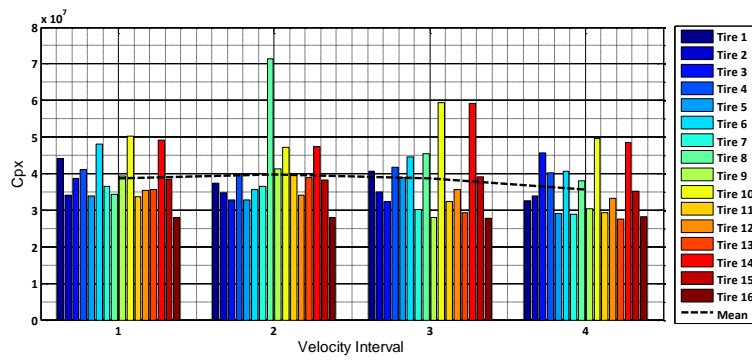
(a) c_{px}
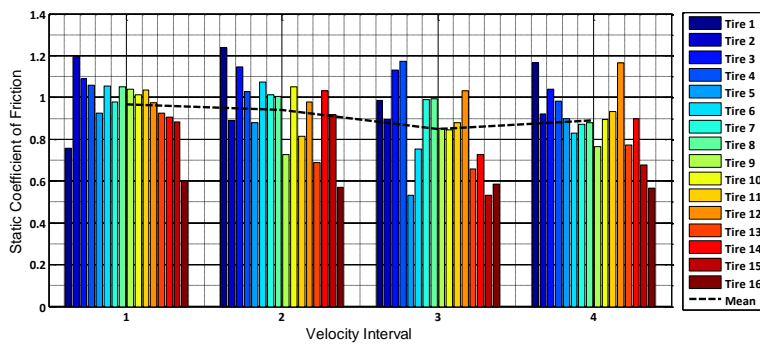
(b) μ_{sx}

Figure 9.17: For the two parameter fitting on **each tire**, we plot the identified parameters, c_{px} and μ_{sx}, as a function of the tire number and for different velocity intervals

values for the tire-stiffness and static coefficient of friction have less variability than in the three parameter fitting which leads to higher confidence in their values.

Both the All-Tire fitting and the Each-Tire fitting found that the tire-stiffness, c_{px}, seems to diminish with tire-braking time. From our knowledge of material science (Chapter 3), this is due to the effect of a high temperature in the rubber decreasing the material strength and the reduced velocity soliciting the rubber at a lower frequency, which also results in lower material strength. However, without additional information on the tire-rubber temperature and the macroscopic texture which solicits the rubber, it is difficult to determine the influence of these two effects.

The *All-Tire* and *Each-Tire* fitting showed inverse effects with regards to the static coefficient of friction. However, in both cases, the variability was small within the values. It demonstrates the downside of the *Each Tire* fitting in that for a certain velocity interval, there may not be enough points to make a confident fit which may lead to erroneous identified values. A future solution to this problem may be to define a confidence parameter based on the number of data points and the data point spread. As we have demonstrated, a larger spread of slip values in the data points leads to higher confidence in the curve fitting. Using a confidence value, we can reject identifications in which we do not have confidence so that they do not perturb the results.

9.6   Conclusion

This chapter has been devoted to using the identification algorithm developed in Chapter 8 to identify unknowns tire-runway contact parameters from flight test data. There are several difficulties in making the fitting, most notably due to the flight test data points.

We first demonstrated the worst case scenario, when there were three unknown in the problem. Due to the form and sensitivity of the Brush Model, a three parameter identification presents several problems due to the infinite number of solutions. Constraints were used which represent the physical nature of the problem, but the three parameter fitting still proved to be difficult to the quality of the flight test data points. In general, we demonstrated than a wet runway is easier to identify that the dry runway case due to the larger interval of data points with which to make the fit. However, for both the dry and wet runways, the identified parameters were often inconsistent from one tire or velocity interval to another. This leads to lack of confidence in the identified values as they do not agree with the basic physics of the problem which says the values should be similar.

The two parameter fitting provided much more consistent results. By removing one of the unknown parameters, the dynamic coefficient of friction,

the three parameter fitting became a two parameter problem. By imposing experimentally validated results in the problem, our confidence in the fitting significantly increases. The identified values were consistent from one interval to another, and the trend of the identified values were consistent with tire-runway physics.

As work continues on this project, the goal will be to expand the validation to more flight tests. Integration of the thermal effects into the problem will aid in explaining the trends seen in the identified parameters. In addition, an important next step will be to determine the coefficient of friction for each time step based on the actual sliding velocity.

We have demonstrated that it is feasible to use the Brush Model with flight test data and that when the parameters have been identified, the Brush Model gives a braking force value, F_x^M within 2% of that measured in flight tests, F_x^E. The Brush Model has proven to well represent the tire-runway contact physics present during braking.

Part IV

Conclusion

Chapter 10

Conclusion

Summary. Cette thèse s'est attachée à la modélisation des forces de frottement qui se produisent entre un pneu d'avion et une piste lors du freinage. Quand un avion atterrit, trois forces se combinent pour le ralentir : l'inversion de poussée (le cas échéant), la traînée aérodynamique et le frottement entre le pneu et la piste dû au freinage. Parmi ces forces, nous avons montré que la force de freinage est la principale force qui contribue pour jusqu'à 80% à la force d'arrêt totale. Afin d'assurer la sécurité des avions lors de leurs opérations quotidiennes, un calcul est fait avant chaque atterrissage pour estimer la distance d'atterrissage aux conditions d'arrivée prévues. Ce résultat est comparé à la longueur de piste disponible pour garantir que l'avion est capable d'atterrir sur l'aéroport avec une marge de sécurité. Pour calculer la distance d'atterrissage, nous avons modélisé les forces impliquées dans l'arrêt de l'avion, principalement la force de freinage. Ainsi, la compréhension des forces de frottement produites lors du freinage est fondamentale pour un fonctionnement en toute sécurité.

La méthodologie actuellement utilisée pour calculer les forces de frottement est une méthode empirique qui s'appuie sur les données des essais en vol. Des essais en vol comportant un freinage sont menés dans ce but et les forces agissant sur l'avion sont séparées pour pouvoir déterminer la force restante due aux freins. En divisant la force de freinage par la charge verticale sur les roues freinées, nous obtenons un coefficient de frottement équivalent (ou global) : μ_{global}. L'objectif de ce travail était d'approfondir notre connaissance des facteurs modifiant le frottement de contact et de construire un modèle représentatif de la physique du contact dans la zone entre le pneu et la piste.

Une bonne partie de ce travail a consisté à développer le modèle de la brosse. Ce modèle n'est pas une nouvelle méthodologie et son utilisation a été largement documentée dans le domaine automobile. Ce modèle a l'avantage de bien représenter la physique du contact dans la zone entre le pneu et la piste ; les calculs sont peu coûteux et permettent des temps de simulation

rapides. L'une des contraintes industrielles imposée à ce travail a été le temps de calcul : le modèle devait avoir un temps de calcul réduit pour permettre une future intégration dans le simulateur de vol.

Nous avons révisé le modèle de la brosse " basique " et avons dérivé les équations de base pour modéliser le frottement pneu-piste dans le sens longitudinal. Nous avons dérivé le frottement de contact en fonction de la rigidité du pneu, de la charge verticale sur la roue, du taux de glissement longitudinal et des coefficients de frottement statique et dynamique. Nous nous sommes alors appuyés sur ce modèle de la brosse " basique " pour mener une étude approfondie de la théorie scientifique et des phénomènes physiques qui s'appliquent aux paramètres du modèle de la brosse. En particulier, nous avons étudié les facteurs modifiant la rigidité du pneu et les coefficients de frottement. Cette étude a permis d'approfondir la connaissance des facteurs environnementaux qui influencent le modèle de la brosse et qui ont par conséquent un effet sur le frottement de contact. Il faut surtout noter que nous avons développé la relation entre la résistance mécanique du caoutchouc et la rigidité du pneu ainsi que les coefficients de frottement statique et dynamique. Ces relations sont particulièrement intéressantes pour le domaine de l'aviation, car les pneus d'avion ont des propriétés mécaniques très différentes de celles des pneus automobiles. Cette thèse nous a permis de mieux comprendre et de quantifier les différences entre le frottement de freinage des avions (qui est mal connu) et le frottement de freinage des automobiles (qui est beaucoup plus développé). Plusieurs partenariats de recherche ont été constitués pour étudier la complexité du frottement entre un pneu d'avion et une piste. Le partenaire principal a été *Airbus Operations* qui a proposé ce thème de recherche, apporté son appui et fourni les données d'essais en vol. En particulier nous avons travaillé avec le *LRCCP* à Paris, France, pour obtenir les données sur les propriétés mécaniques des pneus et avec l'*Institute of Dynamics and Vibration Research* de l'université Leibniz de Hanovre, Allemagne, pour obtenir les données sur les coefficients de frottement entre un pneu d'avion et une piste. Nous pouvons également citer : le *LMA* à Marseille pour la modélisation des pneus, le centre français de recherche aérospatiale *ONERA* pour le développement du modèle de la brosse et l'*University Paul-Sabatier* pour l'identification du modèle. De plus, les travaux de *Svendenius* pour le développement du modèle de la brosse et de *Persson* pour la compréhension de la tribologie ont été d'une valeur inestimable. La dernière partie de cette thèse traite de la validation initiale du modèle de frottement à l'aide des données d'essais en vol. Nous avons utilisé ces données pour identifier les coefficients inconnus dans le modèle de frottement et évaluer la validité de l'identification. Nous avons d'abord présenté le cas le plus défavorable où nous n'avions aucune connaissance préalable des paramètres de frottement. Ce cas présente des inconvénients évidents, mais il sert de référentiel en termes de capacité et de robustesse du modèle et du procédé d'identification. Nous avons ensuite étudié un cas plus réaliste où

nous avons estimé le coefficient de frottement dynamique à l'aide de données expérimentales, ce qui a éliminé une des inconnues dans le procédé d'identification. Grâce à un algorithme plus intelligent, nous avons démontré la capacité à identifier correctement les paramètres et prouvé la robustesse relative du modèle de frottement dans la corrélation aux données d'essais en vol. Cette validation préliminaire a prouvé l'efficacité de la modélisation du frottement basée sur le modèle de la brosse. Ce modèle de frottement fournit une base stable sur laquelle nous pourrons appuyer nos travaux futurs.

10.1   Review

This thesis work has concentrated on modeling the frictional forces that occur between an aircraft tire and a runway during braking. When an aircraft lands, three forces work together to slow the aircraft: the reverse thrust (if used), the aerodynamic drag and the friction between the tire and the runway due to braking. Among these three forces, we have shown that the braking force is the principal force contributing up to 80% of the total stopping force. In order to ensure aircraft security during everyday operations, before every aircraft lands a calculation is made which estimates the landing distance at the predicted arrival conditions and compares this to the actual available length of the runway. This ensures that the aircraft is capable of landing at the airport with a safety margin. In order to make the landing distance calculation, we model the forces that are involved in stopping the aircraft, most notably the braking force. As such, an understanding of the frictional forces generated during braking is fundamental to the safety of airline operations.

The current methodology used in calculating the frictional forces is an empirical method that relies on flight test data. To this end, flight tests involving aircraft braking are performed and the forces reacting on the airplane are separated so that the remaining force due to the brakes is determined. By dividing the braking force by the vertical load on the braked wheels, an equivalent (or global) coefficient of friction is obtained, μ_{global}. In order to expand our knowledge of the factors that affect contact friction, the goal of this PhD work is to build a model which can represent the contact physics occurring in the tire-runway contact zone.

A significant portion of this PhD work has been to develop the Brush Model. The Brush Model is not a new methodology and its use has been extensively documented within the automobile world. The advantage of the Brush Model is that it represents well the contact physics involved in the tire-runway contact zone but is low-cost computationally allowing for rapid simulation time. One of the industrial constraints imposed for this PhD work was computation time; the model needed to have a low computational time in order to permit future integration into the flight simulator.

We reviewed, what we called the basic Brush Model, and derived the basic equations to model the tire-runway friction in the longitudinal direction. We derived the contact friction as a function of the tire-stiffness, the vertical load on the wheel, the slip ratio and the static and dynamic coefficients of friction. We then built upon the basic brush model by studying in depth the scientific theory and physics that pertain to the parameters used within the Brush Model. In particular, we studied the factors that affect the tire-stiffness and the coefficients of friction. This study permits a deeper understanding of environmental factors which influence the Brush Model and as a result have an effect on the contact friction. Of particular interest, we develop the relationship between the rubber mechanical strength and the tire-stiffness, as well as the static and dynamic coefficients of friction. These relationships are of particular interest in the aviation world as aircraft tires have significantly different mechanical properties than automobile tires. This PhD work has permitted us to understand and quantify the differences between aircraft braking friction (which is poorly understood) and automobile braking friction (which is significantly more developed).

Several research partnerships were formed to study the intricacies of aircraft tire-runway friction. The principal partner was *Airbus Operations* who proposed the research and provided the background support and flight test data. In particular, we worked with *LRCCP* in Paris, France to obtain data on the tire-mechanical properties and with the *Institute of Dynamics and Vibration Research* at the University of Hannover, Germany to obtain data on the friction coefficients between an aircraft tire and a runway. Other integral partners included: *LMA* in Marseille for tire modeling, the French Aerospace Lab *ONERA* for Brush Model development and the *University Paul-Sabatier* for model identification. In addition, the works of *Svendenius* for the Brush Model development and *Persson* for understanding of tribology proved invaluable.

The final section of the PhD deals with an initial validation of the friction model using flight test data. We used flight test data to identify unknown coefficients within the friction model and evaluate the validity of the identification. We presented, first, the worst case scenario, where we had no prior knowledge of the friction parameters. This case had obvious drawbacks but it served as a baseline as to the capability and robustness of the model and the identification process. We then performed a more realistic case where we estimated the dynamic friction coefficient using experimental data which reduced one of the unknowns in the identification process. By adding intelligence to the algorithm, we demonstrated the capability to correctly identify the parameters and the relative robustness of the friction model to correlate to the flight test data. This preliminary validation proved the effectiveness of the friction modeling based on the Brush Model theory. The friction model provides a stable base with which to build upon for future works.

10.2   Future Work

The PhD work has provided a baseline model with which to model the contact friction between the tire and the runway. This baseline model has gone through an initial validation process to prove its robustness using flight test data. The future work of this project will aim at continuing the validation of the friction model and the addition of more complex effects that are currently not take into account. In particular:

– This PhD work studies the important effect that temperature has on the tire-stiffness and the tribology. The current friction model does not integrate the contribution that thermal heating during the aircraft braking process has on the tire-model.

– Although this PhD work developed a simple model to predict the tire-stiffness as a function of the vertical load and the tire-pressure, this model was not implemented into the version the friction model used for validation. Using a model of the tire-stiffness will greatly improve the identification process. However the important dynamic effects on tire-stiffness must be studied as the simple model that was developed is valid for static tire-stiffness.

– The understanding of tribology was greatly advanced by studying the works of Persson. The next step will be to integrate the friction models developed by Persson directly into the friction model to replace the experimental data that is currently used.

– The complex relationship between the static and dynamic coefficients of friction must be evaluated. There is currently no method to estimate the static coefficient of friction. As such, in this PhD work, the only means to obtain this value was from identification. In future works, there must be a way to estimate this value.

– To expand the friction model to wet runways, the effect of water lubrication on friction must be studied.

– To expand the friction model to contaminated runways (standing water, snow, ice), more data must be gathered on the friction between the tire and a runway covered by these contaminants.

10.3   Final Word

It is the hope of this author that this PhD work, which lasted three years, will provide a sufficient base for which to continue this work. It seems that friction has often been an afterthought it the aviation world. The aircraft spends the majority of its time in the air and so little of its time on the ground. In the past we have been content to have only a basic understanding of aircraft braking friction. Although this PhD work has demonstrated the complexity involved in contact

friction, it has also demonstrated that despite this complexity, it can be understood, and most importantly, it can be modeled. Furthering our knowledge of the factors that affect friction and obtaining the ability to correctly model the aircraft braking friction will only serve to further enhance the safety and security of aircraft.

Bibliography

[1] F.P. Bowden and D. Tabor. *Friction: an introduction to tribology.* Number 41. Anchor, 1973.

[2] Flight Safety Foundation. FSF ALAR Briefing Note 8.3 – Landing Distances. *Flight Safety Digest*, (November):167–172, 2000.

[3] Flight Safety Foundation. FSF ALAR Briefing Note 8.5 – Wet or Contaminated Runways. *Flight Safety Digest*, (November):179–184, 2000.

[4] Flight Safety Foundation. Reducing the Risk of Runway Excursions. Technical report, Flight Safety Foundation, 2009.

[5] K. A. Grosch. Visco-Elastic Properties and the Friction of Solids: Relation between the Friction and Visco-elastic Properties of Rubber. , 197:858–859, March 1963.

[6] Gert Heinrich and Manfred Kluppel. Rubber friction, tread deformation and tire traction. *Wear*, 265(7-8):1052 – 1060, 2008.

[7] H.P. Jost. Tribology: How a word was coined 40 years ago. *Tribology & lubrication technology*, 62(3):24–28, 2006.

[8] R.S. Lakes. *Viscoelastic materials.* Cambridge University Press Cambridge, UK, 2009.

[9] BMT Fleet Technology Limited. RuFAB - Runway Friction Characteristics Measurement and Aircraft Braking. Technical report, European Aviation Safety Agency (EASA), 2010.

[10] Marc A. Meyers and Krishan Kumar Chawla. *Mechanical behavior of materials.* Prentice Hall, 1999.

[11] B N J Persson. Rubber friction and tire dynamics. *Journal of Physics: Condensed Matter*, 23(1):015003, 2011.

[12] B. N. J. Persson, F. Bucher, and B. Chiaia. Elastic contact between randomly rough surfaces: Comparison of theory with numerical results. *Phys. Rev. B*, 65(18):184106, Apr 2002.

[13] Bo N. J. Persson. On the theory of rubber friction. Technical Report 401, Surface Science, 1997.

[14] Bo N. J. Persson. Qualitative theory of rubber friction and wear. Technical Report V 112, N 4, Journal of Chemical Physics, 2000.

[15] Bo N. J. Persson. Theory of rubber friction and contact mechanics. Technical Report V 115, N 8, Journal of Chemical Physics, 2001.

[16] Bo N. J. Persson. Theory of rubber friction: Nonstationary sliding. Technical Report V 65, 134106, Physical Review B, 2002.

[17] Bo N. J. Persson. On the nature of static friction, kinetic friction and creep. Technical Report 254, Wear, 2003.

[18] Bo N. J. Persson. Rubber friction on wet and dry road surfaces: The sealing effect. Technical Report V 71, 035428, Physical Review B, 2005.

[19] Bo N. J. Persson. Rubber friction: role of the flash temperature. Technical Report Vol 18 Nï¿$\frac{1}{2}$32, Journal of Physics, 2006.

[20] Bo N. J. Persson and Nicholas D. Spencer. Sliding friction: Physical principles and applications. *Physics Today*, 52(1):66–68, 1999.

[21] Rob Rasmussen. European Testing Blog.

[22] M. Rubinstein and R.H. Colby. *Polymer physics*, volume 105.

[23] Jacob Svendenius. Tire models for use in braking applications :. Technical Report ISRN LUTFD2/TFRT–3232–SE, Lund Institute of Technology, 2003. Licenciate Thesis.

[24] Jacob Svendenius. Tire modeling and friction estimation :. Technical Report PhD, Lund University, 2007. PhD Thesis.

Modélisation des forces de contact entre le pneu d'un avion et la piste

Lorsqu'un avion atterrit, la force principale nécessaire pour arrêter l'avion est obtenue par le freinage. Par une réduction de la vitesse de rotation des roues, les freins provoquent une vitesse de glissement entre les pneus et la piste. C'est cette différence de vitesse qui génère la force de freinage capable de stopper l'avion. La modélisation de cette force est essentielle pour l'estimation de la longueur de piste à l'atterrissage.

Les modèles classiques utilisés par les avionneurs sont assez simplistes et dérivent expérimentalement des modèles de frictions les plus simples. De sorte que ces modèles sont dans l'incapacité d'estimer l'influence de paramètres clefs influençant la force de freinage. Il s'agit, en particulier de la pression des pneus, de la nature de la gomme, de la température ambiante et de celle de la gomme, de l'état de la piste, de sa texture, etc.

L'objectif de la thèse a été de développer un modèle de contact pneu-piste capable d'estimer la force de freinage. C'est le « Brush Model » qui a servi de base à cette modélisation. En phase de freinage la zone de contact est constituée d'une première zone de déformation de la gomme qui crée une force résistante en suivant la loi de Hooke, puis d'une seconde zone de glissement dont la force de résistance suit la loi de Coulomb. Ce modèle a été amélioré grâce aux résultats de la mécanique des structures pour la loi de Hooke et grâce aux résultats de la tribologie pour la loi de Coulomb. Ces deux modélisations faisant appel aux données issues de la science des matériaux. L'ensemble de ces modélisations a été enrichi par une coopération avec plusieurs centres de recherches ayant fourni de nombreux résultats expérimentaux.

Le modèle obtenu a ensuite été confronté avec des résultats d'essais en vol obtenus avec « Airbus Operations S.A.S ». La thèse a validé le prétraitement des données d'essais ainsi que le processus d'identification qui a permis de montrer l'accord du modèle avec les résultats expérimentaux obtenus lors des essais en vol.

Cette modélisation donne des résultats très encourageants, elle permet une compréhension beaucoup plus approfondie des effets de l'environnement sur les forces de freinage. De sorte que cette thèse a permis d'améliorer très sensiblement la compréhension fondamentale des phénomènes en jeu lors du freinage, au contact entre le pneu et la piste. Chez Airbus, les résultats obtenus vont servir de base pour les travaux à venir sur ce thème.

Mots-Clés : frottement, pneu, piste, brush model, avion, caoutchouc, taux de glissement, Coulomb

Modeling the contact forces between an aircraft tire and the runway

As an aircraft lands on a runway, the principal force acting to stop the aircraft within the confines of the runway is generated by the brakes. The brakes cause the tire's rotational speed to slow down with regards to the aircraft's speed over the ground. This difference in speed causes friction and it is this friction that is the principal force to stop the aircraft. In order to be able to estimate the stopping distance of an aircraft an understanding of this friction is essential.

Traditionally, aircraft manufactures have relied on simplistic, empirically derived friction models. However, these empirical models cannot estimate the influence of several key factors that are known (scientifically) to affect friction such as the rubber temperature, the runway texture, the ambient air temperature and the rubber composition to name a few.

This PhD work aims to develop a frictional model that can be used to estimate the friction developed between an aircraft tire and the runway. A model commonly known as the Brush Model, is derived for use with aircraft tires and runways. The underlying physics of this model are developed using the established scientific theories of tribology, material science and strength of materials. Coordination with several research institutes provides experimental results to reinforce the model.

The model is then compared with flight test results obtained from a partnership with Airbus Operations S.A.S. The PhD works demonstrates the entire validation process from flight test data cleaning, the derivation of a curve-fitting algorithm and the matching of derived model with the flight test data.

The modeling has shown very encouraging results. It allows for a much deeper understanding of the environmental effects on friction. This PhD work has greatly improved the fundamental understanding of friction and will serve as a base for future works with Airbus.

Keywords: Friction, Runway, Tire, Brush Model, Aircraft, tribology, rubber, anti-skid, slip ratio, Coulomb